ORBIT STRUCTURES IN THE PLANAR CIRCULAR RESTRICTED THREE-BODY PROBLEM AND ITS APPLICATIONS

A THESIS SUBMITTED TO
THE GRADUATE SCHOOL OF NATURAL AND APPLIED SCIENCES
OF
MIDDLE EAST TECHNICAL UNIVERSITY

BY

ŞAHİN ULAŞ KÖPRÜCÜ

IN PARTIAL FULFILLMENT OF THE REQUIREMENTS
FOR
THE DEGREE OF MASTER OF SCIENCE
IN
PHYSICS

JULY 2023

Approval of the thesis:

ORBIT STRUCTURES IN THE PLANAR CIRCULAR RESTRICTED THREE-BODY PROBLEM AND ITS APPLICATIONS

submitted by **ŞAHİN ULAŞ KÖPRÜCÜ** in partial fulfillment of the requirements for the degree of **Master of Science in Physics Department, Middle East Technical University** by,

Prof. Dr. Halil KALIPÇILAR
Dean, Graduate School of **Natural and Applied Sciences** _____

Prof. Dr. Seçkin KÜRKÇÜOĞLU
Head of Department, **Physics** _____

Prof. Dr. Bayram TEKİN
Supervisor, **Physics, METU** _____

Examining Committee Members:

Prof. Dr. Seçkin KÜRKÇÜOĞLU
Physics, METU _____

Prof. Dr. Bayram TEKİN
Physics, METU _____

Prof. Dr. Tahsin Çağrı ŞİŞMAN
Astronautical Engineering, UTAA _____

Date:06.07.2023

I hereby declare that all information in this document has been obtained and presented in accordance with academic rules and ethical conduct. I also declare that, as required by these rules and conduct, I have fully cited and referenced all material and results that are not original to this work.

Name, Surname: ŞAHİN ULAŞ KÖPRÜCÜ

Signature :

ABSTRACT

ORBIT STRUCTURES IN THE PLANAR CIRCULAR RESTRICTED THREE-BODY PROBLEM AND ITS APPLICATIONS

KÖPRÜCÜ, ŞAHİN ULAŞ
M.S., Department of Physics
Supervisor: Prof. Dr. Bayram TEKİN

July 2023, 86 pages

In this thesis, orbit structures in the planar Circular Restricted Three-Body Problem (CRTBP) are studied with a geometrical perspective. Unlike the two-body problem, there is no general analytical solution for the three-body problem due to its chaotic nature. Therefore, qualitative methods provide precious insights for the orbit structures in CRTBP.

In this regard, stability analysis of the equilibrium points is performed and the local orbit structures like periodic, transit and non-transit orbits around those points are investigated. Then, the periodic orbits in the planar CRTBP, so called Lyapunov orbits, are studied in more detail in terms of their stability and global connections. The global orbit structures like homoclinic and heteroclinic orbits are calculated by utilizing the invariant manifolds associated to Lyapunov orbits. In addition, the sensitive dependence to the initial conditions of a Lyapunov orbit is investigated with the use of the Lyapunov exponent which is one of the chaos indicators.

Lastly, the two possible applications of the CRTBP are demonstrated. The first application is about constructing fuel efficient low-energy spacecraft trajectories from

Earth to Moon by using CRTBPs of the Sun-Earth-spacecraft and the Earth-Moon-spacecraft. The second application is about the search for the undiscovered Planet 9 with sub-relativistic spacecrafts in the context of Sun-Planet 9-spacecraft CRTBP to investigate whether considering the Sun yields new prospects for the detection of Planet 9.

Keywords: Circular Restricted Three-Body Problem, Local and Global Orbit Structures, Low-energy Earth to Moon Transfer Trajectory, Search for Planet 9

ÖZ

DÜZLEMSEL DAİRESEL KISITLI ÜÇ-CİSİM PROBLEMİNDEKİ YÖRÜNGE YAPILARI VE UYGULAMALARI

KÖPRÜCÜ, ŞAHİN ULAŞ
Yüksek Lisans, Fizik Bölümü
Tez Yöneticisi: Prof. Dr. Bayram TEKİN

Temmuz 2023 , 86 sayfa

Bu tezde düzlemsel Dairesel Kısıtlı Üç-Cisim Problemindeki (DKÜCP) yörünge yapıları geometrik bir bakış açısıyla incelenmiştir. Üç-cisim probleminin kaotik doğası sebebiyle iki cisim problemindeki gibi genel bir analitik çözüm bulunmamaktadır. Bu sebeple nitel yöntemler DKÜCP'deki yörünge yapılarını anlamak için önem arz etmektedir.

Bu bağlamda, denge noktalarının stabilite analizi gerçekleştirilmiş, ve bu noktalar etrafındaki periyodik, transit ve transit olmayan yörüngeler gibi lokal yörünge yapıları araştırılmıştır. Ardından, Lyapunov yörüngeleri olarak adlandırılan düzlemsel DKÜCP'deki periyodik yörüngeler detaylı bir şekilde incelenmiş, bu periyodik yörüngelerin stabilitesi ve birbirleriyle global ilişkileri çalışılmıştır. Homoklinik ve heteroklinik yörüngeler gibi global yörünge yapıları, Lyapunov yörüngelerinin değişmez manifoldları kullanılarak hesaplanmıştır. Ek olarak bir Lyapunov yörüngesinin başlangıç durumuna hassas bağımlılığı, bir kaos göstergesi olan Lyapunov üssü ile incelenmiştir.

Son olarak DKÜCP'nin iki olası uygulaması gösterilmiştir. Bunlardan ilki, Güneş-Dünya-uzay aracı ve Dünya-Ay-uzay aracı DKÜCP'lerini kullanarak Dünya'dan Ay'a yakıt tasarruflu düşük enerjili uzay aracı yörüngelerinin tasarlanmasıdır. İkincisi ise henüz keşfedilmemiş 9. gezegenin alt-göreceli uzay araçları ile Güneş-9. Gezegen-uzay aracı DKÜCP bağlamında araştırılması ve 9. Gezegenin bu yöntemle tespitinde Güneş'in nasıl bir etkisi olduğunun incelenmesidir.

Anahtar Kelimeler: Dairesel Kısıtlı Üç-Cisim Problemi, Lokal ve Global Yörünge Yapıları, Dünya'dan Ay'a Düşük Enerjili Yörünge Transferi, 9. Gezegeni Araştırma

To My Family

ACKNOWLEDGMENTS

I would like to thank my supervisor Prof. Dr. Bayram Tekin for accepting me as his master's student even I have an undergraduate degree different than physics. His lectures and our thesis meetings have been always pleasent and enlightening for me.

In addition, I would also like to thank Prof. Dr. Tahsin Çağrı Şişman who helped and guided me as co-advisor throughout the thesis period. It has been always a great pleasure to talk and discuss any subject with him. We have been working since I was an undergraduate student. I learnt and have been still learning so much thanks to him.

TABLE OF CONTENTS

LIST OF TABLES

TABLES

LIST OF FIGURES

FIGURES

LIST OF ABBREVIATIONS

CRTBP	Circular Restricted Three-Body Problem
WSB	Weak Stability Boundary
STM	State Transition Matrix
FTLE	Finite Time Lyapunov Exponent
SOI	Sphere of Influence
EM	Earth-Moon Barycenter
BRFBP	Bicircular Restricted Four-Body Problem
LEO	Low Earth Orbit
LLO	Low Lunar Orbit
VLBI	Very Long Baseline Interferometry
TNOs	Trans-Neptunian Objects
ERTBP	Elliptic Restricted Three-Body Problem

CHAPTER 1

INTRODUCTION

1.1 Review of the Three-Body Problem

The three-body problem investigates the motion of three bodies under their mutual gravitational attractions. Due to the chaotic nature of the problem and therefore sensitive dependence to the initial conditions, there is no general analytical solution unlike the two-body problem. This makes the three-body problem attractive to great physicists and mathematicians over centuries. As an introduction of the thesis, a brief summary of the three-body problem is given with the historical aspects. In this review, [1] is greatly benefited.

History of the problem dates back to Newton. He introduced the three-body problem to investigate motion of the Sun, Earth and Moon system but could not obtain a closed form solution unlike the two-body problem [1]. In 1767, Euler [3] found the first periodic solution for a particular initial configuration in which the three masses are initially placed on a line and separated from each other according to their mass ratios. In addition, he also formulated the motion of three-bodies relative to the rotating frame and introduced the context of Circular Restricted Three-Body Problem (CRTBP). In 1772, just after Euler, Lagrange [4] found a new periodic solution for the equilateral triangular configuration where the three masses are initially placed at the vertices of a triangle. In both Euler's and Lagrange's solutions, the net force on each mass is toward to their common center of mass during the motion, and they are the only central configurations in the three-body problem.

[1] Newton told to Halley that the theory of Moon made his headache and 'kept it awake so often, that he would think of it no more' [2].

In the second half of nineteenth century, attempts for finding series solution were performed because of the closed-form solution seemed to be unlikely. Delaunay [5], Lindstedt [6], Gyldén [7] and later Sundman [8] studied on obtaining a series solution but covergence and complexity of the expressions were the issues making the series solution impractical. Around the end of nineteenth century, Poincaré made great contributions to the three-body problem with his monumental three-volume book which was later translated as *New Methods of Celestial Mechanics* [9]. He proposed a qualitative approach with geometrical perspective for the solution of differential equations and his approach led to find periodic orbits in the CRTBP. In addition, he also realized the sensitive dependence to the initial conditions in the three-body problem which led the foundation of the chaos theory. Further information about his contributions to the three-body problem can be found in [10].

In the second half of twentieth century, Kolmogorov [11], Moser [12] and Arnold [13] studied the stability of periodic orbits in the three-body problem against small perturbations, and the results of their studies related to quasiperiodic motion are now called as the KAM theorem. Apart from the analytical studies, numerical investigations to find periodic orbits accelerated with the advents in computer technology. In 1970s, Hénon [14], Szebehely [15] and many other authors [16], [17] found the families of periodic orbits in the three-body problem by using computer simulations. In 1993, figure-eight shape periodic orbit was found numerically by Moore [18] and later its existence was proven by Chenciner and Montgomery [19]. In 2010s, many new periodic orbits were found numerically [20], [21], [22] and [23]. More recently, Stone and Leigh [24] obtained a statistical solution by studying the distribution of outcome trajectories. Besides, Breen et al. [25] used Artificial Neural Networks to obtain fast and scalable simulations compared to numerical integrations. All those attempts show that the centuries old three-body problem has not been completely solved and is open to new discoveries.

1.1.1 Circular Restricted Three-Body Problem

Since the CRTBP is the subject of the thesis, it is reviewed in a bit more detail in this section. In CRTBP, there are two primary bodies moving in circular orbits around

their common center of mass and the motion of the third body with negligible mass is studied. Apart from the general three-body problem, the mass of third body is restricted so that it does not affect the motion of the two primaries. As mentioned previously, the CRTBP was first introduced by Euler. Then, Lagrange found five equilibrium points and now they are referred as Lagrange points. In 1836, Jacobi [26] obtained a constant of motion in the CRTBP and it was used by Hill [27] to specify realms of motion. So, the allowable region for the motion of third body is now also called as Hill's region. Afterwards, Poincaré developed qualitative methods with a geometrical perspective to obtain periodic orbits of the third body. His well-known surface of section, so called Poincaré section, is a surface that transverses to the motion and is used to analyze the stability of the periodic orbits. In speaking of stability, Lyapunov's studies [28] should be also credited. He introduced the concept of Lyapunov stability which is defined as if a trajectory starts near an equilibirum point, it will stay nearby forever. In this regard, the planar periodic orbits around the collinear equilibrium points in the CRTBP are now called as Lyapunov orbits. In addition, he introduced the concept of the Lyapunov exponent which tells how the trajectories obtained from two neighbourhood initial conditions evolve over time. It is now used as a chaos indicator. Besides the collinear equilibrium points, it was found that the triangular equilibrium points are stable for a certain range of mass parameters of the primaries. Therefore, periodic orbits were found also around the triangular equilibrium points, the so called Tadpole and Horseshoe orbits due to their shapes.

In addition to the planar case, numerious periodic orbits were found for the spatial CRTBP. For example, if the ratio of in-plane and out-plane frequencies is irrational, the resulting trajectory is a quasi-periodic orbit which is commonly known as Lissajous orbit as it is related to the Lissajous curve. In contrast, if their ratios are rational, the resulting trajectory is a three dimensional periodic orbit, the so called Halo orbit. The name Halo was first used by Farquhar [29] because the periodic orbit of a spacecraft around a collinear equilibrium point is seen as a halo around the Moon for the observer who looks from the Earth. Other types of periodic orbits in CRTBP can be found in [30].

The CRTBP has many applications in celestial mechanics and space mission design.

For example, the existance of Trojan asteroids are well explained in the context of Sun-Jupiter-Trojans CRTBP. The mass parameter of Sun-Jupiter system suggests the stable mode for the triangular equilibrium points. In addition, the CRTBP can be also considered as a suitable dynamical model for the following celestial systems [1]; a single star with giant and terrestial exoplanets, a single star with a giant exoplanet and exomoon, binary stellar systems with a giant or terrestial exoplanet. Besides, the CRTBP is a useful setting for the design of space missions. In 1970s, Farquhar considered to utilize Halo orbits for the continous communication from Moon to Earth during the Apollo missions. In 1990s, Belbruno and Miller [31] found fuel efficient Earth to Moon transfer trajectories compared to traditional Hohmann transfer, the so called Weak Stability Boundary (WSB) transfers. Later, Koon et. al [32] developed the concept of patched three-body approximation by utilizing the qualitative methods of CRTBP and the lagrange point dynamics. These transfers are now commonly known as low-energy transfers.

1.2 Aims and Motivations

In this thesis, orbit structures in the planar CRTBP are investigated qualitatively with a geometrical point of view. In this regard, aims and motivations of the thesis can be described as follows;

- In many physical problems, particularly the chaotic ones, there is no analytical solution. So, the first goal of the thesis is to learn qualitative methods for the solution of differential equations. In this thesis, the interest is CRTBP but the methods given here are generic and can be applied to different problems.
- The second goal of the thesis is to construct a theoretical background in CRTBP for advanced research.
- The last goal of the thesis is to demonstrate possible applications of CRTBP.

1.3 The Outline of the Thesis

In this thesis, order of chapters and contents are highly aligned with [33].

In Chapter 2, first the CRTBP is introduced and the equations of motion are given. To reduce the number of parameters and obtain a simpler form of equations of motion, nondimensionalization is applied. Then, three collinear and two triangular equilibrium points are found. Finally, Jacobi constant is given and the classes of motion are classified based on the Jacobi constant.

In Chapter 3, stability of the equilibrium points are studied in detail. First, the equations of motion are linearized around the equilibrium points, then the local orbit structures are classified based on the solutions of linearized equations.

In Chapter 4, the planar periodic orbits around collinear equilibrium points, the so called Lyapunov orbits, and their global connections are studied. First, the periodic solution found from the linear approximation is improved by utilizing the differential correction method in nonlinear equations of motion of CRTBP. Then, the family of Lyapunov orbits are generated with numerical continuation. To analyze the stability of the Lyapunov orbits, Poincaré map is utilized. Related with this stability analysis, stable and unstable invariant manifolds associated to Lyapunov orbits are generated. Then, the global connections between Lyapunov orbits, the so called Homoclinic and Heteroclinic connections, are calculated by using these manifold structures. Finally, the chaotic nature and therefore sensitive dependence to the initial conditions in CRTBP is studied with use of Lyapunov exponent.

In Chapter 5, two applications of CRTBP are demonstrated. As a first application, Earth to Moon low-energy trajectory of a spacecraft is studied. In this regard, CRTBP of Sun-Earth-spacecraft and Earth-Moon-spacecraft are considered. Then, the trajectory design methodology is described and the resulting low-energy transfer is compared with traditional Hohmann transfer. As a second application, a search for Planet 9 with sub-relativistic spacecrafts is studied. Here, CRTBP of Sun-Planet 9-spacecraft is considered and it is searched for whether considering the Sun yields new prospects for the detection of Planet 9.

In Chapter 6, results of the thesis are summarized.

CHAPTER 2

THE CIRCULAR RESTRICTED THREE-BODY PROBLEM

2.1 Introduction

The CRTBP investigates the motion of a point particle with a negligible mass in the gravitational field of two massive bodies moving in a circular orbit. There are some assumptions which make differences from the general three-body problem. Those are;

- The mass of third body is too small, in another words "restricted", such that it does not effect the motion of other two massive bodies.
- The two massive bodies are moving in a "circular" orbit around their common center of mass.

Reference frame of the CRTBP is given in Fig. 2.1. Origin, G, is the center of mass of two massive bodies, the x-axis is in the direction from G to m_2 and the z-axis is perpendicular to the plane of circular motion. Since the x-axis rotates with the motion of m_1 and m_2, this is a non-inertial reference frame. The reason for the choice of a rotating frame will be understood better in the upcoming chapters, but for now it can be said that investigating the motion relative to rotating frame yields more insight for understanding the orbit structures by utilizing the equilibrium point dynamics.

2.2 Equations of Motion

The detailed derivation of the equations of motion of CRTBP can be found in Section 2.12 in [34]. The equations of motion of the third body relative to rotating frame

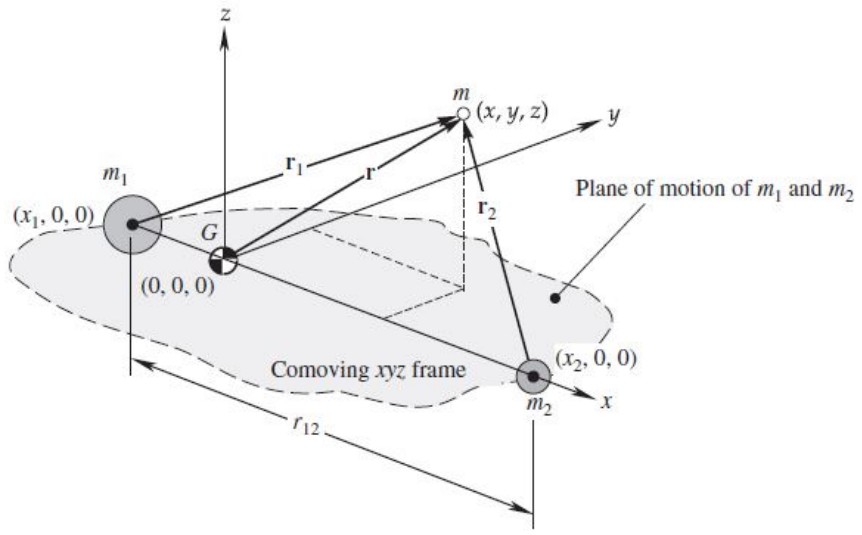

Figure 2.1: Configuration of the CRTBP [34], the mass m is considered to be much smaller than m_1 and m_2.

given in Fig. 2.1 are written as;

$$\ddot{x} - 2\Omega\dot{y} - \Omega^2 x = -\frac{\mu_1}{r_1^3}\left(x + \pi_2 r_{12}\right) - \frac{\mu_2}{r_2^3}\left(x - \pi_1 r_{12}\right), \tag{2.1a}$$

$$\ddot{y} + 2\Omega\dot{x} - \Omega^2 y = -\frac{\mu_1}{r_1^3}y - \frac{\mu_2}{r_2^3}y, \tag{2.1b}$$

$$\ddot{z} = -\frac{\mu_1}{r_1^3}z - \frac{\mu_2}{r_2^3}z, \tag{2.1c}$$

where Ω is the angular velocity of the rotating frame, μ_1 and μ_2 are the gravitational parameters of m_1 and m_2 respectively, r_{12} is the distance between m_1 and m_2, lastly $\pi_1 = \frac{m_1}{m_1+m_2}$ and $\pi_2 = \frac{m_2}{m_1+m_2}$ are the mass ratios.

The terms in the right-hand side are the accelerations due to gravitational field of m_1 and m_2. In the left-hand side, the second and the third terms are Coriolis and centrifugal accelerations, respectively, which arise from the rotation of the reference frame. Since the z-axis is the axis of rotation, there is no contribution coming from the rotation.

The Eqns. (2.1) are second order, nonlinear, ordinary differential equations. There is no general analytical solution of these equations due to sensitive dependence on initial conditions. Although, it is possible to obtain numerical solutions by using numerical integration methods like Runge-Kutta [35].

2.2.1 Nondimensionalization

Nondimensionalization is applied in order to reduce the number of parameters, avoid the large numbers and obtain simpler form of equations of motion. The following substitutions are used to obtain nondimensional quantities;

$$X = \frac{x}{r_{12}}, \quad Y = \frac{y}{r_{12}}, \quad Z = \frac{z}{r_{12}}, \quad R_1 = \frac{r_1}{r_{12}}, \quad R_2 = \frac{r_2}{r_{12}}, \quad \mu = \frac{m_2}{m_1 + m_2}, \quad \tau = \Omega t, \tag{2.2}$$

so that 1 unit distance is equal to r_{12}, 1 unit time is equal to $1/\Omega$ and 1 unit mass is equal to $m_1 + m_2$. Then, the nondimensional form of the equations of motion are written as;

$$\ddot{X} - 2\dot{Y} - X = -\frac{(1-\mu)}{R_1^3}(X+\mu) - \frac{\mu}{R_2^3}(X-(1-\mu)), \tag{2.3a}$$

$$\ddot{Y} + 2\dot{X} - Y = -\frac{(1-\mu)}{R_1^3}Y - \frac{\mu}{R_2^3}Y, \tag{2.3b}$$

$$\ddot{Z} = -\frac{(1-\mu)}{R_1^3}Z - \frac{\mu}{R_2^3}Z, \tag{2.3c}$$

where $\dot{X} = \frac{dX}{d\tau}$, $\dot{Y} = \frac{dY}{d\tau}$, $\dot{Z} = \frac{dZ}{d\tau}$ and $\ddot{X} = \frac{d^2X}{d\tau^2}$, $\ddot{Y} = \frac{d^2Y}{d\tau^2}$, $\ddot{Z} = \frac{d^2Z}{d\tau^2}$. Then, the problem is basically defined with μ which depends on m_1 and m_2.

2.3 Equilibrium Points

The equilibrium points are the locations where the third body is at rest relative to rotating frame. There are no accelerations and velocities. So, the positions of the equilibrium points can be found by setting $\ddot{X} = \ddot{Y} = \ddot{Z} = 0$ and $\dot{X} = \dot{Y} = 0$ in the equations of motion;

$$0 = X - \frac{(1-\mu)}{R_1^3}(X+\mu) - \frac{\mu}{R_2^3}(X-(1-\mu)), \tag{2.4a}$$

$$0 = Y - \frac{(1-\mu)}{R_1^3}Y - \frac{\mu}{R_2^3}Y, \tag{2.4b}$$

$$0 = -\frac{(1-\mu)}{R_1^3}Z - \frac{\mu}{R_2^3}Z, \tag{2.4c}$$

Since $Z = 0$, equilibrium points should lie on x-y plane. Then, the Eqn. (2.4b) can be written as;

$$0 = Y\left(1 - \frac{(1-\mu)}{R_1^3} - \frac{\mu}{R_2^3}\right), \tag{2.5}$$

so that $Y = 0$ or $\frac{(1-\mu)}{R_1^3} + \frac{\mu}{R_2^3} = 1$. When $Y \neq 0$, the Eqn. (2.4a) turns into form of;

$$0 = \mu \left(\frac{1}{R_2^3} - 1 \right). \tag{2.6}$$

Since $\mu \neq 0$, $R_2^3 = 1$. Putting $R_2^3 = 1$ into $\frac{(1-\mu)}{R_1^3} + \frac{\mu}{R_2^3} = 1$ yields $R_1^3 = 1$. Then;

$$R_1^3 = \left[(X + \mu)^2 + Y^2 \right]^{3/2} = 1, \tag{2.7a}$$

$$R_2^3 = \left[(X - (1 - \mu))^2 + Y^2 \right]^{3/2} = 1. \tag{2.7b}$$

There are two equations with two unknowns, so it is solvable;

$$X = \frac{1}{2} - \mu, \quad Y = \pm \frac{\sqrt{3}}{2}. \tag{2.8}$$

Since $R_1 = R_2 = r_{12} = 1$, these two points are called as equilateral triangular equilibrium points, commonly known as L_4 and L_5 where L is referred to as a Lagrange point.

Next, we look for the equilibrium points when $Y = 0$. So, R_1^3 and R_2^3 would be;

$$R_1^3 = |X + \mu|^3, \tag{2.9a}$$

$$R_2^3 = |X - (1 - \mu)|^3. \tag{2.9b}$$

Then, the Eqn. (2.4a) is written in the functional form of;

$$f(\mu, X) = \frac{(1-\mu)}{|X+\mu|^3} (X + \mu) + \frac{\mu}{|X - (1-\mu)|^3} (X - (1 - \mu)) - X = 0. \tag{2.10}$$

The roots of the function f for a chosen μ give the positions of equilibrium points along the x-axis. The plot of X values with respect to μ values for the function f is given in Fig. 2.2. It is seen that the Eqn. (2.10) has three real roots for the chosen μ value. They are called as collinear equilibrium points, commonly known as L_1, L_2 and L_3. Quantatively, the roots can be calculated by using numerical root finding methods like Bisection or Newton-Raphson [35].

As a result, there are five equilibrium points in the CRTBP of which the locations depend on the value of μ. The gravitational and centrifugal forces balance each other at those points so that the third body is at rest relative to rotating frame. Geometry of the equilibrium points is given in Fig. 2.3.

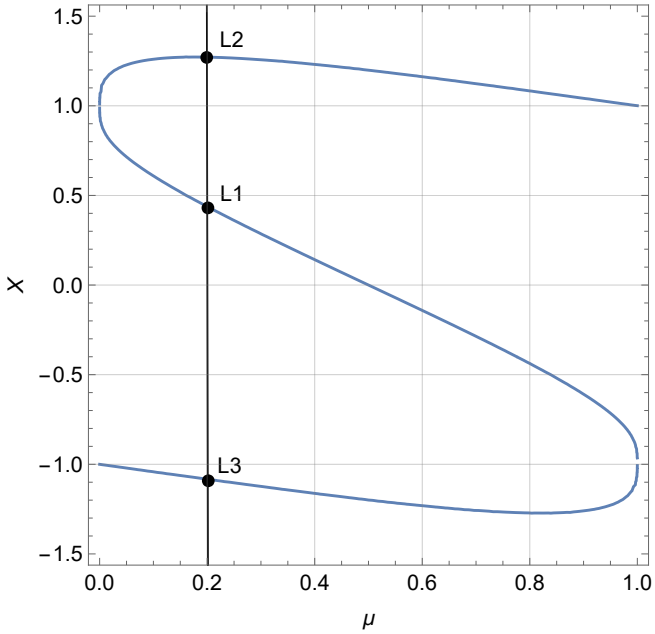

Figure 2.2: Plot of $f(\mu, X)$.

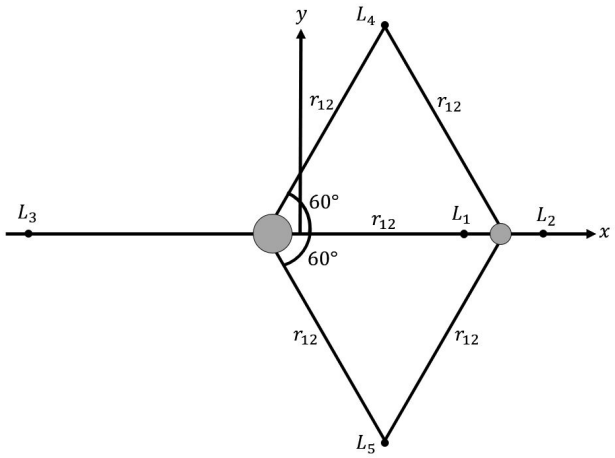

Figure 2.3: Geometry of the Lagrange points.

2.4 The Jacobi Constant

There is a constant of motion in CRTBP, commonly known as Jacobi constant, which can be obtained by multiplying Eqns. (2.3a), (2.3b) and (2.3c) with $\dot{X}$, $\dot{Y}$ and $\dot{Z}$, respectively. The derivation is rather straightforward, so it is not given here explicitly. One may look Section 2.12 in [34] for the detailed derivation. Jacobi constant, C, is

given as;

$$C = \frac{1}{2}\left(\dot{X}^2 + \dot{Y}^2 + \dot{Z}^2\right) - \frac{1}{2}\left(X^2 + Y^2\right) - \frac{(1-\mu)}{R_1} - \frac{\mu}{R_2}. \tag{2.11}$$

The first term is the kinetic energy per unit mass of the third body, the second term is the potential energy per unit mass due to centrifugal force and the last terms are the gravitational potential energies due to two massive bodies. Since the Coriolis force is perpendicular to the velocity direction, it does not do work. Jacobi constant can be considered as the total energy of the third body relative to rotating frame.

2.4.1 Possible Classes of Motion

In order to understand the various possibilities of motion qualitatively, it is useful to study the effective potential which is given with the sum of the centrifugal and the gravitational potentials;

$$U_{eff} = -\frac{1}{2}\left(X^2 + Y^2\right) - \frac{(1-\mu)}{R_1} - \frac{\mu}{R_2}. \tag{2.12}$$

Then, the Jacobi constant is written as;

$$C = T + U_{eff}, \tag{2.13}$$

where T is the kinetic energy per unit mass. Since the kinetic energy cannot be negative, the allowed region for the motion of the third body is defined with;

$$C - U_{eff} \geq 0. \tag{2.14}$$

To understand the possible motions better, a plot of the effective potential with respect to X and Y for $\mu = 0.2$ is given in Fig. 2.4. Take a horizontal surface corresponding to a Jacobi constant, then the allowed region for the motion would be $C \geq U_{eff}$. Since $\vec{F} = -\nabla U_{eff}$, the location of the equilibrium points X_0, Y_0 and Z_0 can be interpreted as;

$$\nabla U_{eff}|_{X_0, Y_0, Z_0 = 0}. \tag{2.15}$$

Next, we look for the Jacobi constant of the equilibrium points and the corresponding realms of motion. The boundary between the allowed and the forbidden regions is represented with the zero velocity curve which is defined as;

$$C = U_{eff}. \tag{2.16}$$

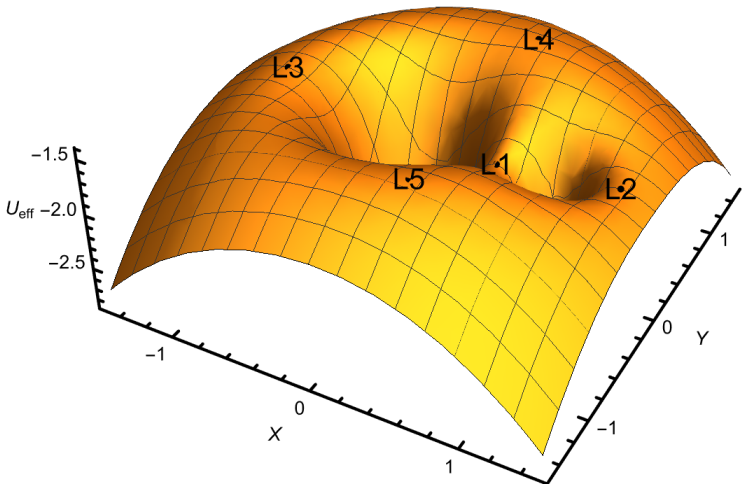

Figure 2.4: Plot of U_{eff} with respect to X and Y for $\mu = 0.2$.

The zero velocity curves for the Jacobi constants of equilibrium points and corresponding realms of motion are given in Fig. 2.5. The realms of motion are sometimes called as Hill's Region. In Fig. 2.5, those regions are shown with white color so that shaded regions are forbidden for the motion. From the Fig. 2.5, it is clearly seen that the Jacobi constants of the equilibrium points are ordered as $C_{L1} < C_{L2} < C_{L3} < C_{L4} = C_{L5}$. Then, the realms of motion can be classified as follows;

- $C < C_{L1}$: A particle near m_1 or m_2 is enclosed by the zero velocity curve so there is no transition between m_1 and m_2 realms. Also, a particle in the exterior realm which is outside the zero velocity curve cannot pass to the interior realm of m_1 and m_2.

- $C_{L1} < C < C_{L2}$: A neck is opened around L_1, so the particle can travel between m_1 and m_2 realms. However, there is no transition between the interior and the exterior realms.

- $C_{L2} < C < C_{L3}$: A neck is opened around L_2, so the particle can travel between the interior and the exterior realms via this neck. It is possible to escape from the interior realm with a Jacobi constant slightly larger than C_{L2}.

- $C_{L3} < C < C_{L4} = C_{L5}$: A neck is opened around L_3, so the particle can travel between the interior and the exterior realms via the necks around L_2 or L_3.
- $C_{L4} = C_{L5} < C$: All the regions on the x-y plane are accesible.

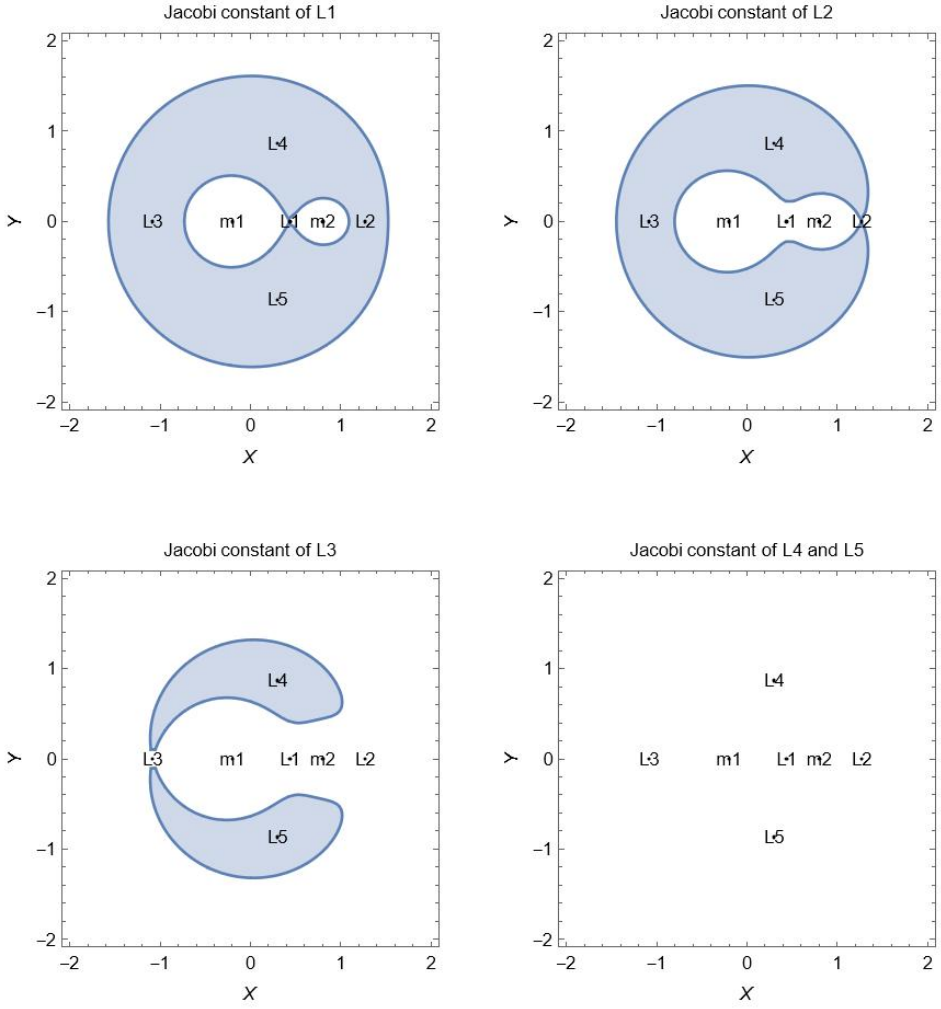

Figure 2.5: Realms of motion for the Jacobi constants of equilibrium points with $\mu = 0.2$.

CHAPTER 3

STABILITY OF THE EQUILIBRIUM POINTS

3.1 Linearization

In order to understand the local orbit structures, motion in the vicinity of the equilibrium points is investigated via linear stability analysis.

The equations of motion of CRTBP can be written with use of effective potential;

$$\ddot{X} - 2\dot{Y} = -\frac{\partial U_{eff}}{\partial X}, \tag{3.1a}$$

$$\ddot{Y} + 2\dot{X} = -\frac{\partial U_{eff}}{\partial Y}, \tag{3.1b}$$

$$\ddot{Z} = -\frac{\partial U_{eff}}{\partial Z}. \tag{3.1c}$$

Then, small perturbations, η, γ, ζ are applied to the equilibrium point, X_0, Y_0, Z_0;

$$X_p = X_0 + \eta, \tag{3.2a}$$

$$Y_p = Y_0 + \gamma, \tag{3.2b}$$

$$Z_p = Z_0 + \zeta. \tag{3.2c}$$

So, motion of a particle near the equilibrium point can be obtained by putting X_p, Y_p, Z_p to the equations of motion in Eqns. (3.1);

$$\ddot{\eta} - 2\dot{\gamma} = -\left.\frac{\partial U_{eff}}{\partial X}\right|_{X_p,Y_p,Z_p}, \tag{3.3a}$$

$$\ddot{\gamma} + 2\dot{\eta} = -\left.\frac{\partial U_{eff}}{\partial Y}\right|_{X_p,Y_p,Z_p}, \tag{3.3b}$$

$$\ddot{\zeta} = -\left.\frac{\partial U_{eff}}{\partial Z}\right|_{X_p,Y_p,Z_p}. \tag{3.3c}$$

Next, the right hand side of Eqns. (3.3) is linearized by using first order multivariable Taylor series expansion around the equilibrium point;

$$\left.\frac{\partial U_{eff}}{\partial X}\right|_{X_p,Y_p,Z_p} = \left.\frac{\partial U_{eff}}{\partial X}\right|_{X_0,Y_0,Z_0} + \eta\left.\frac{\partial^2 U_{eff}}{\partial X^2}\right|_{X_0,Y_0,Z_0} + \gamma\left.\frac{\partial}{\partial Y}\left(\frac{\partial U_{eff}}{\partial X}\right)\right|_{X_0,Y_0,Z_0} + \zeta\left.\frac{\partial}{\partial Z}\left(\frac{\partial U_{eff}}{\partial X}\right)\right|_{X_0,Y_0,Z_0} + \mathcal{O}\left(\eta^2,\gamma^2,\zeta^2,\eta\gamma,\eta\zeta,\gamma\zeta\right), \tag{3.4a}$$

$$\left.\frac{\partial U_{eff}}{\partial Y}\right|_{X_p,Y_p,Z_p} = \left.\frac{\partial U_{eff}}{\partial Y}\right|_{X_0,Y_0,Z_0} + \eta\left.\frac{\partial}{\partial X}\left(\frac{\partial U_{eff}}{\partial Y}\right)\right|_{X_0,Y_0,Z_0} + \gamma\left.\frac{\partial^2 U_{eff}}{\partial Y^2}\right|_{X_0,Y_0,Z_0} + \zeta\left.\frac{\partial}{\partial Z}\left(\frac{\partial U_{eff}}{\partial Y}\right)\right|_{X_0,Y_0,Z_0} + \mathcal{O}\left(\eta^2,\gamma^2,\zeta^2,\eta\gamma,\eta\zeta,\gamma\zeta\right), \tag{3.4b}$$

$$\left.\frac{\partial U_{eff}}{\partial Z}\right|_{X_p,Y_p,Z_p} = \left.\frac{\partial U_{eff}}{\partial Z}\right|_{X_0,Y_0,Z_0} + \eta\left.\frac{\partial}{\partial X}\left(\frac{\partial U_{eff}}{\partial Z}\right)\right|_{X_0,Y_0,Z_0} + \gamma\left.\frac{\partial}{\partial Y}\left(\frac{\partial U_{eff}}{\partial Z}\right)\right|_{X_0,Y_0,Z_0} + \zeta\left.\frac{\partial^2 U_{eff}}{\partial Z^2}\right|_{X_0,Y_0,Z_0} + \mathcal{O}\left(\eta^2,\gamma^2,\zeta^2,\eta\gamma,\eta\zeta,\gamma\zeta\right). \tag{3.4c}$$

Since η, γ, ζ are the small perturbations, higher order terms are neglected in the expansion. Recall that $\nabla U_{eff} = 0$ at the equilibrium points, so first terms in the expansions vanish. Also, all the equilibrium points lie on the x-y plane, so $Z_0 = 0$. Then, the other terms are given as follows;

$$\left.\frac{\partial^2 U_{eff}}{\partial X^2}\right|_{X_0,Y_0,Z_0} = -1 - \mu\left(\frac{3\left(X_0-(1-\mu)\right)^2}{R_2^5} - \frac{1}{R_2^3}\right) - (1-\mu)\left(\frac{3\left(X_0+\mu\right)^2}{R_1^5} - \frac{1}{R_1^3}\right), \tag{3.5a}$$

$$\left.\frac{\partial^2 U_{eff}}{\partial Y^2}\right|_{X_0,Y_0,Z_0} = -1 - \mu\left(\frac{3Y_0^2}{R_2^5} - \frac{1}{R_2^3}\right) - (1-\mu)\left(\frac{3Y_0^2}{R_1^5} - \frac{1}{R_1^3}\right), \tag{3.5b}$$

$$\left.\frac{\partial^2 U_{eff}}{\partial Z^2}\right|_{X_0,Y_0,Z_0} = -\mu\left(-\frac{1}{R_2^3}\right) - (1-\mu)\left(-\frac{1}{R_1^3}\right), \tag{3.5c}$$

$$\frac{\partial^2 U_{eff}}{\partial Y \partial X} = \left.\frac{\partial^2 U_{eff}}{\partial X \partial Y}\right|_{X_0,Y_0,Z_0} = -\mu\frac{3\left(X_0-(1-\mu)\right)Y_0}{R_2^5} - (1-\mu)\frac{3\left(X_0+\mu\right)Y_0}{R_1^5}, \tag{3.5d}$$

$$\frac{\partial^2 U_{eff}}{\partial Z \partial X} = \frac{\partial^2 U_{eff}}{\partial X \partial Z} = \frac{\partial^2 U_{eff}}{\partial Z \partial Y} = \left.\frac{\partial^2 U_{eff}}{\partial Y \partial Z}\right|_{X_0,Y_0,Z_0} = 0, \tag{3.5e}$$

where $R_1 = \left[\left(X_0+\mu\right)^2 + Y_0^2\right]^{1/2}$ and $R_2 = \left[\left(X_0-(1-\mu)\right)^2 + Y_0^2\right]^{1/2}$. The linear approximation of the equations of motion in the vicinity of an equilibrium point is

written as;

$$\ddot{\eta} - 2\dot{\gamma} = -\eta \frac{\partial^2 U_{eff}}{\partial X^2}\bigg|_{X_0,Y_0,Z_0} - \gamma \frac{\partial^2 U_{eff}}{\partial Y \partial X}\bigg|_{X_0,Y_0,Z_0}, \tag{3.6a}$$

$$\ddot{\gamma} + 2\dot{\eta} = -\eta \frac{\partial^2 U_{eff}}{\partial X \partial Y}\bigg|_{X_0,Y_0,Z_0} - \gamma \frac{\partial^2 U_{eff}}{\partial Y^2}\bigg|_{X_0,Y_0,Z_0}, \tag{3.6b}$$

$$\ddot{\zeta} = -\zeta \frac{\partial^2 U_{eff}}{\partial Z^2}\bigg|_{X_0,Y_0,Z_0}. \tag{3.6c}$$

Since $\frac{\partial^2 U_{eff}}{\partial Z^2}\big|_{X_0,Y_0,Z_0} > 0$, perturbation along the z-axis yields simple harmonic motion. So, the system is stable against the perturbation in the out-of plane direction. In fact, this expected because m_1 and m_2 move in the x-y plane and force the particle to be on the this plane. In order to solve Eqns. (3.6a) and (3.6b), they are reduced to first order ordinary differential equations by using the following auxiliary variables;

$$y_1 = \eta, \quad y_2 = \gamma, \quad y_3 = \dot{\eta}, \quad y_4 = \dot{\gamma}. \tag{3.7}$$

Then, the set of first order ordinary differential equations can be written as;

$$\dot{y}_1 = y_3, \tag{3.8a}$$

$$\dot{y}_2 = y_4, \tag{3.8b}$$

$$\dot{y}_3 = -y_1 \frac{\partial^2 U_{eff}}{\partial X^2}\bigg|_{X_0,Y_0,Z_0} - y_2 \frac{\partial^2 U_{eff}}{\partial Y \partial X}\bigg|_{X_0,Y_0,Z_0} + 2y_4, \tag{3.8c}$$

$$\dot{y}_4 = -y_1 \frac{\partial^2 U_{eff}}{\partial X \partial Y}\bigg|_{X_0,Y_0,Z_0} - y_2 \frac{\partial^2 U_{eff}}{\partial Y^2}\bigg|_{X_0,Y_0,Z_0} - 2y_3. \tag{3.8d}$$

The matrix form of Eqns. (3.8) would be;

$$\begin{bmatrix} \dot{y}_1 \\ \dot{y}_2 \\ \dot{y}_3 \\ \dot{y}_4 \end{bmatrix} = \begin{bmatrix} 0 & 0 & 1 & 0 \\ 0 & 0 & 0 & 1 \\ -\frac{\partial^2 U_{eff}}{\partial X^2}\Big|_{X_0,Y_0,Z_0} & -\frac{\partial^2 U_{eff}}{\partial Y \partial X}\Big|_{X_0,Y_0,Z_0} & 0 & 2 \\ -\frac{\partial^2 U_{eff}}{\partial X \partial Y}\Big|_{X_0,Y_0,Z_0} & -\frac{\partial^2 U_{eff}}{\partial Y^2}\Big|_{X_0,Y_0,Z_0} & -2 & 0 \end{bmatrix} \begin{bmatrix} y_1 \\ y_2 \\ y_3 \\ y_4 \end{bmatrix}. \tag{3.9}$$

The ansatz for the solution of $\dot{\vec{y}} = M\vec{y}$ in Eqn. (3.9) is;

$$\vec{y} = \vec{u}e^{\lambda\tau}. \tag{3.10}$$

Then, the general solution of Eqn. (3.9) is given as;

$$\vec{y} = c_1\vec{u}_1 e^{\lambda_1\tau} + c_2\vec{u}_2 e^{\lambda_2\tau} + c_3\vec{u}_3 e^{\lambda_3\tau} + c_4\vec{u}_4 e^{\lambda_4\tau}, \tag{3.11}$$

where c_1, c_2, c_3, c_4 are arbitrary coefficients determined by the initial conditions, λ_1, λ_2, λ_3, λ_4 are the eigenvalues of the matrix M and $\vec{u}_1$, $\vec{u}_2$, $\vec{u}_3$, $\vec{u}_4$ are the corresponding eigenvectors. The stability and the flow near the equilibrium points can be investigated by using the eigenvalues and the eigenvectors.

3.2 Stability of the Triangular Equilibrium Points

Recall that the positions of the triangular equilibrium points are;

$$X_0 = \frac{1}{2} - \mu, \quad Y_0 = \pm\frac{\sqrt{3}}{2}, \quad Z_0 = 0. \tag{3.12}$$

Then, the elements of the matrix M would be;

$$\left.\frac{\partial^2 U_{eff}}{\partial X^2}\right|_{X_0,Y_0,Z_0} = -\frac{3}{4}, \tag{3.13a}$$

$$\left.\frac{\partial^2 U_{eff}}{\partial Y^2}\right|_{X_0,Y_0,Z_0} = -\frac{9}{4}, \tag{3.13b}$$

$$\frac{\partial^2 U_{eff}}{\partial X \partial Y} = \left.\frac{\partial^2 U_{eff}}{\partial Y \partial X}\right|_{X_0,Y_0,Z_0} = \pm\frac{3\sqrt{3}}{4}(2\mu - 1). \tag{3.13c}$$

Therefore, the matrix M is;

$$M = \begin{bmatrix} 0 & 0 & 1 & 0 \\ 0 & 0 & 0 & 1 \\ \frac{3}{4} & \pm\frac{3\sqrt{3}}{4}(1-2\mu) & 0 & 2 \\ \pm\frac{3\sqrt{3}}{4}(1-2\mu) & \frac{9}{4} & -2 & 0 \end{bmatrix}. \tag{3.14}$$

The characteristic equation, $\det(M - \lambda I_n) = 0$, of matrix M is;

$$\lambda^4 + \lambda^2 + \frac{27\mu}{4} - \frac{27\mu^2}{4} = 0. \tag{3.15}$$

So, the eigenvalues are;

$$\lambda_{1,2} = \pm\sqrt{\left(\frac{\sqrt{27\mu^2 - 27\mu + 1} - 1}{2}\right)}, \tag{3.16a}$$

$$\lambda_{3,4} = \pm\sqrt{\left(\frac{-\sqrt{27\mu^2 - 27\mu + 1} - 1}{2}\right)}. \tag{3.16b}$$

To understand the possible eigenvalue cases better, a plot of $p(\mu) = 27\mu^2 - 27\mu + 1$ is given in Fig. 3.1.

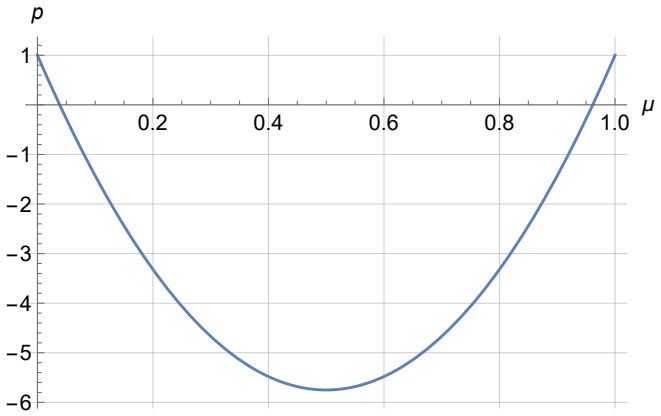

Figure 3.1: Plot of $p(\mu)$.

The roots of $p(\mu)$ are;

$$\mu = \frac{1}{2} - \frac{\sqrt{69}}{18} \approx 0.03852 \quad \text{and} \quad \mu = \frac{1}{2} + \frac{\sqrt{69}}{18} \approx 0.96148. \tag{3.17}$$

The smaller root is also known as Routh's or Gascheau's value, μ_G, [36]. Eigenvalues are purely imaginary for the μ values of;

$$0 < \mu < \mu_G \quad \text{and} \quad 1 - \mu_G < \mu < 1. \tag{3.18}$$

Since the purely imaginary eigenvalues yield sine and cosine terms in Eqn. (3.11), there are periodic orbits around the triangular equilibrium points for the μ values satisfying the Eqn. (3.18). In fact, this type of equilibrium points are called as center in the terminology of stability.

The periodic orbits in the vicinity of triangular equilibrium points are called as Tadpole orbits due to their shapes. In our solar system, for example;

$$\text{Sun-Earth System: } \mu_{SE} \approx 3.004 \times 10^{-6}, \tag{3.19a}$$

$$\text{Sun-Jupiter System: } \mu_{SJ} \approx 9.538 \times 10^{-4}, \tag{3.19b}$$

$$\text{Earth-Moon System: } \mu_{EM} \approx 0.01215. \tag{3.19c}$$

Since they are less than μ_G, the triangular equilibrium points exist in the stable region for those systems. The small celestial bodies placed near L_4 or L_5 are known as Trojans, so there are Earth Trojans for the Sun-Earth system and the Jupiter Trojans for the Sun-Jupiter system.

Initial conditions of the Tadpole orbits can be obtained by calculating the matrix M for a given μ, then putting the eigenvalues and corresponding eigenvectors of matrix M to the Eqn. (3.11) and finally equating $\tau = 0$. In Fig. 3.2, the Tadpole orbits are generated by considering the coefficients $c_2 = c_3 = c_4 = 0$ and $c_1 = [0.001, 0.002, 0.003, 0.004, 0.005]$ and solving the nonlinear equations of motion of CRTBP for the chosen initial conditions by using the MATLAB ode45 solver with absolute and relative tolerances of 10^{-13}.

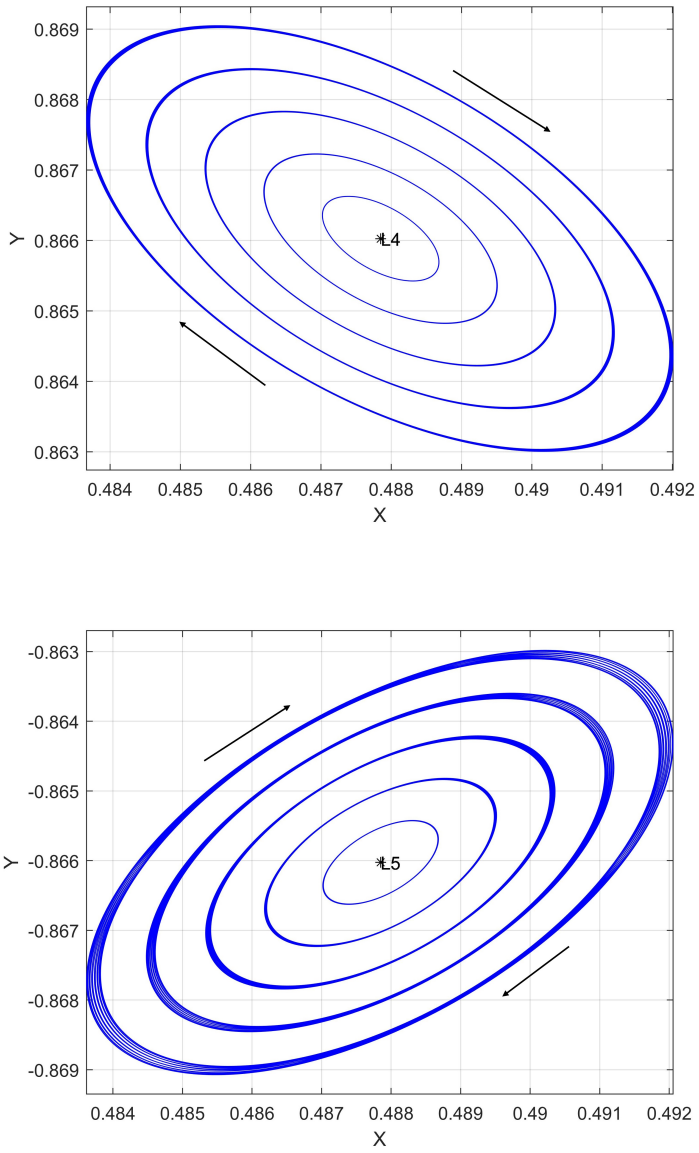

Figure 3.2: Example of the Tadpole orbits for the Earth-Moon system.

Since the initial conditions of the Tadpole orbits are obtained with linear approximation near the equilibrium point, nonlinear effects disturb the periodicity as the initial condition is getting away from the equilibrium point.

In the interval of $\mu_G < \mu < 1 - \mu_G$, eigenvalues are complex numbers with nonzero real parts such that two of them have positive and other two have negative real parts. Therefore, triangular equilibrium points are linearly unstable for those μ values.

3.3 Stability of the Collinear Equilibrium Points

The collinear equilibrium points lie on the x-axis, so $Y_0 = 0$ and $Z_0 = 0$. Then the elements of the matrix M would be;

$$\left.\frac{\partial^2 U_{eff}}{\partial X^2}\right|_{X_0,Y_0,Z_0} = -1 - \frac{2\mu}{|X_0 - (1-\mu)|^3} - \frac{2(1-\mu)}{|X_0 + \mu|^3}, \tag{3.20a}$$

$$\left.\frac{\partial^2 U_{eff}}{\partial Y^2}\right|_{X_0,Y_0,Z_0} = -1 + \frac{\mu}{|X_0 - (1-\mu)|^3} + \frac{(1-\mu)}{|X_0 + \mu|^3}, \tag{3.20b}$$

$$\frac{\partial^2 U_{eff}}{\partial X \partial Y} = 0. \tag{3.20c}$$

Therefore, the matrix M is;

$$M = \begin{bmatrix} 0 & 0 & 1 & 0 \\ 0 & 0 & 0 & 1 \\ 1+2\alpha & 0 & 0 & 2 \\ 0 & 1-\alpha & -2 & 0 \end{bmatrix}, \tag{3.21}$$

where $\alpha = \frac{\mu}{|X_0-(1-\mu)|^3} + \frac{(1-\mu)}{|X_0+\mu|^3}$. The characteristic equation, $\det(M - \lambda I_n) = 0$, of matrix M is;

$$\lambda^4 + (2-\alpha)\lambda^2 + (1+2\alpha)(1-\alpha) = 0. \tag{3.22}$$

Let $\beta = \lambda^2$, then;

$$p(\beta) = \beta^2 + (2-\alpha)\beta + (1+2\alpha)(1-\alpha) = 0. \tag{3.23}$$

Since $\frac{d^2p}{d\beta^2} > 0$, $p(\beta)$ is concave up. Then, we look for the sign of the last term, $(1+2\alpha)(1-\alpha)$, to identify the roots. The effective potential plots given in Fig. 3.3 are used to decide signs.

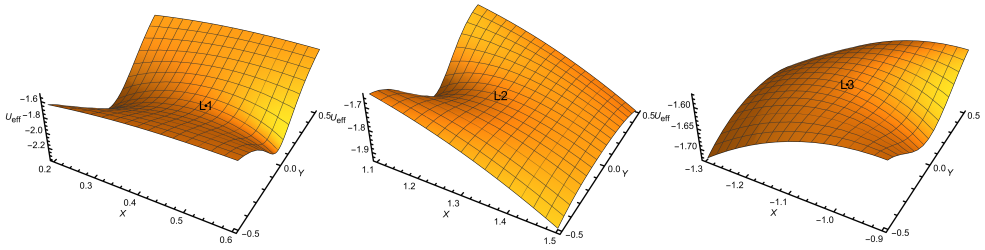

Figure 3.3: Effective potential plots around collinear equilibrium points for $\mu = 0.2$.

Remember that;

$$1 + 2\alpha = -\frac{\partial^2 U_{eff}}{\partial X^2}\bigg|_{X_0,Y_0,Z_0}, \tag{3.24a}$$

$$1 - \alpha = -\frac{\partial^2 U_{eff}}{\partial Y^2}\bigg|_{X_0,Y_0,Z_0}. \tag{3.24b}$$

According to Fig. 3.3, it can be said that $\frac{\partial^2 U_{eff}}{\partial X^2}\big|_{X_0,Y_0,Z_0} < 0$ and $\frac{\partial^2 U_{eff}}{\partial Y^2}\big|_{X_0,Y_0,Z_0} > 0$. Then;

$$1 + 2\alpha > 0, \tag{3.25a}$$

$$1 - \alpha < 0. \tag{3.25b}$$

Since $p\,(\beta)$ is concave up and $(1 + 2\alpha)\,(1 - \alpha) < 0$, $p\,(\beta)$ should have two real roots with one positive and one negative. Therefore, the roots of $p\,(\beta)$ are;

$$\beta_1 = \frac{\alpha - 2 + \sqrt{9\alpha^2 - 8\alpha}}{2} > 0, \tag{3.26a}$$

$$\beta_2 = \frac{\alpha - 2 - \sqrt{9\alpha^2 - 8\alpha}}{2} < 0. \tag{3.26b}$$

Then, the eigenvalues are;

$$\lambda_{1,2} = \pm\sqrt{\beta_1} = \pm\chi, \tag{3.27a}$$

$$\lambda_{3,4} = \pm\sqrt{\beta_2} = \pm i\nu, \tag{3.27b}$$

where $\chi = \sqrt{\beta_1} > 0$ and $\nu = \sqrt{-\beta_2} > 0$. To obtain the motion near the equilibrium points, corresponding eigenvectors are calculated as follows;

$$\vec{u}_1 = \begin{bmatrix} 1 \\ -\sigma \\ \chi \\ -\chi\sigma \end{bmatrix}, \vec{u}_2 = \begin{bmatrix} 1 \\ \sigma \\ -\chi \\ -\chi\sigma \end{bmatrix}, \vec{u}_3 = \begin{bmatrix} 1 \\ -i\kappa \\ i\nu \\ \nu\kappa \end{bmatrix}, \vec{u}_4 = \begin{bmatrix} 1 \\ i\kappa \\ -i\nu \\ \nu\kappa \end{bmatrix}, \tag{3.28}$$

where $\sigma = \frac{2\chi}{\chi^2-(1-\alpha)} > 0$ and $\kappa = -\left(\frac{\nu^2+(1+2\alpha)}{2\nu}\right) < 0$. The conventions given in [33] are used for representing the eigenvectors. Then, the equations of motion around collinear equilibrium points can be obtained by putting Eqn. (3.28) and Eqn. (3.27) to the Eqn. (3.11);

$$\eta = c_1 e^{\chi\tau} + c_2 e^{-\chi\tau} + c_3 e^{i\nu\tau} + c_4 e^{-i\nu\tau}, \tag{3.29a}$$

$$\gamma = -c_1\sigma e^{\chi\tau} + c_2\sigma e^{-\chi\tau} - c_3(i\kappa)e^{i\nu\tau} + c_4(i\kappa)e^{-i\nu\tau}. \tag{3.29b}$$

By expanding $e^{i\nu\tau}$, $e^{-i\nu\tau}$ and rearranging the terms, final form would be;

$$\eta(\tau) = c_1 e^{\chi\tau} + c_2 e^{-\chi\tau} + c_3\cos(\nu\tau) + c_4\sin(\nu\tau), \tag{3.30a}$$

$$\gamma(\tau) = -c_1\sigma e^{\chi\tau} + c_2\sigma e^{-\chi\tau} - c_4\kappa\cos(\nu\tau) + c_3\kappa\sin(\nu\tau). \tag{3.30b}$$

There are different types of motion depending on the initial condition. First, we look for the unstable manifold, $\gamma = -\sigma\eta$, and the stable manifold, $\gamma = \sigma\eta$, in Fig. 3.4 to understand the flow direction in the vicinity of collinear equilibrium points.

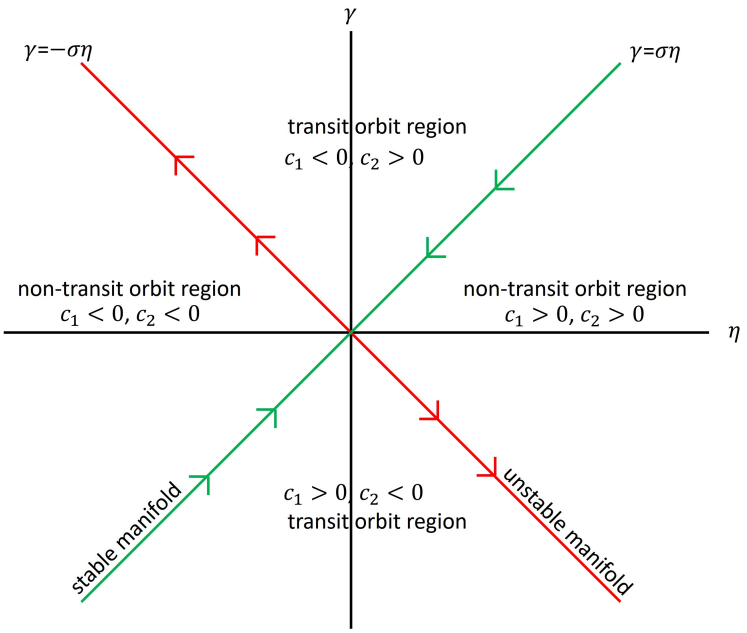

Figure 3.4: Flow directions and regions of possible motion in the vicinity of collinear equilibrium points.

In generating the examples of possible trajectories around the collinear equilibrium point, MATLAB ode45 solver is used with absolute and relative tolerances of 10^{-13}. The possible motions can be classified as follows;

- $\underline{c_1 = c_2 = 0}$: The periodic motion, commonly known as the Lyapunov orbit, occurs. The initial condition for the Lyapunov orbit can be obtained from Eqn. (3.30) by using the sine and cosine terms. Examples of the Lyapunov orbits around L_1 for the Earth-Moon system are given in Fig. 3.5 by setting the coefficients $c_1 = c_2 = c_4 = 0$ and $c_3 = [10^{-5}, 10^{-4}]$. In Fig. 3.5, it is seen that the linear approximation is valid as long as the initial condition is sufficiently close to the fixed point. As the initial condition is getting away, linear approximation does not hold and nonlinearities alter the periodicity. In order to obtain periodic orbits accurately, a numerical method called as differential correction is used. This method will be discussed detailed in the next chapter.

- $\underline{c_1 c_2 = 0}$: Asymptotic orbits to the Lyapunov orbit occur. If $c_1 = 0$ and $c_2 \neq 0$, asymptotic orbits are stable so the particle moves towards to the Lyapunov orbit. If $c_1 \neq 0$ and $c_2 = 0$, asymptotic orbits are unstable so particle moves away from the Lyapunov orbit. In fact, asymptotic orbits are the invariant manifold structures associated to the Lyapunov orbit. The systematic construction of those structures will be discussed in the next chapter. Examples of the stable and the unstable asymptotic orbits to the L_1 Lyapunov orbit of the Earth-Moon system are given in Fig. 3.6 by setting the coefficients $c_1 = c_4 = 0$ and $|c_2| = |c_3| = 10^{-5}$ for the stable orbits, $c_2 = c_4 = 0$ and $|c_1| = |c_3| = 10^{-5}$ for the unstable orbits.

- $\underline{c_1 c_2 > 0}$: Non-transit orbits occur. If $c_1 > 0$ and $c_2 > 0$, η is in the positive region and if $c_1 < 0$ and $c_2 < 0$, η is in the negative region. In both cases, γ is in between the lines $\gamma = -\sigma\eta$ and $\gamma = \sigma\eta$ so that particle cannot pass to different realms through the equilibrium point. Examples of the non-transit orbits around the Earth-Moon L_1 are given in Fig. 3.7 by setting the coefficients $c_3 = c_4 = 0$ and $|c_1| = |c_2| = 10^{-5}$.

- $\underline{c_1 c_2 < 0}$: Transit orbits occur. If $c_1 < 0$ and $c_2 > 0$, γ is in the positive region and if $c_1 > 0$ and $c_2 < 0$, γ is in the negative region. In both cases, η is in between the lines $\gamma = -\sigma\eta$ and $\gamma = \sigma\eta$ so that particle can pass through the equilibrium point. Examples of the transit orbits around the Earth-Moon L_1 are given in Fig. 3.8 by setting the coefficients $c_3 = c_4 = 0$ and $|c_1| = |c_2| = 10^{-5}$.

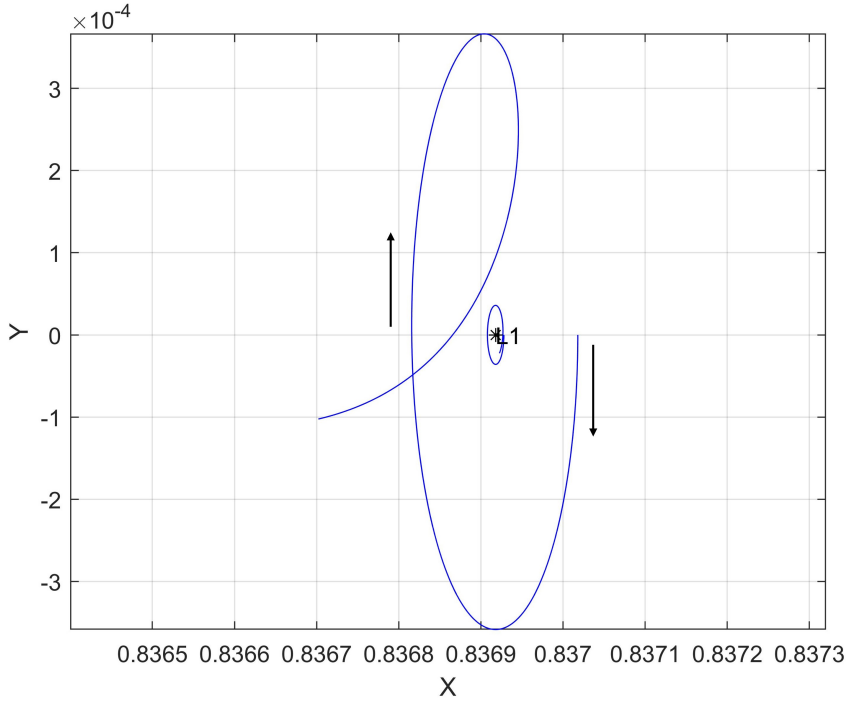

Figure 3.5: Lyapunov orbits around L_1 for the Earth-Moon system.

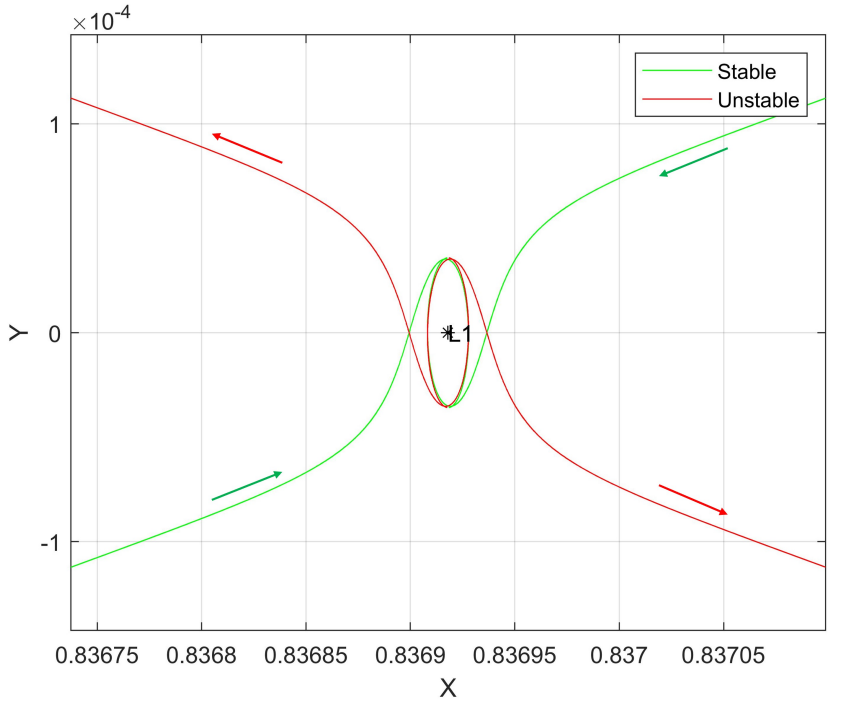

Figure 3.6: Asymptotic orbits to the L_1 Lyapunov orbit for the Earth-Moon system.

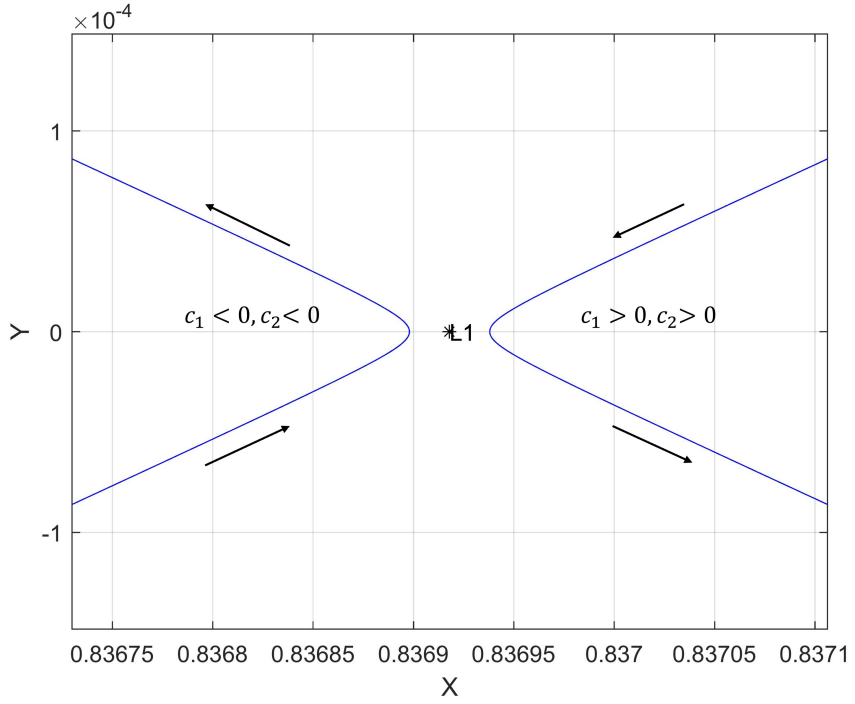

Figure 3.7: Non-transit orbits around L_1 for the Earth-Moon system.

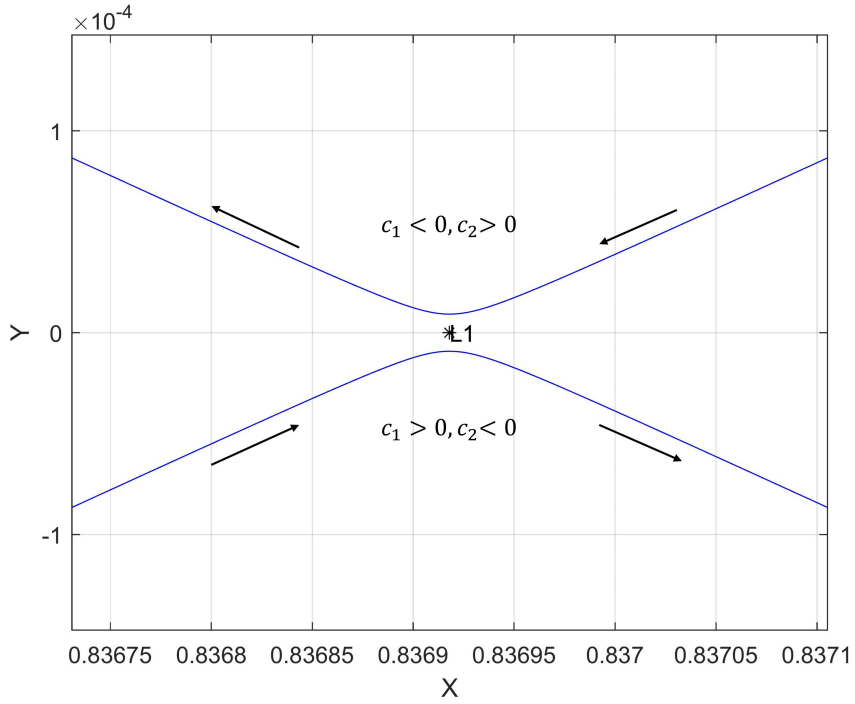

Figure 3.8: Transit orbits around L_1 for the Earth-Moon system.

CHAPTER 4

LYAPUNOV ORBITS AND THEIR GLOBAL CONNECTIONS

4.1 Differential Correction

In the previous chapter, it was seen that the linear approximation gives a rough initial condition to generate periodic orbits, particularly if the initial condition is away from the fixed point. In order to improve the initial condition and obtain periodic orbits in nonlinear equations, a method called as differential correction is used. In this method, some desired values and design variables are specified. Then, the design variables are corrected to achieve desired values in an iterative manner.

Consider;

$$f(\vec{y}(\tau_0), \tau) = \vec{y}(\tau), \tag{4.1}$$

where f represents the dynamics of the system including the equations of motion implicitly, and $\vec{y} = \left[X, Y, Z, \dot{X}, \dot{Y}, \dot{Z}\right]^T$. Then, small perturbations $\vec{y}_{pert}(\tau_0)$ and τ_{pert} are applied;

$$f(\vec{y}(\tau_0) + \vec{y}_{pert}(\tau_0), \tau + \tau_{pert}) = \vec{y}(\tau) + \vec{y}_{pert}(\tau), \tag{4.2}$$

where $\vec{y}_{pert}(\tau)$ is the perturbed state at time τ. The Taylor series expansion of f is given as;

$$f(\vec{y}(\tau_0)+\vec{y}_{pert}(\tau_0), \tau+\tau_{pert}) = f(\vec{y}(\tau_0), \tau)+\frac{\partial f(\vec{y}(\tau_0), \tau)}{\partial \vec{y}(\tau_0)}\vec{y}_{pert}(\tau_0)+\frac{\partial f(\vec{y}(\tau_0), \tau)}{\partial \tau}\tau_{pert}. \tag{4.3}$$

It is a first order linear approximation where higher order terms are neglected. By using Eqn. (4.1) and Eqn. (4.2), it is possible to rearrange Eqn. (4.3) as;

$$\vec{y}_{pert}(\tau) = \Phi(\tau, \tau_0)\vec{y}_{pert}(\tau_0) + \frac{\partial \vec{y}(\tau)}{\partial \tau}\tau_{pert}, \tag{4.4}$$

where $\Phi(\tau,\tau_0) = \frac{\partial \vec{y}(\tau)}{\partial \vec{y}(\tau_0)}$ is the State Transition Matrix (STM). Also, $\vec{y}_{pert}(\tau) = \vec{y}_{desired}(\tau) - \vec{y}_{propagated}(\tau)$, $\vec{y}_{pert}(\tau_0) = \vec{y}_{i+1}(\tau_0) - \vec{y}_i(\tau_0)$ and $\tau_{pert} = \tau_{i+1} - \tau_i$. The STM can be computed by using the following differential equation;

$$\dot{\Phi}(\tau,\tau_0) = \frac{\partial \dot{\vec{y}}(\tau)}{\partial \vec{y}(\tau_0)} = \frac{\partial \dot{\vec{y}}(\tau)}{\partial \vec{y}(\tau)} \frac{\partial \vec{y}(\tau)}{\partial \vec{y}(\tau_0)}, \tag{4.5a}$$

$$\dot{\Phi}(\tau,\tau_0) = A(\tau)\Phi(\tau,\tau_0), \tag{4.5b}$$

where $A(\tau)$ is;

$$A(\tau) = \frac{\partial \dot{\vec{y}}(\tau)}{\partial \vec{y}(\tau)} = \begin{bmatrix} 0 & 0 & 0 & 1 & 0 & 0 \\ 0 & 0 & 0 & 0 & 1 & 0 \\ 0 & 0 & 0 & 0 & 0 & 1 \\ -\frac{\partial^2 U_{eff}}{\partial X^2} & -\frac{\partial^2 U_{eff}}{\partial Y \partial X} & -\frac{\partial^2 U_{eff}}{\partial Z \partial X} & 0 & 2 & 0 \\ -\frac{\partial^2 U_{eff}}{\partial X \partial Y} & -\frac{\partial^2 U_{eff}}{\partial Y^2} & -\frac{\partial^2 U_{eff}}{\partial Z \partial Y} & -2 & 0 & 0 \\ -\frac{\partial^2 U_{eff}}{\partial X \partial Z} & -\frac{\partial^2 U_{eff}}{\partial Y \partial Z} & -\frac{\partial^2 U_{eff}}{\partial Z^2} & 0 & 0 & 0 \end{bmatrix}, \tag{4.6}$$

with the initial condition of $\Phi(\tau_0,\tau_0) = I_6$.

To generate the Lyapunov orbits by using the differential correction method, first the desired conditions for the existence of periodic orbits are investigated. Notice that the substitutions $\tau \to -\tau$ and $Y \to -Y$ does not change the equations of motion of CRTBP. So, the motion is symmetric with respect to the x-axis in the context of time reversibility. Suppose, a particle is initially placed on the x-axis and its velocity is perpendicular to the x-axis. Propagate the trajectory of this particle from the initial point forward in time until the next x-axis crossing and suppose the crossing occurs perpendicularly. Then, propagate the trajectory of the same particle from the initial point backward in time until the x-axis crossing, and here also it should cross the x-axis perpendicularly due to the symmetry. As a result, combination of each half of the trajectories yields a periodic orbit. Then, the desired conditions to have a periodic orbit can be given with the use of perpendicular x-axis crossing;

$$Y_{desired}(\tau) = 0 \quad \text{and} \quad \dot{X}_{desired}(\tau) = 0. \tag{4.7}$$

Also, the initial condition used for the differential correction method is given as;

$$\vec{y}(\tau_0) = \Big[X(\tau_0), 0, 0, 0, \dot{Y}(\tau_0), 0\Big]^T. \tag{4.8}$$

The initial guesses $X(\tau_0)$ and $\dot{Y}(\tau_0)$ are coming from the linear approximation given in Chapter 3. The $\dot{Y}(\tau_0)$ and τ are chosen as design variables so that they are corrected to achieve desired values. So, $\vec{y}_{pert}(\tau_0)$ in Eqn. (4.4) would be;

$$\vec{y}_{pert}(\tau_0) = \left[0, 0, 0, 0, \dot{Y}_{pert}(\tau_0), 0\right]^T, \tag{4.9}$$

and Eqn. (4.4) is written explicitly as;

$$\begin{bmatrix} X_{pert}(\tau) \\ Y_{pert}(\tau) \\ Z_{pert}(\tau) \\ \dot{X}_{pert}(\tau) \\ \dot{Y}_{pert}(\tau) \\ \dot{Z}_{pert}(\tau) \end{bmatrix} = \Phi_{6\times6}(\tau, \tau_0) \begin{bmatrix} 0 \\ 0 \\ 0 \\ 0 \\ \dot{Y}_{pert}(\tau_0) \\ 0 \end{bmatrix} + \begin{bmatrix} \dot{X}(\tau) \\ \dot{Y}(\tau) \\ \dot{Z}(\tau) \\ \ddot{X}(\tau) \\ \ddot{Y}(\tau) \\ \ddot{Z}(\tau) \end{bmatrix} \tau_{pert}. \tag{4.10}$$

Since the targeted variables are only $Y_{desired}(\tau)$ and $\dot{X}_{desired}(\tau)$, Eqn. (4.10) can be reduced to;

$$\begin{bmatrix} Y_{pert}(\tau) \\ \dot{X}_{pert}(\tau) \end{bmatrix} = \begin{bmatrix} \Phi_{2,5}(\tau, \tau_0) & \dot{Y}(\tau) \\ \Phi_{4,5}(\tau, \tau_0) & \ddot{X}(\tau) \end{bmatrix} \begin{bmatrix} \dot{Y}_{pert}(\tau_0) \\ \tau_{pert} \end{bmatrix}. \tag{4.11}$$

Then, taking the inverse yields;

$$\begin{bmatrix} \dot{Y}_{pert}(\tau_0) \\ \tau_{pert} \end{bmatrix} = \begin{bmatrix} \Phi_{2,5}(\tau, \tau_0) & \dot{Y}(\tau) \\ \Phi_{4,5}(\tau, \tau_0) & \ddot{X}(\tau) \end{bmatrix}^{-1} \begin{bmatrix} Y_{pert}(\tau) \\ \dot{X}_{pert}(\tau) \end{bmatrix}, \tag{4.12}$$

where $Y_{pert}(\tau) = Y_{desired}(\tau) - Y_{propagated}(\tau)$, $\dot{X}_{pert}(\tau) = \dot{X}_{desired}(\tau) - \dot{X}_{propagated}(\tau)$ and $\dot{Y}_{pert}(\tau_0) = \dot{Y}_{i+1}(\tau_0) - \dot{Y}_i(\tau_0)$, $\tau_{pert} = \tau_{i+1} - \tau_i$. Therefore, the design variables $\dot{Y}(\tau_0)$ and τ are calculated based on Eqn. (4.12) iteratively until the difference between desired and propagated values falls below the termination criteria.

Here and also in rest of the chapter, MATLAB ode45 solver is used with absolute and relative tolerances of 10^{-13} for the numerical integration. Examples of the differential correction process and the resulting Lyapunov orbit are given in Fig. 4.1 and Fig. 4.2. In this example, an L_1 Lyapunov orbit of the Earth-Moon system is constructed. The initial conditions that will be improved with differential correction is taken from the linearized equations of motion by considering $c_1 = c_2 = c_4 = 0$ and $c_3 = 0.001$.

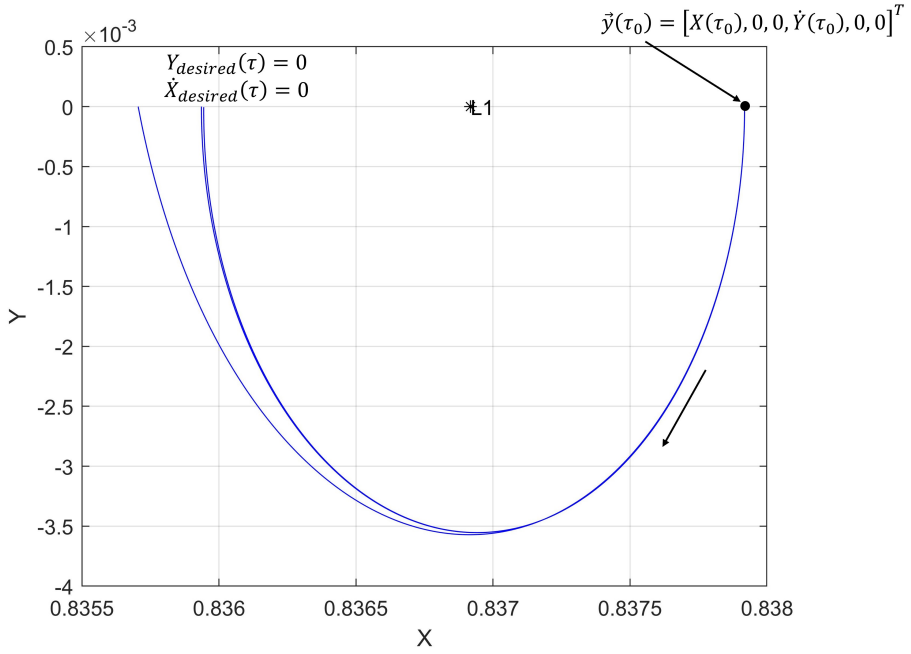

Figure 4.1: Differential correction process for the L_1 Lyapunov orbit of the Earth-Moon system.

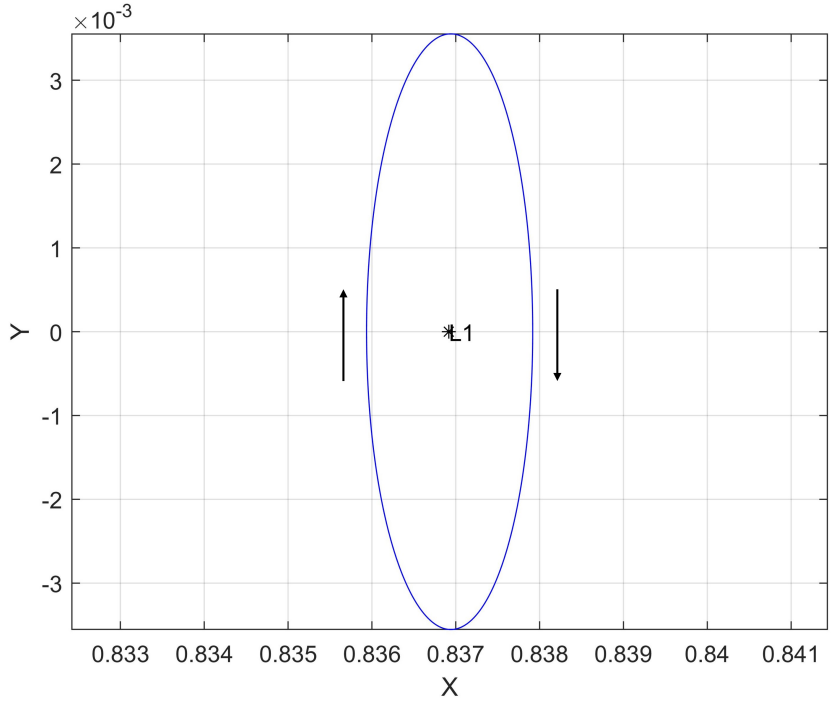

Figure 4.2: L_1 Lyapunov orbit of the Earth-Moon system obtained from the differential correction.

4.2 Continuation

In order to generate a family of Lyapunov orbits, continuation method is used. Each orbit in the family can be identified with certain parameters such as position or velocity at the perpendicular crossing point and also with Jacobi constant [37]. Continuation method is particularly useful to obtain the Lyapunov orbit corresponding to the desired Jacobi constant.

The initial Lyapunov orbit found from the differential correction is the starting point of the continuation method. A small perturbation is applied to the X_0 component of the initial condition as;

$$X_{0,perturbed} = X_0 + \Delta X, \tag{4.13}$$

at the perpendicular crossing point. Then, the differential correction is used with the perturbed X position, $X_{0,perturbed}$, and the initial guesses of $\dot{Y}_0$ and τ_0. Those initial guesses belong to the starting Lyapunov orbit. The outcome of the differential correction would be the updated $\dot{Y}_0$ and τ_0 of the $X_{0,perturbed}$. Therefore, another Lyapunov orbit is obtained corresponding to the perturbed position, $X_{0,perturbed}$. This process is repeated for each newly obtained Lyapunov orbit to reach a family of orbits. Here, the important point is the order of perturbation ΔX. This has to be small in order to make the continuation method more reliable by preventing the convergence of the differential correction method to a different family [37].

The family of L_1 Lyapunov orbits for the Earth-Moon system is given in Fig. 4.3. In addition, Jacobi constant of each orbit in the family and the corresponding initial conditions with the periods are given in Fig. 4.4 and Fig. 4.5, respectively. In order to calculate a Lyapunov orbit of a desired Jacobi constant, first the X_0 value corresponding to the desired Jacobi constant is extracted from Fig. 4.4. Then, the extracted X_0 value is used to find $\dot{Y}_0$ and period of the corresponding Lyapunov orbit from Fig. 4.5. Since the initial conditions and period are known, Lyapunov orbit of the desired Jacobi constant is generated. The family of L_2 and L_3 Lyapunov orbits can be calculated with the same manner.

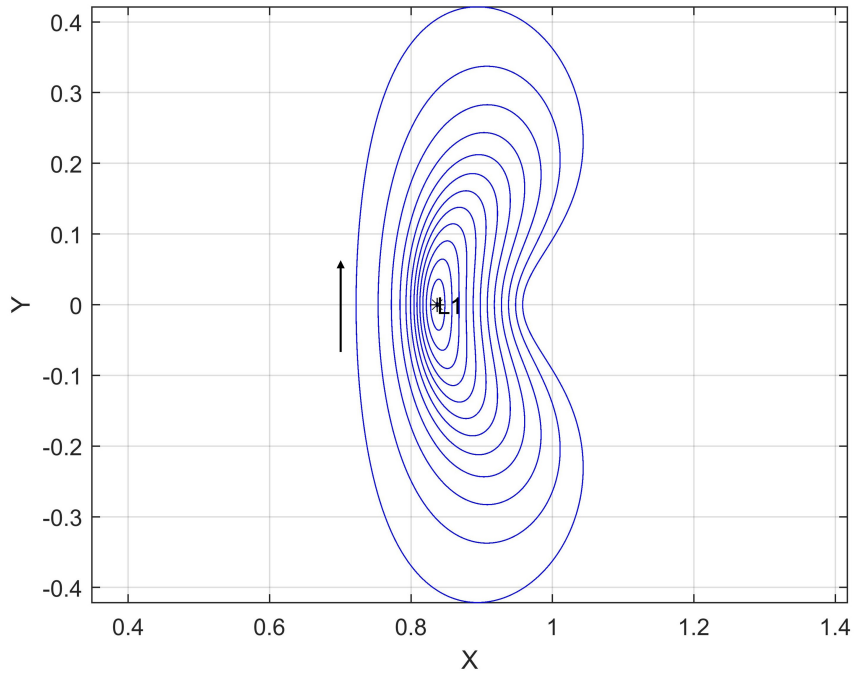

Figure 4.3: The family of L_1 Lyapunov orbits for the Earth-Moon system.

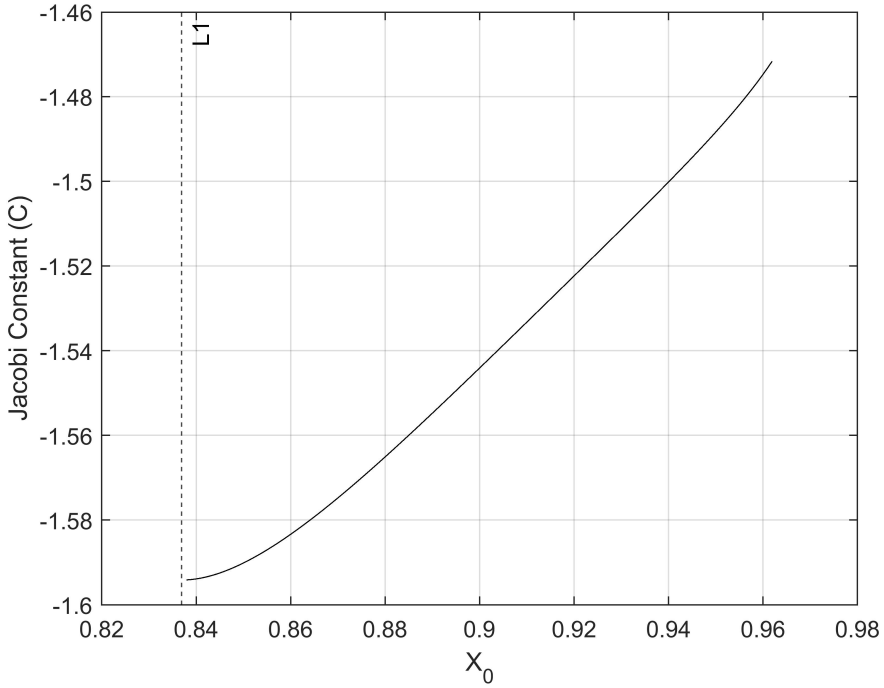

Figure 4.4: Jacobi constants of L_1 Lyapunov orbits family for the Earth-Moon system.

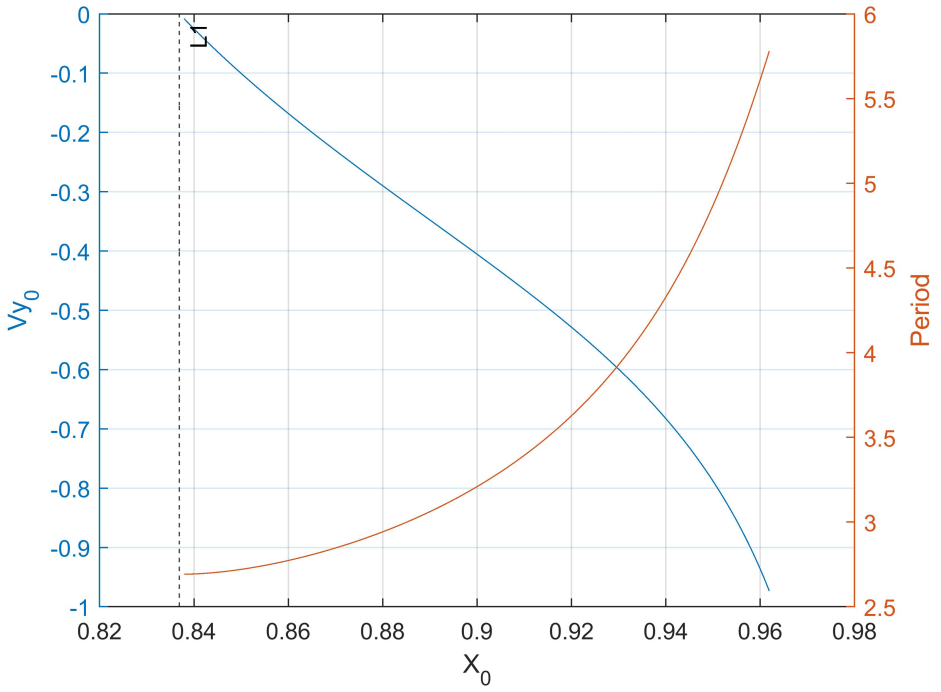

Figure 4.5: Initial conditions and periods of L_1 Lyapunov orbits family for the Earth-Moon system.

4.3 Poincaré Map

Poincaré Map is a useful tool to analyze the stability of the periodic orbits. Consider a surface that is transverse to the flow direction as given with S in Fig. 4.6. Then, the Poincaré Map, P, is defined by mapping from one intersection with surface S to the next. So;

$$P(\vec{x}_k) = \vec{x}_{k+1}. \tag{4.14}$$

Notice that $P(\vec{x}^*) = \vec{x}^*$ in Fig. 4.6 which means a periodic orbit can be considered as a fixed point in the mapping. This is particularly useful because investigating the stability of a periodic orbit becomes dealing with stability of a fixed point.

The following calculations are highly aligned with [38]. To analyze the stability, first a small perturbation $\vec{v}_0$ is applied to the fixed point;

$$P(\vec{x}^* + \vec{v}_0) = \vec{x}^* + \vec{v}_1. \tag{4.15}$$

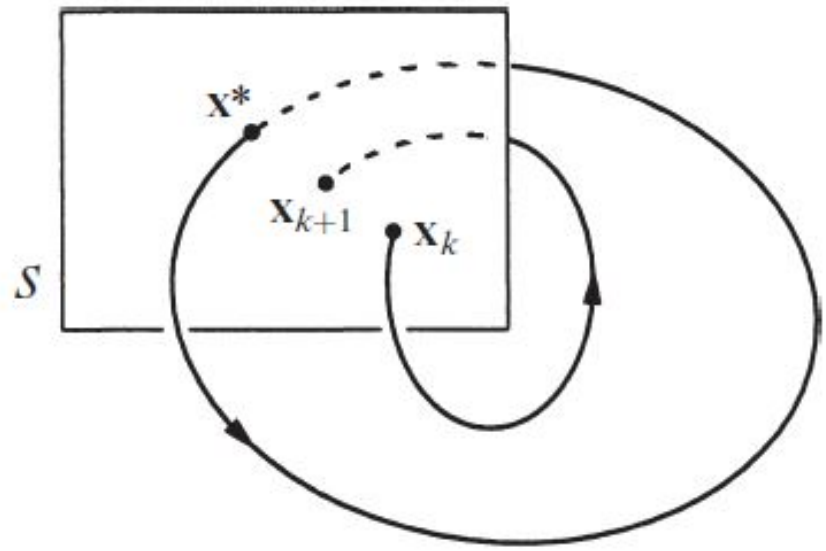

Figure 4.6: Illustration of the Poincaré Map [38].

Then, $P(\vec{x}^* + \vec{v}_0)$ is expanded around $\vec{x}^*$ by using Taylor series expansion;

$$P(\vec{x}^* + \vec{v}_0) = P(\vec{x}^*) + [DP(\vec{x}^*)]\,\vec{v}_0 + \mathcal{O}(||\vec{v}_0||^2). \tag{4.16}$$

After putting Eqn. (4.15) and $P(\vec{x}^*) = \vec{x}^*$ to the expansion, one reaches at;

$$\vec{v}_1 = [DP(\vec{x}^*)]\,\vec{v}_0. \tag{4.17}$$

Consider the following eigenvalue equation;

$$[DP(\vec{x}^*)]\,\vec{u}_j = \lambda_j \vec{u}_j, \tag{4.18}$$

where λ_j are the eigenvalues of $[DP(\vec{x}^*)]$ and $\vec{u}_j$ are the corresponding eigenvectors. Then, multiplication of Eqn. (4.17) with $\vec{u}_j$ yields;

$$\vec{v}_1 \vec{u}_j = \lambda_j \vec{v}_0 \vec{u}_j. \tag{4.19}$$

By rearranging the Eqn. (4.19), one can get;

$$(\vec{v}_1 - \lambda_j \vec{v}_0)\,\vec{u}_j = 0. \tag{4.20}$$

Since $\vec{u}_j \neq 0$, then;

$$\vec{v}_1 = \lambda_j \vec{v}_0. \tag{4.21}$$

The eigenvalues λ_j are also called as Characteristic or Floquet multipliers. They are used to assess the stability of the periodic orbits. The possible eigenvalue cases can be classified as follows;

- $|\lambda_j| > 1$: The given perturbation grows in the corresponding eigenvector direction, so the periodic orbit would be unstable.

- $|\lambda_j| < 1$: The given perturbation decays in the corresponding eigenvector direction, so the periodic orbit would be stable.

- $|\lambda_j| = 1$: The given perturbation does not grow or decay, so the periodic orbit would be neutrally stable.

4.3.1 Monodromy Matrix

In CRTBP, $P(\vec{x}^*)$ is the propagation of the initial state, $\vec{x}^*$, by using the equations of motion of CRTBP during one period. Therefore, $[DP(\vec{x}^*)]$ is in fact the STM, $\Phi(T, \tau_0)$, from τ_0 to period T. The matrix $\Phi(T, \tau_0)$ is also called as the Monodromy matrix. So, eigenvalues of the Monodromy matrix are crucial to understand the stability of the Lyapunov orbits.

To identify the eigenvalues, first it is shown that Monodromy matrix is a symplectic matrix. Let $U(\tau)$ is;

$$U(\tau) = \Phi(\tau, \tau_0)^T K^{-1} \Phi(\tau, \tau_0), \tag{4.22}$$

where K is a nonsingular, skew-symmetric matrix [39];

$$K = \begin{bmatrix} 0 & 0 & 0 & 1 & 0 & 0 \\ 0 & 0 & 0 & 0 & 1 & 0 \\ 0 & 0 & 0 & 0 & 0 & 1 \\ -1 & 0 & 0 & 0 & 2 & 0 \\ 0 & -1 & 0 & -2 & 0 & 0 \\ 0 & 0 & -1 & 0 & 0 & 0 \end{bmatrix}. \tag{4.23}$$

Next, take the time derivate of $U(\tau)$;

$$\dot{U}(\tau) = \dot{\Phi}(\tau, \tau_0)^T K^{-1} \Phi(\tau, \tau_0) + \Phi(\tau, \tau_0)^T K^{-1} \dot{\Phi}(\tau, \tau_0). \tag{4.24}$$

Recall $\dot{\Phi}(\tau, \tau_0) = A(\tau)\Phi(\tau, \tau_0)$ from Eqn. (4.5b), and put it into Eqn. (4.24);

$$\dot{U}(\tau) = \Phi(\tau, \tau_0)^T A(\tau)^T K^{-1} \Phi(\tau, \tau_0) + \Phi(\tau, \tau_0)^T K^{-1} A(\tau) \Phi(\tau, \tau_0). \tag{4.25}$$

By rearranging Eqn. (4.25), one can get;

$$\dot{U}(\tau) = \Phi(\tau, \tau_0)^T \left[A(\tau)^T K^{-1} + K^{-1} A(\tau) \right] \Phi(\tau, \tau_0). \tag{4.26}$$

Since $A(\tau)^T K^{-1} + K^{-1} A(\tau) = 0$, then $\dot{U}(\tau) = 0$. Also notice that $U(\tau_0)$ is;

$$U(\tau_0) = \Phi(\tau_0, \tau_0)^T K^{-1} \Phi(\tau_0, \tau_0) = K^{-1}, \tag{4.27}$$

where $\Phi(\tau_0, \tau_0)$ is the identity matrix. So, $U(\tau) = K^{-1}$. Then the STM, $\Phi(\tau, \tau_0)$, satisfies the symplectic condition;

$$\Phi(\tau, \tau_0)^T K^{-1} \Phi(\tau, \tau_0) = K^{-1}. \tag{4.28}$$

Therefore, the Monodromy matrix, $M = \Phi(T, \tau_0)$, is a symplectic matrix. In order to find eigenvalues, characteristic polynomial of M is written as;

$$p(\lambda) = \det(M - \lambda I_n). \tag{4.29}$$

It is possible to write $M = K \left(M^T\right)^{-1} K^{-1}$ by using the symplectic property of M, so;

$$p(\lambda) = \det \left(K \left(M^T\right)^{-1} K^{-1} - \lambda I_n \right). \tag{4.30}$$

Inside the determinant can be rearranged as follows;

$$p(\lambda) = \det \left(K \left(\left(M^T\right)^{-1} - \lambda I_n \right) K^{-1} \right). \tag{4.31}$$

Since $\det(K) = \det(K^{-1}) = 1$ and $\left(M^T\right)^{-1} = (M^{-1})^T$, then;

$$p(\lambda) = \det \left(\left(M^{-1} - \lambda I_n\right)^T \right) = \det \left(M^{-1} - \lambda I_n\right). \tag{4.32}$$

It can be rearranged as;

$$p(\lambda) = \det \left(M^{-1} (I_n - \lambda M)\right) = \det \left(M^{-1}\right) \det (I_n - \lambda M). \tag{4.33}$$

Since M is a symplectic matrix, $\det(M^{-1}) = (\det(M))^{-1} = 1$, then;

$$p(\lambda) = \det (I_n - \lambda M) = \det \left(-\lambda \left(M - \frac{1}{\lambda} I_n \right) \right). \tag{4.34}$$

Finally, one finds;

$$p(\lambda) = (-\lambda)^n \, p\left(\frac{1}{\lambda}\right). \tag{4.35}$$

Since $\lambda \neq 0$, the characteristic polynomial should satisfy;

$$p(\lambda) = 0, \quad p\left(\frac{1}{\lambda}\right) = 0, \tag{4.36}$$

which means if λ is an eigenvalue of M, so is $\frac{1}{\lambda}$. Hence, eigenvalues of the Monodromy matrix arise as reciprocal pairs.

In addition, perturbation along the periodic orbit does not grow or decay. So, according to the Eqn. (4.21), there should be an eigenvalue which is equal to one for the periodic orbits and the corresponding eigenvector is tangent to the orbit. As a result, possible eigenvalues of the Monodromy matrix belonging to the planar Lyapunov orbits can be given as follows;

$$\lambda_1, \quad \lambda_2 = \frac{1}{\lambda_1}, \quad \lambda_3 = \lambda_4 = 1. \tag{4.37}$$

So, there are stable, unstable and neutrally stable modes.

4.4 Stable and Unstable Invariant Manifolds

According to the eigenvalues of the Monodromy matrix, there are stable and unstable invariant manifolds associated to the Lyapunov orbit. The definitions given in [40] are used for introducing the manifolds;

- Stable Manifold (W^S): It is the set of initial conditions such that the trajectory of a particle starting at those initial conditions approaches to the periodic orbit as $\tau \to \infty$. The proper set can be obtained from the eigenvector corresponding to $|\lambda| < 1$.
- Unstable Manifold (W^U): It is the set of initial conditions such that the trajectory of a particle starting at those initial conditions moves away from the periodic orbit as $\tau \to \infty$. The proper set can be obtained from the eigenvector corresponding to $|\lambda| > 1$.

The initial guesses to generate stable and unstable manifolds can be given respectively as follows;

$$\vec{y}_S(\vec{y}_0) = \vec{y}_0 \pm \epsilon \vec{u}_S(\vec{y}_0), \tag{4.38a}$$

$$\vec{y}_U(\vec{y}_0) = \vec{y}_0 \pm \epsilon \vec{u}_U(\vec{y}_0), \tag{4.38b}$$

where $\vec{u}_S$, $\vec{u}_U$ are the normalized stable and unstable eigenvectors, $\vec{y}_0$ is an initial state on the periodic orbit and ϵ is a small perturbation applied to that initial state. It is mentioned in [33] and [37] that the order of perturbation should be small enough to make the linear approximation valid, and also it should not be too small to require a large amount of time to depart from the periodic orbit. The positive and negative perturbations refer to the construction of manifolds in different realms.

The stable and unstable manifolds are generated by backward and forward propagation of the initial states $\vec{y}_S(\vec{y}_0)$ and $\vec{y}_U(\vec{y}_0)$, respectively. Examples of the stable and unstable manifolds associated to the L_1 Lyapunov orbit of the Earth-Moon system with Jacobi constant of $C = -1.58$ are given in Fig. 4.7.

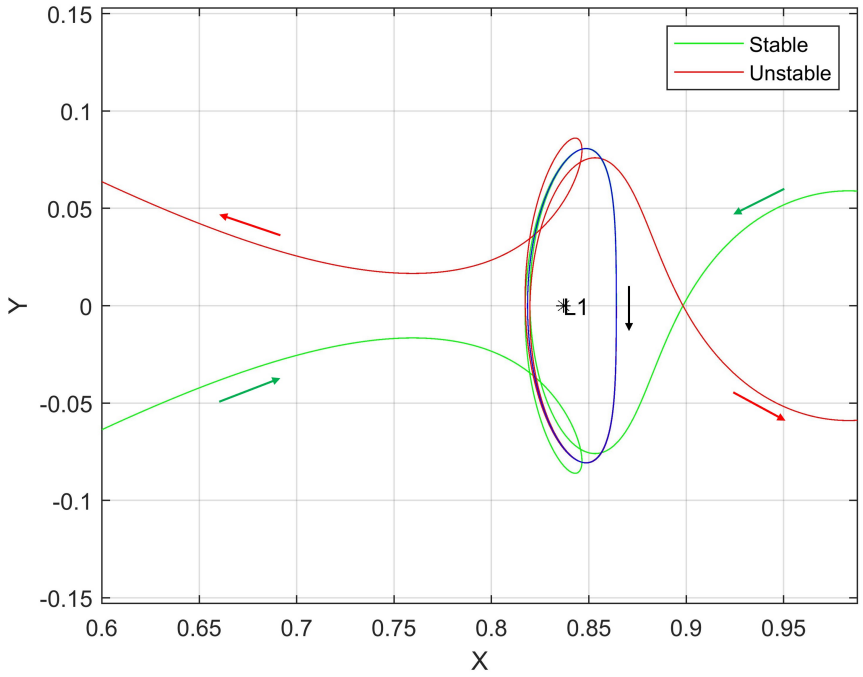

Figure 4.7: Stable and unstable manifolds associated to L_1 Lyapunov orbit of the Earth-Moon system with Jacobi constant of $C = -1.58$.

It is possible to generate sets of manifolds by using various points along the periodic orbit. This can be done by calculating the eigenvalues and corresponding eigenvectors of the monodromy matrix at each of those points. However, this method is computationally inefficient. There is an alternative way which includes the propagation of

eigenvectors by using STM;

$$\vec{u}_S(\vec{y}_i) = \Phi(\tau_i, \tau_0)\vec{u}_S(\vec{y}_0), \tag{4.39a}$$

$$\vec{u}_U(\vec{y}_i) = \Phi(\tau_i, \tau_0)\vec{u}_U(\vec{y}_0). \tag{4.39b}$$

Since the STM does not conserve the norm of a vector, the eigenvectors should be normalized in order to apply perturbations appropriately. Then, the initial guesses of the stable and unstable manifolds belonging to the various points along the periodic orbit can be given as;

$$\vec{y}_S(\vec{y}_i) = \vec{y}_i \pm \epsilon \frac{\vec{u}_S(\vec{y}_i)}{\left|\vec{u}_S(\vec{y}_i)\right|}, \tag{4.40a}$$

$$\vec{y}_U(\vec{y}_i) = \vec{y}_i \pm \epsilon \frac{\vec{u}_U(\vec{y}_i)}{\left|\vec{u}_U(\vec{y}_i)\right|}. \tag{4.40b}$$

The resulting manifold sets form a tube-like structure as given in Fig. 4.8. The trajectories inside and outside the tubes yield transit and non-transit orbits, respectively. So, the invariant manifolds act as separatrices such that they separate the regions of two types of motion.

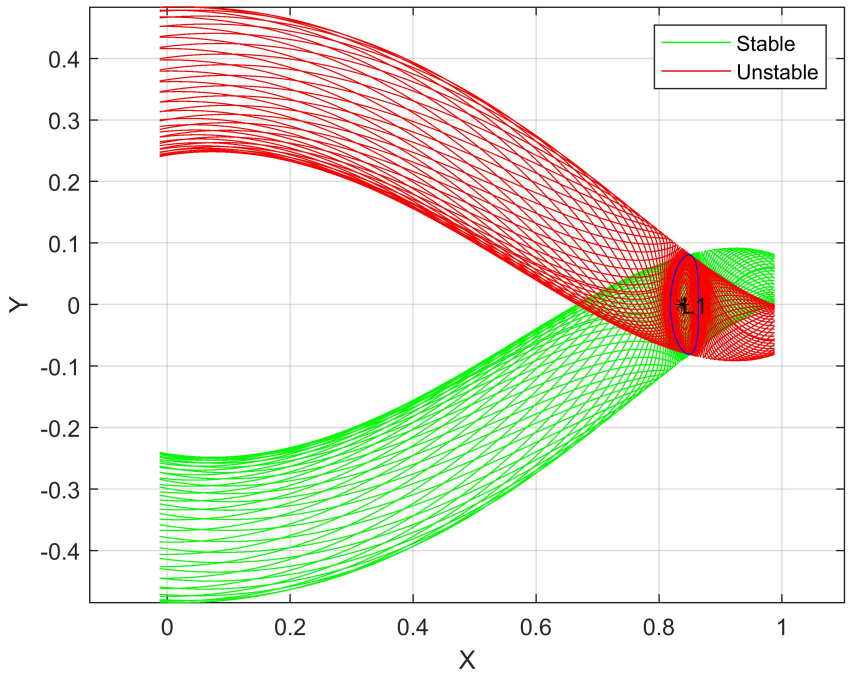

Figure 4.8: Stable and unstable invariant manifold tubes associated to L_1 Lyapunov orbit of the Earth-Moon system with Jacobi constant of $C = -1.58$.

4.5 Homoclinic Orbits

A homoclinic orbit connects the Lyapunov orbit with itself. In other words, it is an orbit that departs from and returns back to the same Lyapunov orbit via its unstable and stable manifolds. The intersection of manifolds on an appropriate Poincaré surface is the key point for the construction of homoclinic orbits. For the sake of simplicity of the calculation, Poincaré surface is chosen as the plane of X-$\dot{X}$ at $Y = 0$ and represented with $\Gamma|_{Y=0}$. First, the homoclinic orbits in the interior realm are investigated. The interior realm is the region of trajectories which cannot pass beyond L_1. In order to obtain the intersection of unstable and stable manifolds on the Poincaré surface, energy of the Lyapunov orbit is increased. The unstable and stable manifolds associated to L_1 Lyapunov orbit of Earth-Moon system with $C = -1.57$ and the corresponding Poincaré surfaces, $\Gamma_{L_1}^{U,interior}|_{Y=0}$ and $\Gamma_{L_1}^{S,interior}|_{Y=0}$, are given in Fig. 4.9 and Fig. 4.10.

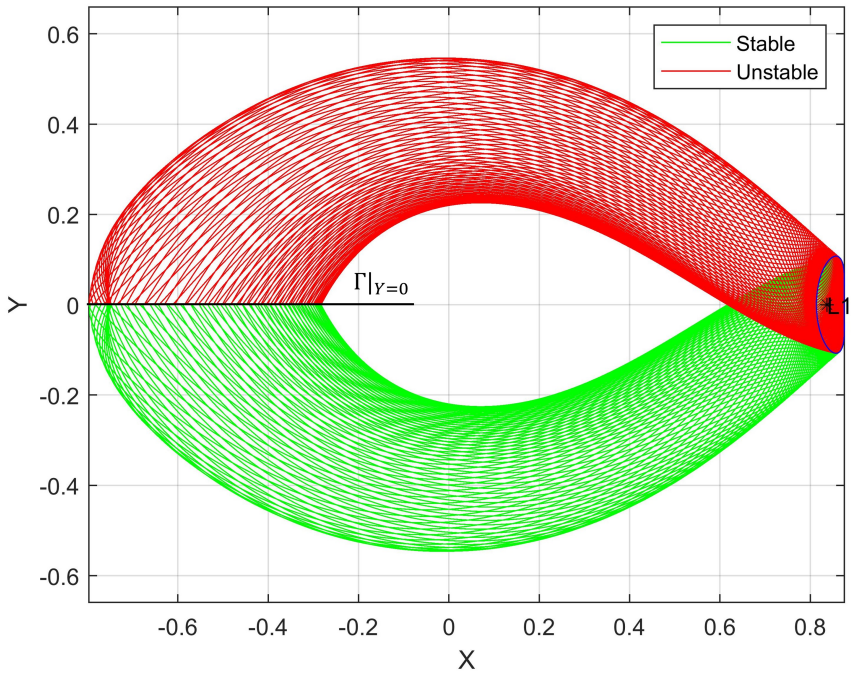

Figure 4.9: Stable and unstable manifolds associated to L_1 Lyapunov orbit in the interior realm of the Earth-Moon system with $C = -1.57$.

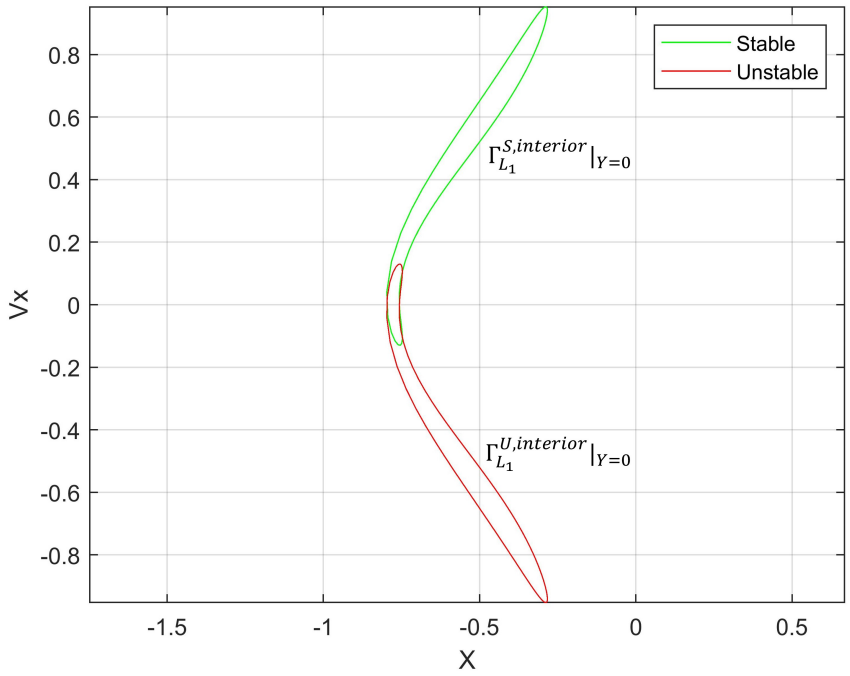

Figure 4.10: Poincaré surfaces of the stable and unstable manifolds given in Fig. 4.9.

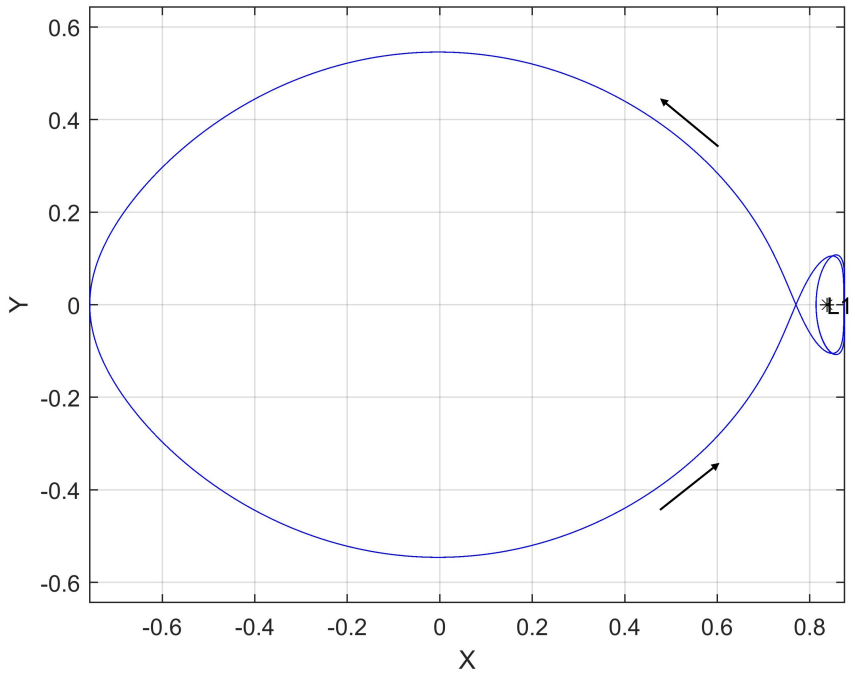

Figure 4.11: Homoclinic orbit in the interior realm of the Earth-Moon system.

$\Gamma_{L_1}^{U,interior}|_{Y=0}$ and $\Gamma_{L_1}^{S,interior}|_{Y=0}$ intersect at four points and two of them are on the line of $\dot{X} = 0$. The intersections with $\dot{X} = 0$ give the transversal homoclinic orbits which are discussed detailed in [41]. The initial conditions for the homoclinic orbits are obtained by using the intersections on Poincaré surface and the equation of the Jacobi constant. An example of the transverse homoclinic orbit in the interior realm is given in Fig. 4.11 for one of the intersections.

Next, we look for the homoclinic orbits in the exterior realm which is beyond L_2. The methodology is same as with the interior. The unstable and stable manifolds associated to the L_2 Lyapunov orbit of Earth-Moon system with $C = -1.55$ and the corresponding Poincaré surfaces, $\Gamma_{L_2}^{U,exterior}|_{Y=0}$ and $\Gamma_{L_2}^{S,exterior}|_{Y=0}$, are given in Fig. 4.12 and Fig. 4.13.

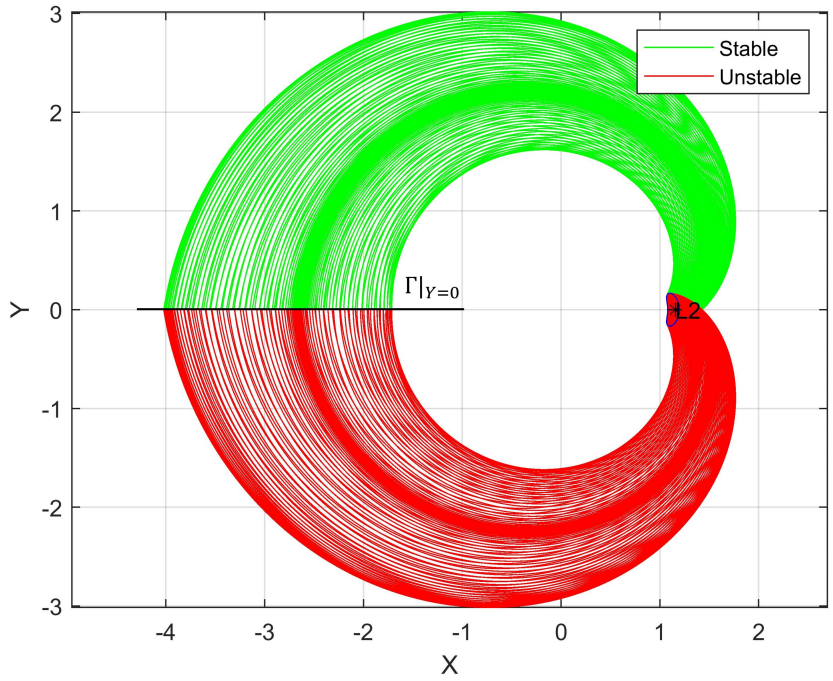

Figure 4.12: Stable and unstable manifolds associated to L_2 Lyapunov orbit in the exterior realm of the Earth-Moon system with $C = -1.55$.

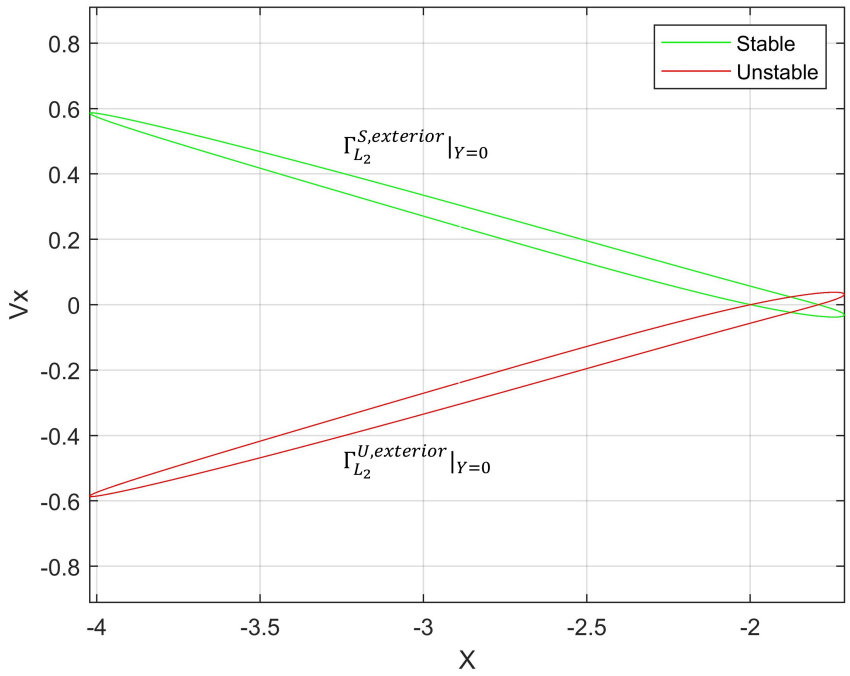

Figure 4.13: Poincaré surfaces of the stable and unstable manifolds given in Fig. 4.12.

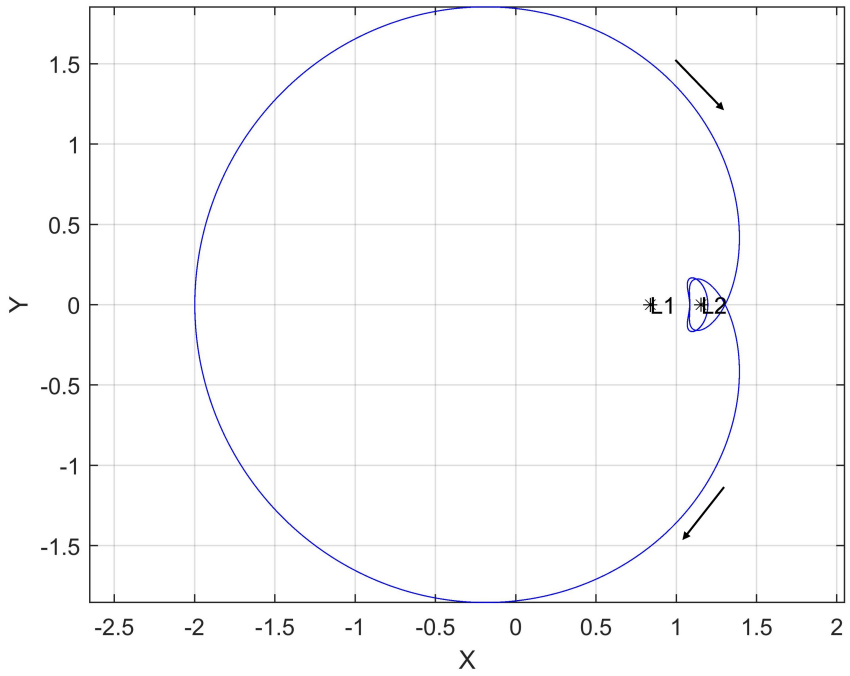

Figure 4.14: Homoclinic orbit in the exterior realm of the Earth-Moon system.

$\Gamma_{L_2}^{U,exterior}|_{Y=0}$ and $\Gamma_{L_2}^{S,exterior}|_{Y=0}$ intersect at four points and two of them are on the line of $\dot{X} = 0$. So, there are transverse homoclinic orbits in the exterior realm. The initial conditions can be found with the same manner as for the interior realm. An example of the transverse homoclinic orbit in the exterior realm is given in Fig. 4.14 for one of the intersections.

4.6 Heteroclinic Orbits

A heteroclinic orbit connects the Lyapunov orbit of different equilibrium points with each other. So, it is an orbit that departs from, say L_1 Lyapunov orbit, via its unstable manifold and arrives to, say L_2 Lyapunov orbit, via its stable manifold. Here again, the intersection of the manifolds on an appropriate Poincaré surface is the key point for the construction of heteroclinic orbits. The Poincaré surface is chosen as the plane of Y-$\dot{Y}$ at $X = 1 - \mu$ and represented with $\Gamma|_{X=1-\mu}$. In order to find the heteroclinic orbits from L_1 to L_2, the unstable manifolds of L_1 Lyapunov orbit and the stable manifold of L_2 Lyapunov orbit are calculated for the Earth-Moon system with $C = -1.57$ in Fig. 4.15 and the corresponding Poincaré surfaces, $\Gamma_{L1}^{U}|_{X=1-\mu}$ and $\Gamma_{L2}^{S}|_{X=1-\mu}$, are given in Fig. 4.16.

Note that the two Lyapunov orbits have the same Jacobi constant. $\Gamma_{L1}^{U}|_{X=1-\mu}$ and $\Gamma_{L2}^{S}|_{X=1-\mu}$ intersect at two points. Then, the initial conditions for the heteroclinic orbits can be found from the intersections of Poincaré surfaces and the equation of Jacobi constant. An example of the heteroclinic orbit goes from L_1 to L_2 is given in Fig. 4.17 for one of the intersections. Since there is a symmetry given with [33];

$$s : (X, Y, \dot{X}, \dot{Y}, \tau) \rightarrow (X, -Y, -\dot{X}, \dot{Y}, -\tau). \tag{4.41}$$

The reverse of the trajectory, namely the heteroclinic orbit goes from L_2 to L_1, can be obtained by using the stated symmetry on initial conditions. The resulting trajectory is given in Fig. 4.18.

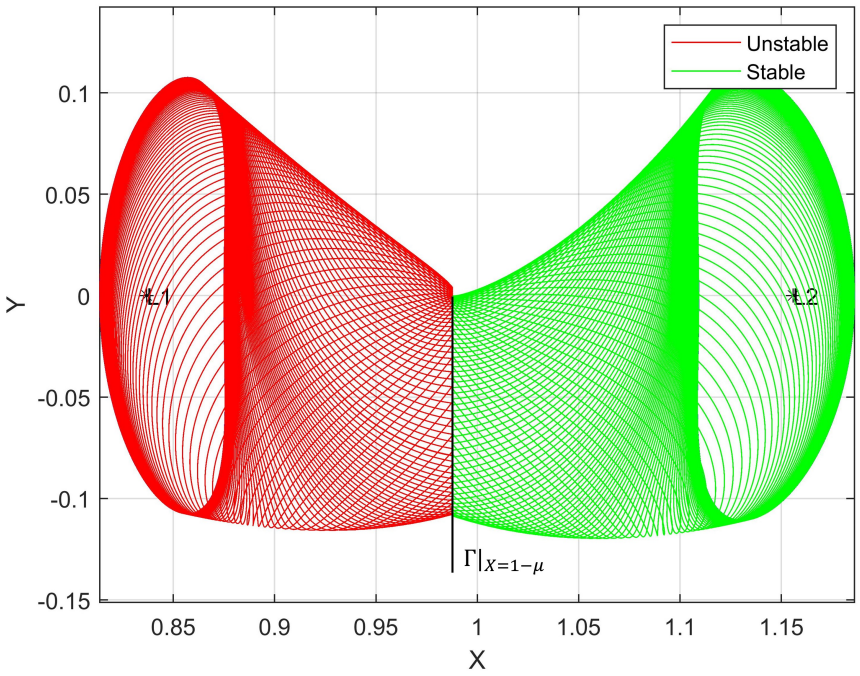

Figure 4.15: Unstable and stable manifolds associated to L_1 and L_2 Lyapunov orbit of the Earth-Moon system with $C = -1.57$.

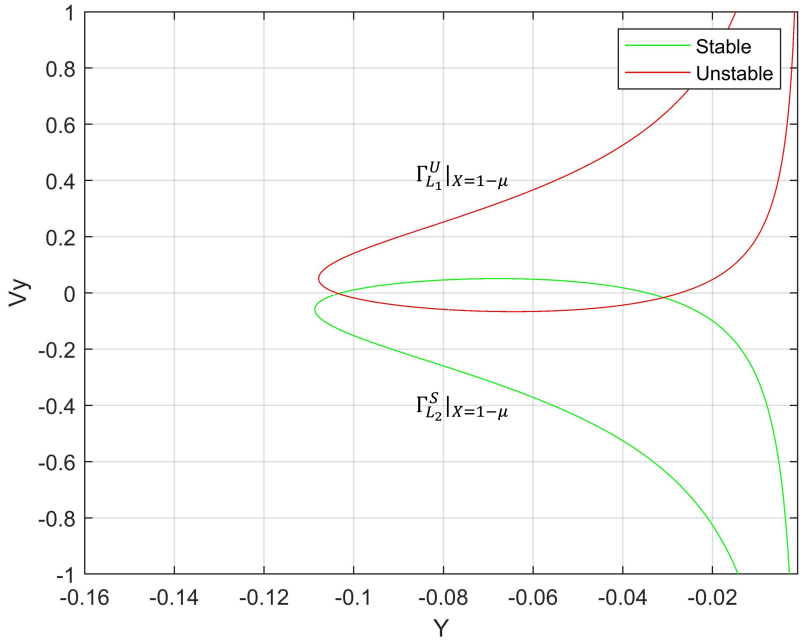

Figure 4.16: Poincaré surfaces of the unstable and stable manifolds given in Fig. 4.15.

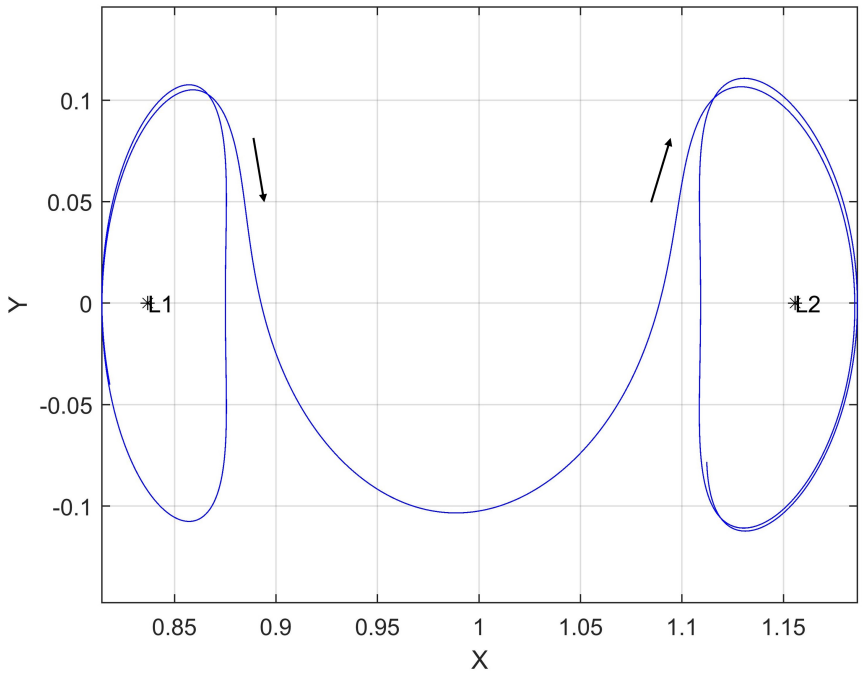

Figure 4.17: Heteroclinic orbit goes from L_1 to L_2 for the Earth-Moon system.

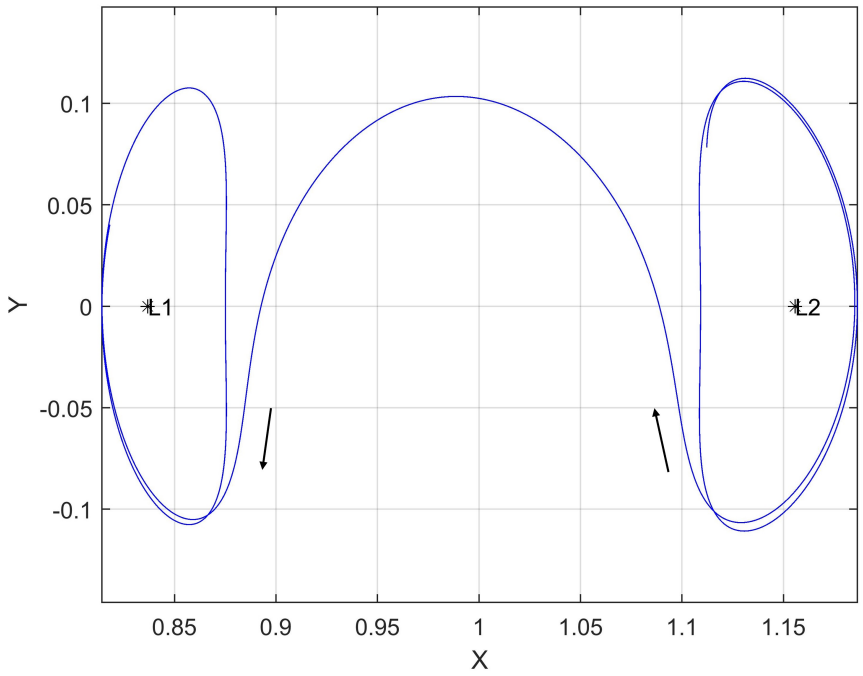

Figure 4.18: Heteroclinic orbit goes from L_2 to L_1 for the Earth-Moon system.

4.7 Chaos in the CRTBP

Lastly, the chaotic nature in the CRTBP is investigated by using the sensitive dependence on initial conditions. There is not a generally accepted definition of chaos, so here the definition given in Strogatz is used [38];

"Chaos is aperiodic long-term behavior in a deterministic system that exhibits sensitive dependence on initial conditions."

The deterministic system refers to that same initial conditions generate the same trajectory, and hence the system does not have any random disturbance. The irregular behaviour arises due to the nonlinear dynamics in the system. The crucial point in the definition is the sensitive dependence on initial conditions. It means small differences in the initial conditions yield the trajectories that diverge exponentialy fast. To analyze the sensitive dependence on initial conditions, the Lyapunov exponent is generally used.

4.7.1 Lyapunov Exponent

In this section, the lecture given in [42] is greatly benefited. Recall the Eqn. (4.4) by excluding the τ_{pert};

$$\vec{y}_{pert}(\tau) = \Phi(\tau, \tau_0)\vec{y}_{pert}(\tau_0), \tag{4.42}$$

which tells how the small variation on the initial condition evolves over time. It is possible to write Eqn. (4.42) as follows;

$$|\vec{y}_{pert}(\tau)|^2 = \left[\Phi(\tau, \tau_0)\vec{y}_{pert}(\tau_0)\right]^T \left[\Phi(\tau, \tau_0)\vec{y}_{pert}(\tau_0)\right]. \tag{4.43}$$

By rearranging the Eqn. (4.43), one can obtain;

$$|\vec{y}_{pert}(\tau)|^2 = \left(\Phi(\tau, \tau_0)^T\Phi(\tau, \tau_0)\right)|\vec{y}_{pert}(\tau_0)|^2. \tag{4.44}$$

The term $\Phi(\tau, \tau_0)^T\Phi(\tau, \tau_0)$ is called as Cauchy-Green deformation tensor (Δ). The largest eigenvalue of Δ gives the maximum stretching occurs at τ. Then,

$$\max|\vec{y}_{pert}(\tau)|^2 = \lambda_{max}(\Delta)|\vec{y}_{pert}(\tau_0)|^2, \tag{4.45}$$

where $\lambda_{max}(\Delta)$ represents the largest eigenvalue of Δ. Next, take the square root of Eqn. (4.45);

$$\max|\vec{y}_{pert}(\tau)| = \sqrt{\lambda_{max}(\Delta)}|\vec{y}_{pert}(\tau_0)|. \tag{4.46}$$

Assume that;

$$\max|\vec{y}_{pert}(\tau)| = e^{\sigma|\tau|}|\vec{y}_{pert}(\tau_0)|. \tag{4.47}$$

Then;

$$e^{\sigma|\tau|} = \sqrt{\lambda_{max}(\Delta)}. \tag{4.48}$$

Finally, the formal definition of Lyapunov exponent is given by rearranging the Eqn. (4.48) and taking the limit as;

$$\lim_{\tau\to\infty}\sigma = \frac{1}{|\tau|}\ln\left(\sqrt{\lambda_{max}(\Delta)}\right). \tag{4.49}$$

If σ is calculated within a finite time interval, then it is called as Finite Time Lyapunov Exponent (FTLE). In CRTBP, it is not possible to integrate the equations of motion to infinity. Therefore, FTLE is used to analyze sensitive depence on initial condition. If $\sigma > 0$, the initial variation grows exponentially and indicates the existence of chaos.

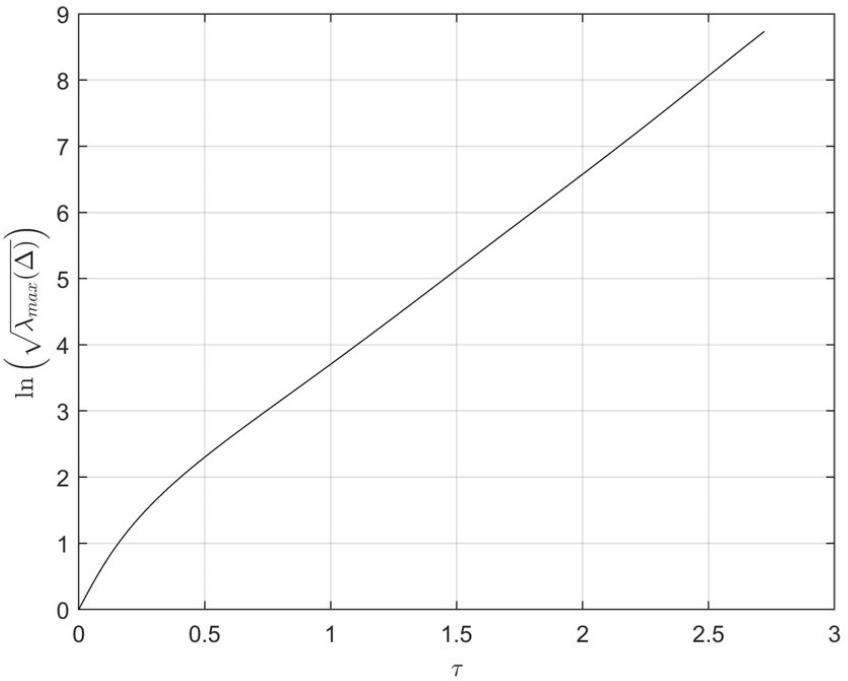

Figure 4.19: $\ln\left(\sqrt{\lambda_{max}(\Delta)}\right)$ versus integration time of the L_1 Lyapunov orbit in the Earth-Moon system with $C = -1.59$.

We investigated the sensitive dependence on the initial condition of the L_1 Lyapunov orbit with $C = -1.59$. The $\ln\left(\sqrt{\lambda_{max}(\Delta)}\right)$ versus integration time is given in Fig. 4.19 and analysis interval is one period. Slope of the plot at an arbitrary τ gives the corresponding FTLE. Since the slope is positive at any τ, a small variation on the initial condition grows exponentially. So, there is sensitive dependence on initial condition which indicates chaos.

CHAPTER 5

APPLICATIONS

5.1 Earth to Moon Low-Energy Transfer

5.1.1 Introduction

The most conventional method to design the orbit of a spacecraft that attains the Moon is patched conic approximation. In this method, motion of the spacecraft is investigated with Earth-spacecraft and Moon-spacecraft two-body problems, therefore the possible orbits are conic sections. The trajectory design is considered within the Earth-spacecraft two-body problem until the spacecraft enters the Moon's Sphere of Influence (SOI). The Moon's SOI is a region where the gravitational attraction of Moon becomes more dominant compared to Earth. Once the spacecraft enters the Moon's SOI, motion is investigated within the Moon-spacecraft two-body problem. Illustration of the patch conic approximation is given in Fig. 5.1.

Spacecraft gets into the geocentric departure trajectory by applying a maneuver near the Earth. The trajectory is studied with the Earth-spacecraft two-body problem until the patch point where the spacecraft intercepts the Moon's SOI. After the patch point, spacecraft follows a hyperbolic trajectory with respect to the Moon and applies a braking maneuver at the periapsis of hyperbola to get into a closed orbit around the Moon. The overall transfer duration is approximately 5 days. However, this method has some drawbacks. Firstly, the spacecraft approaches to the Moon with high relative velocity so the required maneuver to get captured by the Moon is large. Large maneuver means more propellant and more propellant means cost. Secondly, this method constitutes a risk such that if the spacecraft misses the maneuver due to the thruster

engine fail or another problem, it will not be captured by the Moon and therefore will exit the SOI.

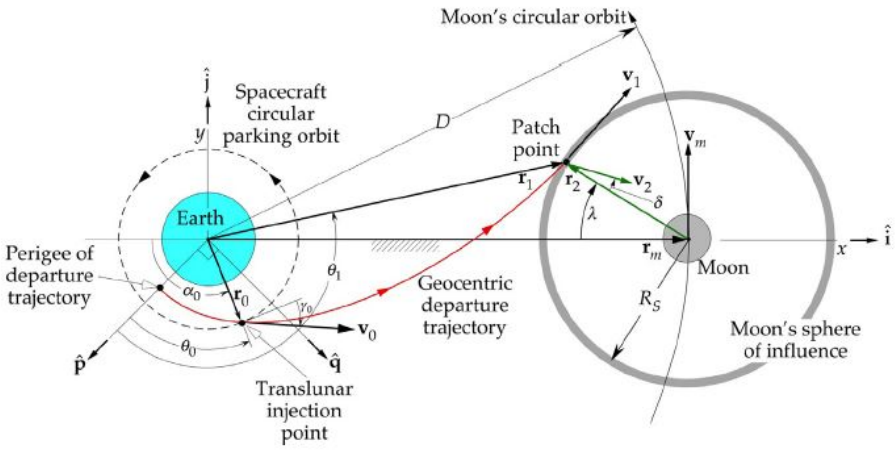

Figure 5.1: Patched conic approximation for the Earth to Moon transfer trajectory [34].

In order to eliminate the drawbacks of the patched conic approximation, Belbruno [43] discovered a new way for the Lunar transfer and later it was called as Weak Stability Boundary (WSB) transfer [31, 44]. He introduced the concept of ballistic capture which refers that spacecraft is captured by the Moon without any maneuver. However, the captured orbit is unstable, therefore a maneuver is required to obtain a stable orbit around the Moon. But still the amount of maneuver is smaller than the patched conic approximation. In other words, less energy is required to attain the Lunar orbit compared to traditional method. For this reason, WSB method is also called as low-energy transfer. The drawback of this method is the long transfer duration, about order of months. The low-energy transfer becomes possible by taking the advantage of the gravity of Sun. So, the trajectory is designed by considering the Earth-Moon-Sun-spacecraft four body interactions. After the Belbruno's work, Koon et al. [32] investigated the WSB method with the approach of coupled three-body model by using the Lagrange point dynamics of Sun-Earth-spacecraft and Earth-Moon-spacecraft systems. They provided a more systematic way for the construction of low-energy transfer.

In 1990, WSB method was demonstrated for the first time in Japanese Lunar mission,

Hiten spacecraft. Since then, it has been used in space missions such as GRAIL mission of National Aeronautics and Space Administration and more recently KPLO mission of Korean Aerospace Research Institute.

5.1.1.1 Reference Frames and Transformations

Since the trajectory is initially designed with the patched three-body approximation, it is useful to introduce Sun and Earth-Moon barycenter (Sun-EM) rotating frame and Earth-Moon rotating frame. In Fig. 5.2, $\bar{X} - \bar{Y}$ is the Sun-EM rotating frame, $X' - Y'$ is the Earth-Moon rotating frame, $X - Y$ is an arbitrary inertial frame, θ_M is the angular displacement of Moon relative to $\bar{X}$ axis, and lastly CM represents the center of mass of the relevant frame.

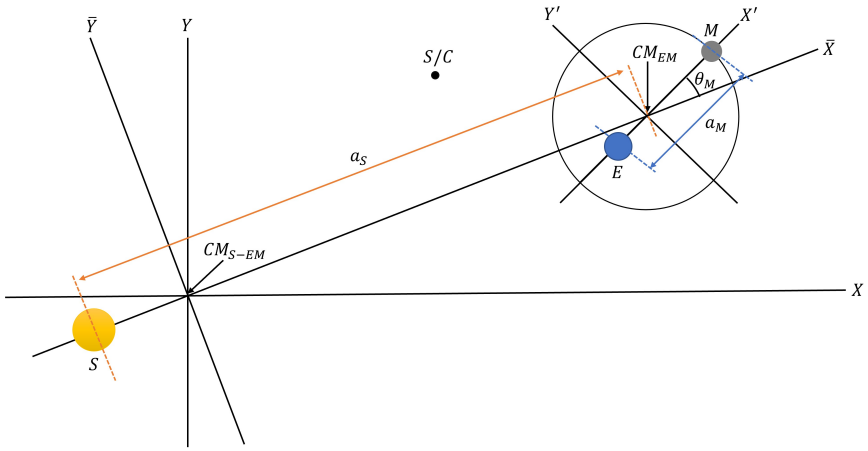

Figure 5.2: Illustration of the coordinate frames.

The arrival trajectory to the Moon is initially constructed with use of the Earth-Moon rotating frame and the departure trajectory from Earth is initially constructed with use of Sun-EM rotating frame. Therefore, the frame transformations are necessary to design overall transfer.

Earth-Moon Rotating Frame to Sun-EM Rotating Frame: In order to transform the position vector of spacecraft from Earth-Moon rotating frame to Sun-EM rotating frame, following transformation is applied;

$$\vec{r}_{S/C} = \vec{r}_{EM} + C\left[\theta_M(\tau')\right]\vec{r'}_{S/C}\frac{a_M}{a_S}. \tag{5.1}$$

Here, $\vec{\bar{r}}_{S/C}$ and $\vec{\bar{r}}_{EM}$ are the position vectors of spacecraft and Earth-Moon barycenter relative to Sun-EM rotating frame respectively, $\vec{r'}_{S/C}$ is the position vector of spacecraft relative to Earth-Moon rotating frame, the coefficient $\frac{a_M}{a_S}$ stands for the transformation of nondimensional distance between the two frames and lastly $C\left[\theta_M(\tau')\right]$ is the rotation matrix of;

$$C\left[\theta_M(\tau')\right] = \begin{bmatrix} \cos\theta_M(\tau') & -\sin\theta_M(\tau') \\ \sin\theta_M(\tau') & \cos\theta_M(\tau') \end{bmatrix}, \tag{5.2}$$

where $\theta_M(\tau')$ is written as;

$$\theta_M(\tau') = \theta_{M,0} + \left(1 - \frac{\Omega_S}{\Omega_M}\right)\tau'. \tag{5.3}$$

Here $\theta_{M,0}$ is the initial phase angle of the Moon, Ω_S and Ω_M are the angular velocities of the Sun-EM and Earth-Moon rotating frames, respectively, lastly τ' is the nondimensional time of Earth-Moon rotating frame.

Then, to transform the velocity vector of spacecraft from the Earth-Moon rotating frame to the Sun-EM rotating frame, Eqn. (5.1) is differentiated with respect to τ' as follows;

$$\vec{\bar{v}}_{S/C} = \frac{a_M}{a_S}\frac{\Omega_M}{\Omega_S}\left(\dot{C}\left[\theta_M(\tau')\right]\vec{r'}_{S/C} + C\left[\theta_M(\tau')\right]\vec{v'}_{S/C}\right), \tag{5.4}$$

and $\dot{C}\left[\theta_M(\tau')\right]$ is;

$$\dot{C}\left[\theta_M(\tau')\right] = \begin{bmatrix} -\sin\theta_M(\tau') & -\cos\theta_M(\tau') \\ \cos\theta_M(\tau') & -\sin\theta_M(\tau') \end{bmatrix}\left(1 - \frac{\Omega_S}{\Omega_M}\right). \tag{5.5}$$

In Eqn. (5.4), the coefficient $\frac{\Omega_M}{\Omega_S}$ comes from the transformation of nondimensional time between the two frames which is $\bar{\tau} = \frac{\Omega_S}{\Omega_M}\tau'$.

Sun-EM Rotating Frame to Earth-Moon Rotating Frame: In order to transform the position vector of spacecraft from Sun-EM rotating frame to Earth-Moon rotating frame, following transformation is applied;

$$\vec{r'}_{S/C} = C^T\left[\theta_M(\bar{\tau})\right]\left(\vec{\bar{r}}_{S/C} - \vec{\bar{r}}_{EM}\right)\frac{a_S}{a_M}, \tag{5.6}$$

where $\theta_M(\bar{\tau})$ is written as;

$$\theta_M(\bar{\tau}) = \theta_{M,0} + \left(\frac{\Omega_M}{\Omega_S} - 1\right)\bar{\tau}. \tag{5.7}$$

Then, to transform the velocity vector of spacecraft from Sun-EM rotating frame to Earth-Moon rotating frame, Eqn. (5.6) is differentiated with respect to $\bar{\tau}$ as follows;

$$\vec{v'}_{S/C} = \frac{a_S}{a_M}\frac{\Omega_S}{\Omega_M}\left(\dot{C}^T\left[\theta_M(\bar{\tau})\right]\left(\vec{\bar{r}}_{S/C} - \vec{\bar{r}}_{EM}\right) + C^T\left[\theta_M(\bar{\tau})\right]\vec{\bar{r}}_{S/C}\right). \tag{5.8}$$

5.1.2 Trajectory Design Methodology

There has been numerious studies on the design of low-energy transfer since it was first proposed by Belbruno. In [31], the trajectory is designed with use of WSB where the gravitational influence of the bodies tend to balance and may be considered as the SOI region. In the WSB method, first the initial condition is acquired from the WSB of Earth-Moon system, then it is propagated backwards in the context of four-body problem of Sun-Earth-Moon-spacecraft until the WSB of Sun-Earth system. At this position, a velocity change is applied so that spacecraft reaches the near Earth distance after the backward propagation. The resulting Earth to Moon trajectory yields ballistic capture at the Moon. Later, the low-energy trajectory design is investigated more systematically in [32] by using Lagrange point dynamics of the restricted three-body problem. The capture trajectory to the Moon is analyzed in the Earth-Moon system and the departure trajectory from Earth is analyzed in the Sun-Earth system. So, this method is also called as patched three-body approximation. In this method, the intersections of manifold structures associated to Lagrange point orbits for the Earth-Moon and Sun-Earth systems on a suitable chosen Poincaré section is utilized in the trajectory design. In addition to the WSB and patched three-body methods, the trajectory design is also studied by using Lagrange Coherent Structures [45] and periapse maps [46]. Lastly, most of the low-energy transfer is designed by using L_1 or L_2 of the Sun-Earth system. In [47], the low-energy transfer is constructed by using L_1 of the Earth-Moon system but the transfer duration is longer than the other methods.

In this thesis, the design of low-energy transfers are studied first by using patched three-body approximation to obtain an initial condition. Then, this initial condition is used to construct Earth to Moon trajectory in the Bicircular Restricted Four-Body Problem (BRFBP) by utilizing targeting algorithm.

5.1.2.1 Patched-Three Body Approximation

In the patched three-body approximation, the capture trajectory to the Moon and the departure trajectory from the Earth are investigated in Earth-Moon and Sun-EM systems, respectively. The trajectory design is started with the construction of capture orbit. To design the capture orbit, first L_2 Lyapunov orbit of the Earth-Moon system is generated for a particular Jacobi constant. Since the Jacobi constant corresponding to L_2 is $C_{L2} \approx -1.586$, a slightly larger Jacobi constant $C_{EM} = -1.580$ is chosen so that a neck is opened around L_2 and the spacecraft is able to pass from exterior realm to the interior realm of Moon. Then, the unstable manifolds of L_2 Lyapunov orbit for the Moon realm is generated until the Poincaré section of $\Gamma_{X'=1-\mu_M}$. This Poincaré section is chosen to simplify the calculations. The unstable manifolds and the Poincaré surface are given in Fig. 5.3 and Fig. 5.4, respectively. In the numerical analysis, MATLAB built-in ode45 solver is used with absolute and relative tolerances of 10^{-13}, and the mass parameter for the Earth-Moon system is taken as $\mu_M = 0.01215$.

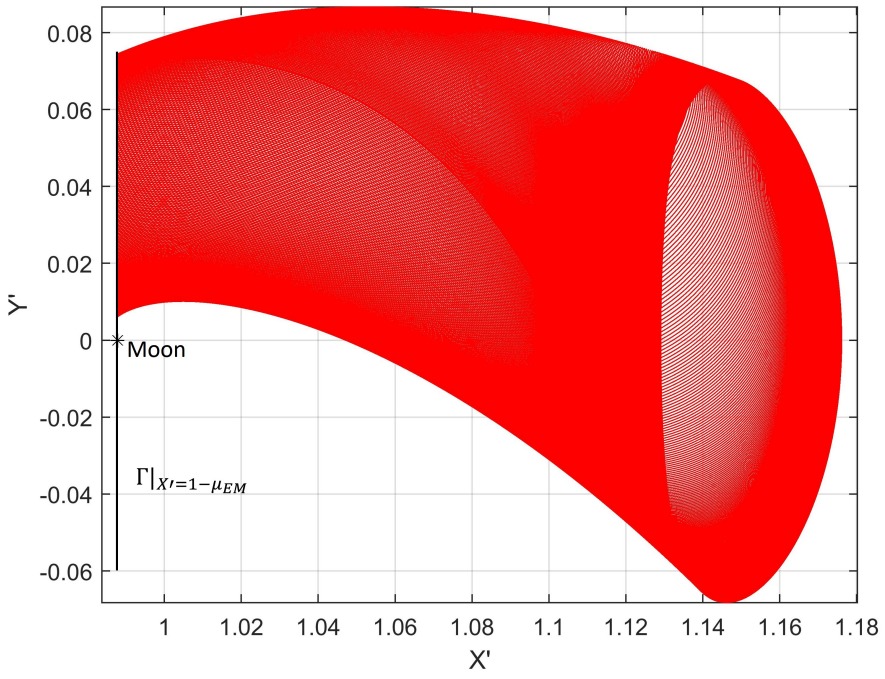

Figure 5.3: Unstable manifolds associated to L_2 Lyapunov orbit of the Earth-Moon system with $C_{EM} = -1.580$.

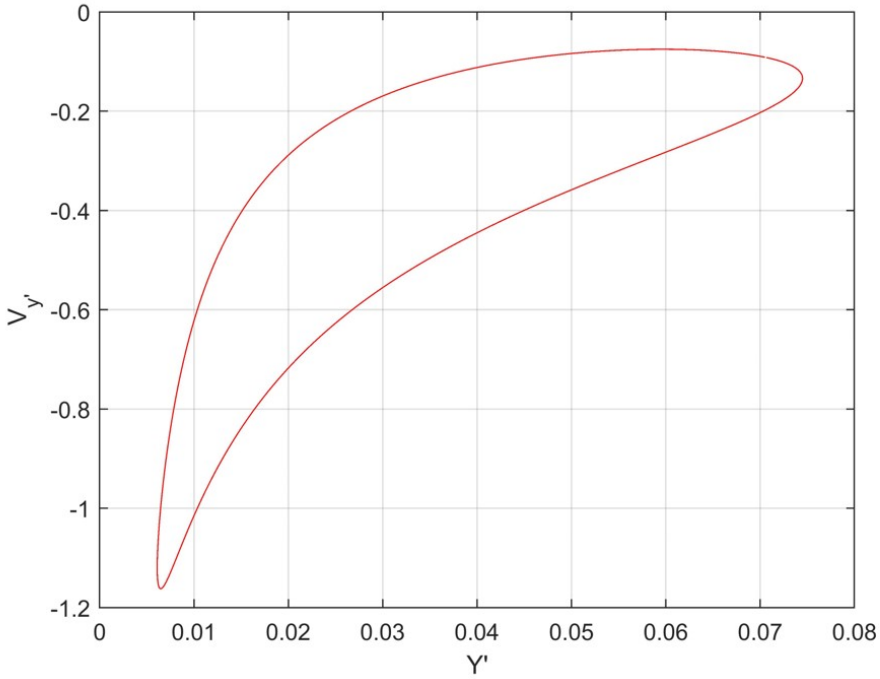

Figure 5.4: Poincaré surface at $X' = 1 - \mu_{EM}$.

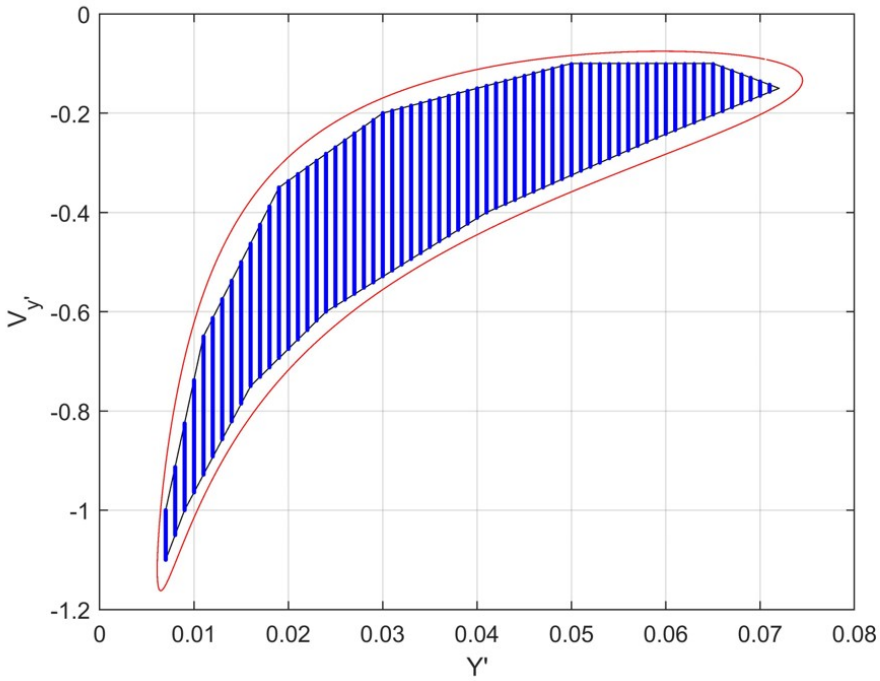

Figure 5.5: Polygon and grids to obtain points inside the curve.

The initial conditions inside the red closed curve in Fig. 5.4 yield the transit orbits through the L_2 neck. So, they provide the transition from the exterior realm to the Moon realm. Although, it is not straightforward to obtain points in the closed curve. To do this, first a polygon is constructed inside the curve, then it is divided into grids as given in Fig. 5.5.

Once the points inside the curve are obtained, they are used to construct low-energy transfers. In calculating the capture trajectories, points are propagated forward in the Earth-Moon system. Since the ballistic capture is desired, trajectories are filtered according to have at least one revolution around the Moon. In addition, the minimum distance to the Moon, the so called perilune, is recorded for the filtered capture trajectories. In calculating the departure trajectories, points are propagated backward in the Earth-Moon system until the Poincaré section of $\Gamma_{\bar{X}=1-\mu_S}$, where $\mu_S = 3.041 \times 10^{-6}$ is the mass parameter of the Sun-EM system. This section is chosen because of the geometrical insight coming from [32]. Then, the trajectories are propagated backward in the Sun-EM system. Here, Earth-Moon to Sun-EM frame transformation is necessary, so the initial Moon phase angle, $\theta_{M,0}$, is required. This angle is chosen as $\theta_{M,0} = 140^\circ$ with trial and error such that the backward propagated trajectories in the Sun-EM frame able to reach near Earth altitudes. In the frame transformation, the relevant parameters are taken as $a_m = 384400$ km, $a_s = 1496 \times 10^5$ km, $\Omega_M = 2.665 \times 10^{-6}$ rad/s and $\Omega_S = 1.991 \times 10^{-7}$ rad/s. Finally, the resulting departure trajectories are filtered such that the minimum distance to the Earth, the so called perigee, would be equal to Low Earth Orbit (LEO) altitudes, lower than the 2000 km altitude. In this manner, first the perigee versus perilune plot is drawn for all the filtered trajectories in Fig. 5.6. Each point on the plot corresponds to a particular trajectory, and they all are drawn in the Sun-EM frame in Fig. 5.7. To look at the capture part in detail, capture trajectories are drawn in the Earth-Moon frame in Fig. 5.8. They approach to the Moon realm via the transit region through the L_2 Lyapunov orbit and have at least one revolution around the Moon. So, the capture is ballistic.

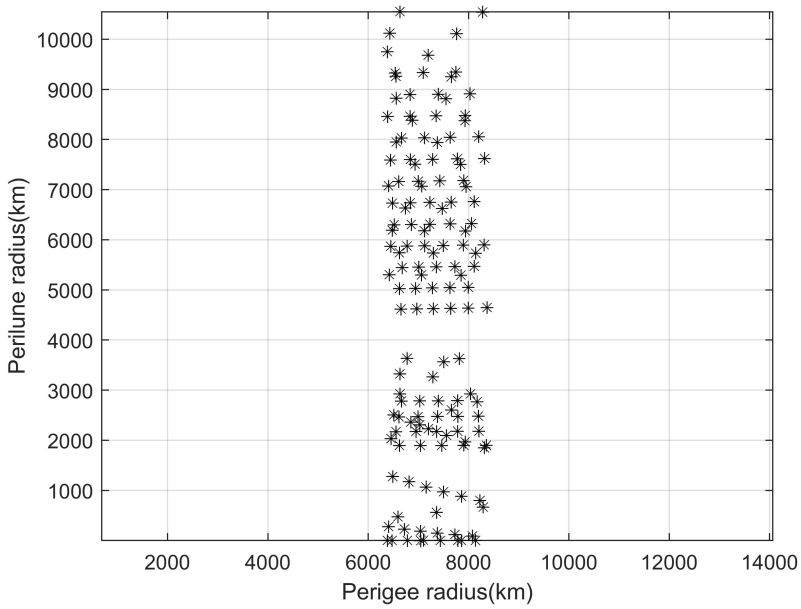

Figure 5.6: The minimum distance to the Earth, perigee, versus the minimum distance to the Moon, perilune, for the filtered trajectories in the patched three-body approximation.

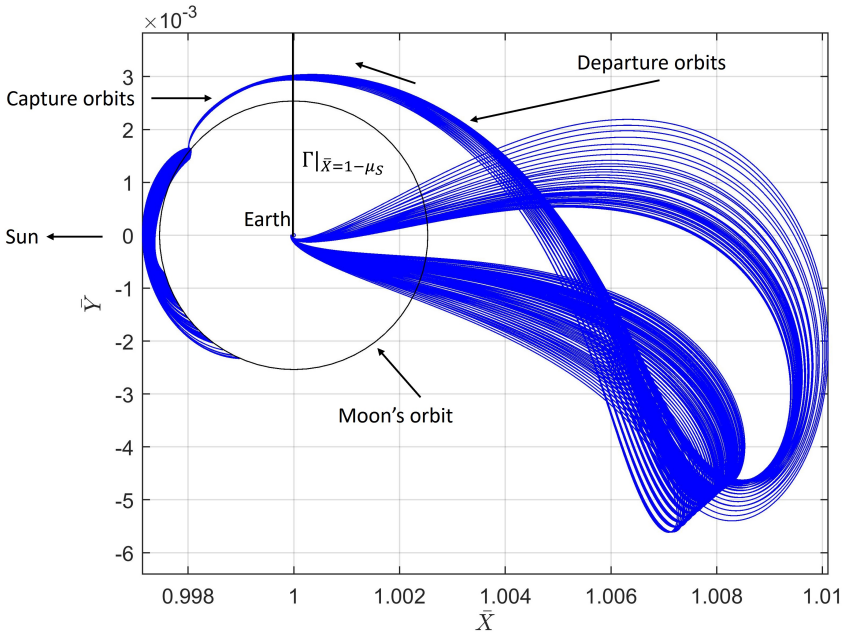

Figure 5.7: Earth to Moon low-energy transfers in Sun-EM frame for the patched three-body approximation.

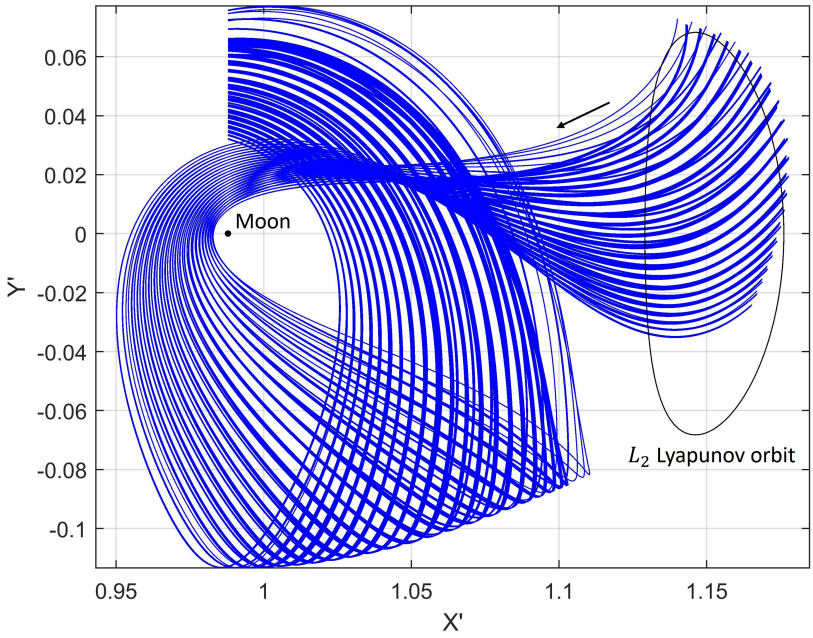

Figure 5.8: Ballistic capture trajectories in the Earth-Moon frame for the patched three-body approximation.

5.1.2.2 Bicircular Restricted Four-Body Problem

In the previous section, trajectories were obtained by using patched three-body approximation. This approach provides an initial guess for the actual four-body problem where the Sun, Earth and Moon are considered simultaneously. In calculating the four-body trajectories, BRFBP is used as the underlying dynamical model, and setting of the BRFBP is given in Fig. 5.2. The model includes some assumptions to simplify the problem. First, it assumes that the orbits of Earth around the Sun and Moon around the Earth are circular. In fact, they move in elliptical orbits but the eccentricity of the ellipse is relatively small, $e = 0.0549$ [48] for the orbit of Moon and $e = 0.0167$ [49] for the orbit of Earth. Second, the BRFBP assumes that Sun, Earth and Moon move in the same plane. But in fact, the orbital planes of Sun-Earth and Earth-Moon systems are different. Earth-Moon orbital plane has inclination of $i = 5.1450^{\circ}$ [48] to the ecliptic plane. But still the assumptions are reasonable and also useful to capture the transfer dynamics in a more simple model. The equations

of motion for the BRFBP is written relative to Sun-EM rotating frame, namely $\bar{X}$-$\bar{Y}$ frame, and given as;

$$\ddot{\bar{X}} - 2\dot{\bar{Y}} - \bar{X} = -\frac{(1-\mu_S)}{|\vec{\bar{r}} - \vec{\bar{r}}_S|^3}\left(\bar{X} - \bar{X}_S\right) - \frac{\mu_S\,(1-\mu_M)}{|\vec{\bar{r}} - \vec{\bar{r}}_E|^3}\left(\bar{X} - \bar{X}_E\right) - \frac{\mu_S\mu_M}{|\vec{\bar{r}} - \vec{\bar{r}}_M|^3}\left(\bar{X} - \bar{X}_M\right), \tag{5.9a}$$

$$\ddot{\bar{Y}} + 2\dot{\bar{X}} - \bar{Y} = -\frac{(1-\mu_S)}{|\vec{\bar{r}} - \vec{\bar{r}}_S|^3}\left(\bar{Y} - \bar{Y}_S\right) - \frac{\mu_S\,(1-\mu_M)}{|\vec{\bar{r}} - \vec{\bar{r}}_E|^3}\left(\bar{Y} - \bar{Y}_E\right) - \frac{\mu_S\mu_M}{|\vec{\bar{r}} - \vec{\bar{r}}_M|^3}\left(\bar{Y} - \bar{Y}_M\right), \tag{5.9b}$$

where $\vec{\bar{r}}_S$, $\vec{\bar{r}}_E$ and $\vec{\bar{r}}_M$ are the position vectors of Sun, Earth and Moon in the Sun-EM frame;

$$\vec{\bar{r}}_S = -\mu_S\hat{\bar{X}}, \tag{5.10a}$$

$$\vec{\bar{r}}_E = \left((1-\mu_S) - \frac{a_M}{a_S}\mu_M\cos\theta_M(\bar{\tau})\right)\hat{\bar{X}} + \left(-\frac{a_M}{a_S}\mu_M\sin\theta_M(\bar{\tau})\right)\hat{\bar{Y}}, \tag{5.10b}$$

$$\vec{\bar{r}}_M = \left((1-\mu_S) + \frac{a_M}{a_S}(1-\mu_M)\cos\theta_M(\bar{\tau})\right)\hat{\bar{X}} + \left(\frac{a_M}{a_S}(1-\mu_M)\sin\theta_M(\bar{\tau})\right)\hat{\bar{Y}}. \tag{5.10c}$$

First, points crossing the Poincaré section of $\Gamma_{\bar{X}=1-\mu_S}$ in the patched three-body approximation are recorded. Then, those points are propagated forward and backward by using Eqns. (5.9) in order to construct the four-body trajectories. The resulting four-body trajectories are filtered such that the perigee radius would be equal to LEO altitudes. In Fig. 5.9, perigee versus perilune plot is drawn for these filtered trajectories. Each point in the plot corresponds to a particular trajectory in BRFBP. The resulting four-body trajectories are given in Fig. 5.10.

Since the patched three-body trajectories deviate in BRFBP, the number of solutions dramatically decreases compared to Fig. 5.6. In this study, it is aimed to construct LEO to Low Lunar Orbit (LLO) low-energy transfer. In Fig. 5.9, all the three points have LEO altitudes but the perilune distances are higher than LLO. In order to achieve LLO, targeting algorithm is applied.

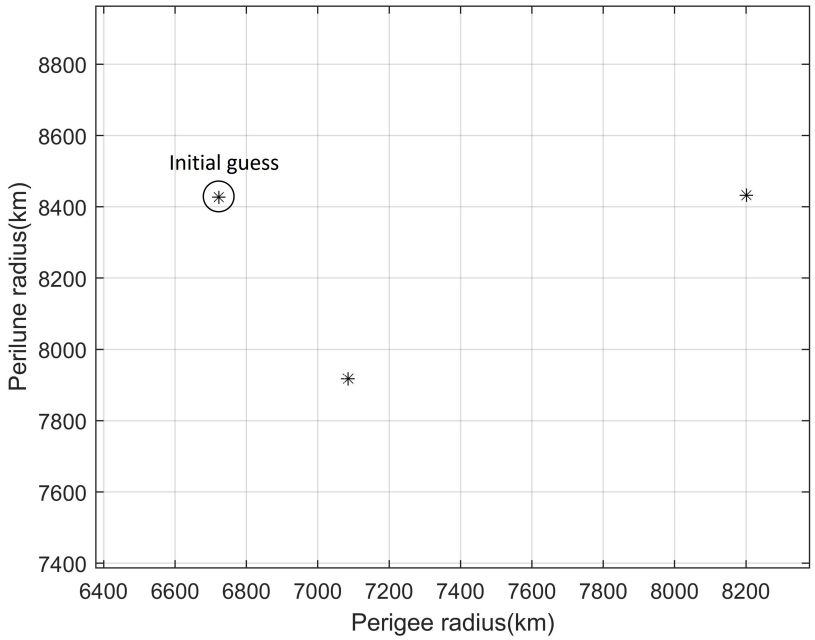

Figure 5.9: The minimum distance to the Earth, perigee, versus the minimum distance to the Moon, perilune, for the filtered trajectories in BRFBP.

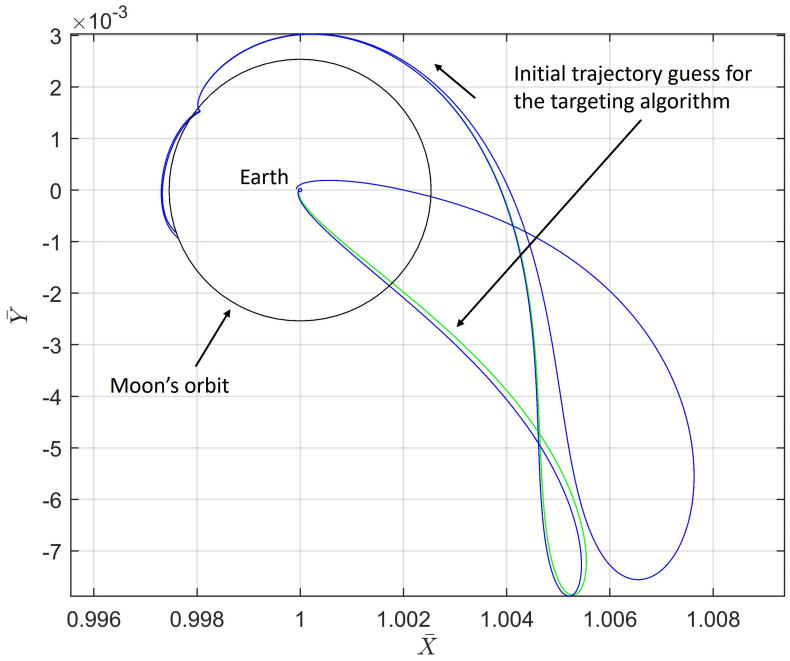

Figure 5.10: Earth to Moon low-energy transfers for the filtered trajectories in BRFBP.

5.1.2.3 Targeting Algorithm

The idea of the targeting algorithm is similar to the differential correction mentioned in Chapter 4. Some design variables are specified, then they are corrected to achieve the desired parameters. In this study, the algorithm described in [50] is implemented, and also used to explain targeting method.

Consider the following nonlinear equation;

$$\vec{f}(\vec{x}) - \vec{y}_d = 0, \tag{5.11}$$

where $\vec{x}$ represents the design variables and $\vec{y}_d$ are the desired parameters. Solution of the Eqn. (5.11) gives the design variables corresponding to the desired parameters. In this sense, targeting algorithm is in fact a root finding problem. So, the roots of Eqn. (5.11) can be found by using numerical root finding methods like Newton-Raphson.

For the multi-variable problems, the Newton-Raphson method is given as;

$$\vec{x}_{k+1} = \vec{x}_k - {J_n}^{-1} \left(\vec{f}(\vec{x}_k) - \vec{y}_d \right), \tag{5.12}$$

where J is the Jacobian matrix. When generating the periodic orbits with differential correction, elements of the Jacobian can be given with the analytical expressions. But generally, it may not be possible to calculate the partial derivatives in the Jacobian analytically. So, elements of the Jacobian is calculated by using the following numerical differentiation;

$$J_i = \frac{1}{\delta x_i} \left(\vec{f}(\vec{x} + \vec{\delta x}_i) - \vec{f}(\vec{x}) \right). \tag{5.13}$$

Targeting algorithm starts with an initial guess and improves it in an iterative manner to achieve the desired parameters.

In this study, initial guess is taken from the pathed three-body approximation. To be more specific, targeting algorithm starts with the initial condition on the Poincaré surface of $\Gamma_{\bar{X}=1-\mu_S}$. The reason for this choice is that the perigee and perilune altitudes can be targeted starting from that initial condition. In the algorithm, components of the velocity vector at a fixed position are the design variables, and they are changed to achieve the desired parameters. For the departure trajectory from Earth, perigee altitude of 400 km, for the arrival trajectory to the Moon, perilune altitude of 100 km,

are targeted. So, there are two different initial conditions that are used to generate Earth and Moon legs of the transfer. The initial condition;

$$\vec{x}_p^E = \left(\bar{X}_p, \bar{Y}_p, \dot{\bar{X}}_p^E, \dot{\bar{Y}}_p^E\right), \tag{5.14}$$

is propagated backward to obtain departure trajectory, and the initial condition;

$$\vec{x}_p^M = \left(\bar{X}_p, \bar{Y}_p, \dot{\bar{X}}_p^M, \dot{\bar{Y}}_p^M\right), \tag{5.15}$$

is propagated forward to obtain the arrival trajectory. Propagation is performed by using the equations of motion of BRFBP. Note that the both initial conditions have the same position, that is sometimes called as patch point, but different velocity. Therefore a velocity change or in other words a maneuver is required at the patch point. The low-energy transfer trajectory resulted from the targeting algorithm and also the ballistic capture part at the Moon are given in Fig. 5.11 and Fig. 5.12.

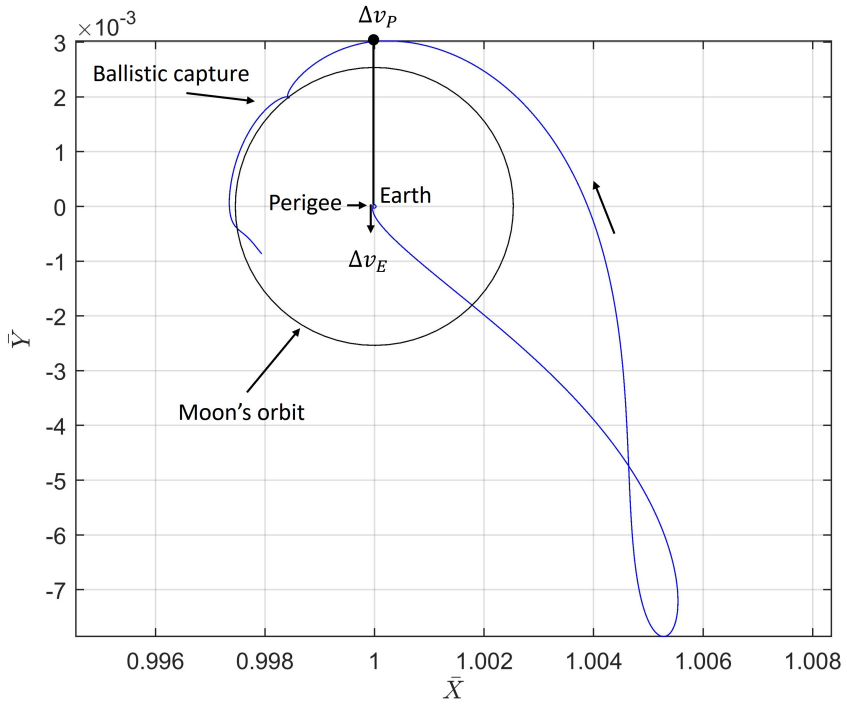

Figure 5.11: LEO to LLO low-energy transfer in BRFBP.

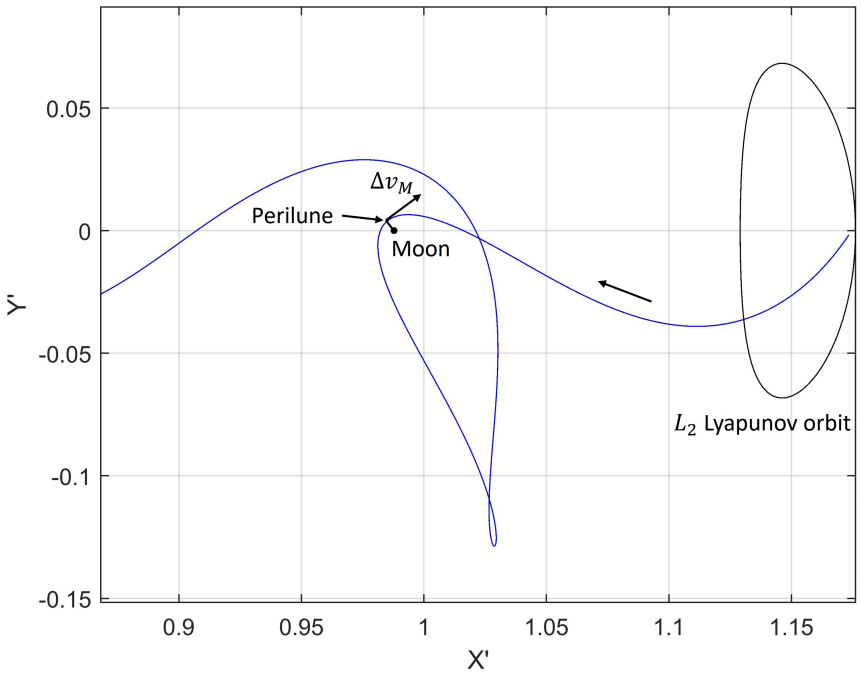

Figure 5.12: Ballistic capture at the Moon in BRFBP.

Initially, spacecraft is placed at a 400 km altitude circular LEO by a launcher. Then, the Earth escape maneuver, Δv_E, is applied for the injection to the low-energy transfer. After about 85 days from escape maneuver, spacecraft reaches the patch point where it applies a maneuver, Δv_P, to target 100 km perilune altitude. It takes about 3 days from patch point to perilune. Finally, the capture maneuver, Δv_M, is applied at perilune in retrograde fashion to acquire 100 km circular LLO. If the capture maneuver is not applied somehow, spacecraft still has one revolution around the Moon so the capture is ballistic. In fact, this is one of the advantages of low-energy transfer against the Hohmann transfer. The other advantage is to have a lower amount of capture maneuver which will be adressed in the maneuver table. All the maneuvers are calculated in the inertial frame, so the relevant rotating frame to inertial frame transformations are considered in the calculation. The resulting maneuver magnitudes and its comparison with Hohmann transfer are given in Tab. 5.1.

Magnitude of the Earth escape maneuver is similar in both methods. But the capture maneuver is about 200 m/s smaller for the low-energy transfer, and it is another

advantage of this method. In overall, low-energy transfer requires 117 m/s less Δv compared to Hohmann transfer, but the transfer duration is about 3 months. Therefore, low-energy transfer is suitable for the unmanned lunar missions.

Table 5.1: Comparison with Hohmann and Low-energy transfers

Transfer method	Δv_E (km/s)	Δv_P (km/s)	Δv_M (km/s)	Δv_T (km/s)	Duration (days)
Hohmann [45]	3.141	-	0.838	3.979	5
Low-energy	3.148	0.075	0.639	3.862	88

In fact, it is possible to reduce Δv further in low-energy transfer. Because the solution coming from the targeting algorithm may not be the optimum one. It just gives a solution satisfying the desired conditions. So, one may look [51] for the optimization of low-energy transfers.

5.2 Search for Planet 9 with Sub-Relativistic Spacecrafts

A possibility of a planet in the outer solar system, commonly known as Planet 9, is proposed to explain unexpected clustering of the Kuiper Belt Objects [52],[53]. Telescope searches are still ongoing, although a detection has not yet been achieved [54]. Since the telescope searches have been inconclusive so far, it is also proposed that this object might be a primordial black hole [55]. To detect Planet 9, alternative ways have been suggested such as sending a cluster of small sub-relativistic spacecrafts and measuring the deflection of their trajectories due to gravity of Planet 9 [56], aiming to measure the Hawking radiation spreading from the primordial black hole with a sub-relativistic spacecraft although it is mentioned that capturing the weak signal would be challenging [57]. In addition, the Zwicky Transient Facility public archive shows no candidate [58]. More recently, a candidate location of Planet 9 is proposed in [59] by tracing the trajectory of an interstellar meteoroid backwards and looking its coincidence with the maximum probability region of Planet 9.

In this thesis, we focus on the method based on measuring the deflection due to gravity of Planet 9 in the trajectory of a spacecraft attaining sub-relativistic speed with

use of advanced technologies like solar sail [60] or laser propulsion [61]. In [56], the deflection is studied in terms of time delay in the signal sending from the spacecraft to Earth with sufficiently accurate timekeeping requirement. To avoid this requirement, measurement of the transverse displacement is proposed by using Very Long Baseline Interferometry (VLBI) [62]. In addition, effects of the drag and electromagnetic forces exerted by the interstellar medium on spacecraft's trajectory is also discussed in [63], including parameter space of the spacecraft to distinguish gravity of Planet 9 from other perturbations.

Firstly, the Planet 9 and spacecraft two-body problem is investigated with the perturbative approach used in [56] for the current orbital parameters of Planet 9, and the analytical expression of transverse displacement given in [62] is derived. Secondly, the effect of Sun is examined in the context of Sun-Planet 9-spacecraft CRTBP under some assumptions. Then, the two-body and three-body results are compared to assess effect of Sun. Lastly, the perturbations due to drag and magnetic forces are analyzed to discuss that whether the gravity of Planet 9 can be distinguishable from those perturbations.

5.2.1 Planet 9 and Spacecraft Two-Body Problem

First, the deflection in the trajectory of a sub-relativistic spacecraft is investigated in the context of Planet 9 and spacecraft two-body problem with the perturbative approach used in [56]. To understand how strong the gravitational effect of Planet 9 is on the spacecraft, kinetic energy per unit mass, $v^2/2$, and gravitational potential energy of Planet 9, $-\mu_{P9}/\rho$, are compared in the vicinity of Planet 9.

The current estimates on the mass and orbit of Planet 9 given in [64] suggest that the gravitational parameter is $\mu_{P9} \approx 6.2\mu_E$ where $\mu_E = 398600$ km^3/s^2 and semi-major axis is $a_{P9} \approx 380$ AU. Then, the smallest impact parameter for the half sky search with 1000 spacecrafts is calculated $\rho \approx 30$ AU as given in [56]. Let the sub-relativistic speed of the spacecrafts to be $v = 0.001c$ where $c = 2.99792458 \times 10^5$ km/s is the speed of light. This sub-relativistic speed is chosen to make the mission duration reasonable. If the relevant parameters are put into the equations of kinetic and potential energies, one obtain that kinetic energy is eight order larger than the

gravitational energy. So, the gravity of Planet 9 can be considered as a perturbative effect on a straight line trajectory. The reference frame and configuration of the two-body problem are given in Fig. 5.13. The black straight line is the unperturbed trajectory in the absence of Planet 9, and blue trajectory is the perturbed one. Finally, ρ is the minimum distance to the Planet 9 along the unperturbed trajectory.

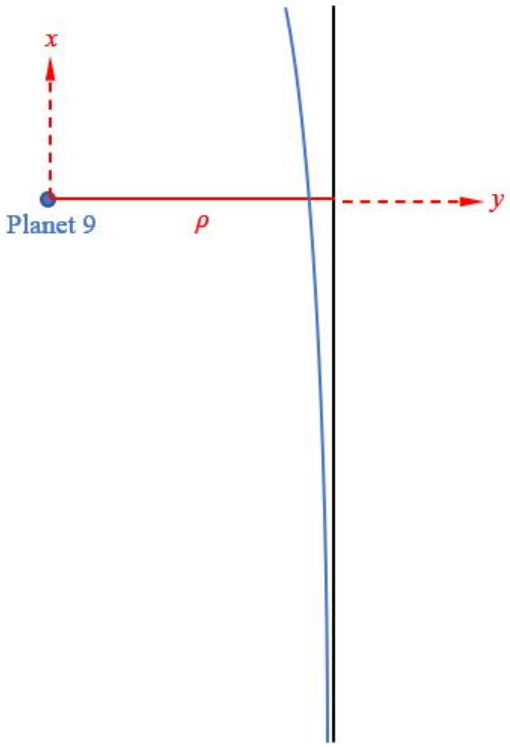

Figure 5.13: Configuration of the Planet 9 and spacecraft two-body problem.

The position vector of the spacecraft in the vicinity of Planet 9 would take the form;

$$\vec{r}(t) = v_0 t\hat{i} + \rho\hat{j} + \vec{r}_1(t), \tag{5.16}$$

where $\vec{r}_1(t) = x_1\hat{i} + y_1\hat{j}$ is the deviation from the straight line trajectory. For the unperturbed trajectory, position at $t = 0$ corresponds to the minimum distance between Planet 9 and spacecraft. Then, the velocity and acceleration vectors become;

$$\dot{\vec{r}}(t) = (v_0 + \dot{x}_1)\,\hat{i} + \dot{y}_1\hat{j}, \tag{5.17a}$$

$$\ddot{\vec{r}}(t) = \ddot{x}_1\hat{i} + \ddot{y}_1\hat{j}. \tag{5.17b}$$

The relative position vector of the spacecraft with respect to Planet 9 satisfies;

$$\ddot{\vec{r}} = -\frac{\mu_{P9}}{r^3}\vec{r}, \tag{5.18}$$

where $r = [(v_0 t + x_1)^2 + (\rho + y_1)^2]^{1/2}$. Then, the components of the equations of motion are;

$$\ddot{x}_1 = -\frac{\mu_{P9}}{\left(v_0^2 t^2 + 2v_0 t x_1 + x_1^2 + \rho^2 + 2\rho y_1 + y_1^2\right)^{3/2}} \left(v_0 t + x_1\right), \tag{5.19a}$$

$$\ddot{y}_1 = -\frac{\mu_{P9}}{\left(v_0^2 t^2 + 2v_0 t x_1 + x_1^2 + \rho^2 + 2\rho y_1 + y_1^2\right)^{3/2}} \left(\rho + y_1\right). \tag{5.19b}$$

Since Planet 9 has a perturbative effect, the deviations would be small so that;

$$\frac{x_1}{v_0 t} \ll 1, \quad \frac{y_1}{\rho} \ll 1. \tag{5.20}$$

Then, the equations of motion take the following form;

$$\ddot{x}_1 = -\frac{\mu_{P9}}{\left(v_0^2 t^2 + \rho^2\right)^{3/2}} v_0 t, \tag{5.21a}$$

$$\ddot{y}_1 = -\frac{\mu_{P9}}{\left(v_0^2 t^2 + \rho^2\right)^{3/2}} \rho. \tag{5.21b}$$

From the integration, perturbative velocities can be found as;

$$\dot{x}_1 = \frac{\mu_{P9}}{v_0 \sqrt{v_0^2 t^2 + \rho^2}} + c_x, \tag{5.22a}$$

$$\dot{y}_1 = -\frac{\mu_{P9}}{\rho \sqrt{v_0^2 t^2 + \rho^2}} t + c_y, \tag{5.22b}$$

where c_x and c_y are the integration constants to be found from the boundary conditions. At $t \to -\infty$, there should not be any gravitational effect of Planet 9 on the spacecraft, so the velocity should be;

$$\lim_{t \to -\infty} \dot{\vec{r}}(t) = v_0 \hat{i}. \tag{5.23}$$

Thus, the proper boundary condition would be;

$$\lim_{t \to -\infty} \dot{\vec{r}}_1(t) = 0. \tag{5.24}$$

After applying the boundary conditions, final form of the perturbative velocity vector, $\dot{\vec{r}}_1$, becomes;

$$\dot{x}_1 = \frac{\mu_{P9}}{v_0 \sqrt{v_0^2 t^2 + \rho^2}}, \tag{5.25a}$$

$$\dot{y}_1 = -\frac{\mu_{P9}}{\rho \sqrt{v_0^2 t^2 + \rho^2}} t - \frac{\mu_{P9}}{\rho v_0}. \tag{5.25b}$$

Finally, the magnitude of the transverse velocity change can be found as;

$$\Delta v_y = \left| \lim_{t\to\infty} \dot{y}_1 - \lim_{t\to-\infty} \dot{y}_1 \right| = \left| \lim_{t\to\infty} \dot{y}_1 \right| = \frac{2\mu_{P9}}{\rho v_0}. \tag{5.26}$$

In thesis, we focus on the measurement of transverse displacement instead of time delay in the signal to relax accurate timekeeping requirement. So, the maximum angular displacement is given as [62];

$$\alpha = \frac{\Delta v_y}{v_x^{(0)}}. \tag{5.27}$$

By putting Eqn. (5.26) into the Eqn. (5.27), one can obtain the following;

$$\alpha = \frac{2\mu_{P9}}{\rho v_0^2} \approx 1 \times 10^{-8} \text{ radians}. \tag{5.28}$$

In [62], it is mentioned that the angular displacement can be measured precisely with use of VLBI. But it has a detection threshold of order 10^{-9} radians for high frequency sources. The Eqn. (5.28) is already above the threshold. To further improve the detectability, impact parameter may be decreased or spacecraft may be slowed down.

5.2.2 Sun-Planet 9-Spacecraft Three-Body Problem

In this section, the angular displacement is studied in the context Sun-Planet 9-spacecraft three-body problem to understand whether the three-body context provides new prospects for the detection. To have an idea on the effect of Sun, the ratio of gravitational acceleration due to Planet 9 and Sun are calculated by taking the gravitational parameter of Sun as $\mu_S = 132712 \times 10^6$ km^3/s^2;

$$\left(\frac{\mu_S}{a_{P9}^2}\right) / \left(\frac{\mu_{P9}}{\rho^2}\right) \approx 335, \tag{5.29}$$

which motives to consider the effect of Sun. The tidal acceleration due to Sun and Planet 9 on the spacecraft have the ratio;

$$\left(\frac{\mu_S}{a_{P9}^3}\right) / \left(\frac{\mu_{P9}}{\rho^3}\right) \approx 26. \tag{5.30}$$

So, the tidal force of the Sun is still larger than the Planet 9.

Motion of the spacecraft in the presence of the Sun and the Planet 9 is investigated by considering the CRTBP as the underlying dynamical model. In using the CRTBP, following assumptions are used;

- Sun and Planet 9 are moving in a circular orbit around their barycenter. In fact, the orbit of Planet 9 is estimated as elliptic ($e \approx 0.2 - 0.5$) [53], but it is considered that the simple circular model may still provide insight about the effect of Sun.

- The orbit of Planet 9 is estimated as moderately inclined ($i \approx 15^\circ - 25^\circ$) [53]. Although, it is assumed that Sun, Planet 9 and spacecraft are moving in the same plane to reduce dimension of the problem.

- Mass of the spacecraft is negligible such that it does not effect the motion of Sun and Planet 9.

The equations of motion of CRTBP are solved with numerical integration for the particular initial conditions. In the numerical integration, MATLAB built-in ode45 solver is used with absolute and relative tolerances of 10^{-13}. It is important to note that the transverse displacement should be calculated relative to the inertial frame, although the motion is obtained in the rotating frame of CRTBP. Therefore, the frame transformations are necessary between rotating and inertial frames. About the integration duration, it is assumed that the measurements start when the spacecraft reaches sub-relativistic speed and continue until $t \approx 2(a_{P9} - \bar{x}_0)/v_0$ is achieved. So, symmetric time interval is considered to calculate the transverse displacement.

In order to decide the proper initial conditions, escape trajectories from the solar system are examined. In [65] and [66], interstellar mission trajectories with the use of solar sails are studied. Due to the reduction of solar flux and so its propulsive effect, it is considered in [66] to separate solar sail at approximately 5 AU. Example of an interstellar escape trajectory with solar sail is given Fig. 5.14. In this analysis, it is assumed that spacecraft reaches the sub-relativistic speed at the solar sail separation distance, so the initial position for the numerical integration is chosen by considering this assumption. The two possible initial configurations are considered which are given in Fig. 5.15 and Fig. 5.16.

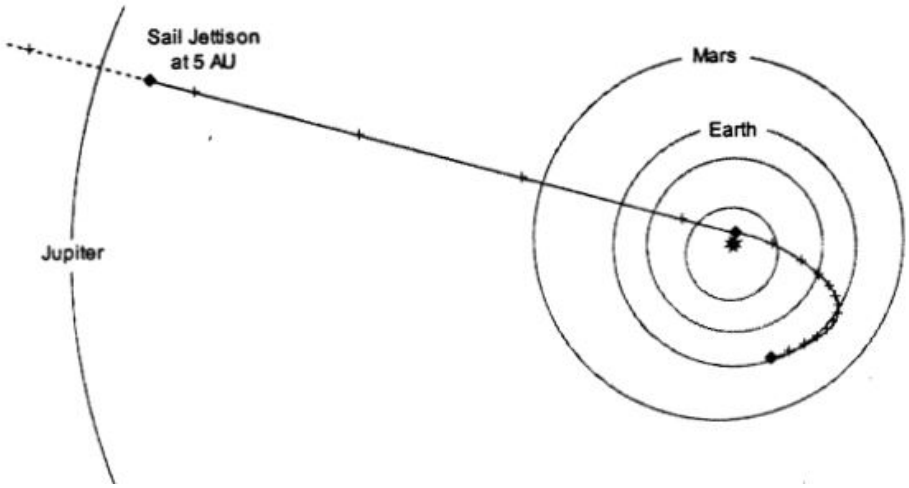

Figure 5.14: Example of an interstellar escape trajectory with solar sail aiming to reach 1000 AU in 20 years [66].

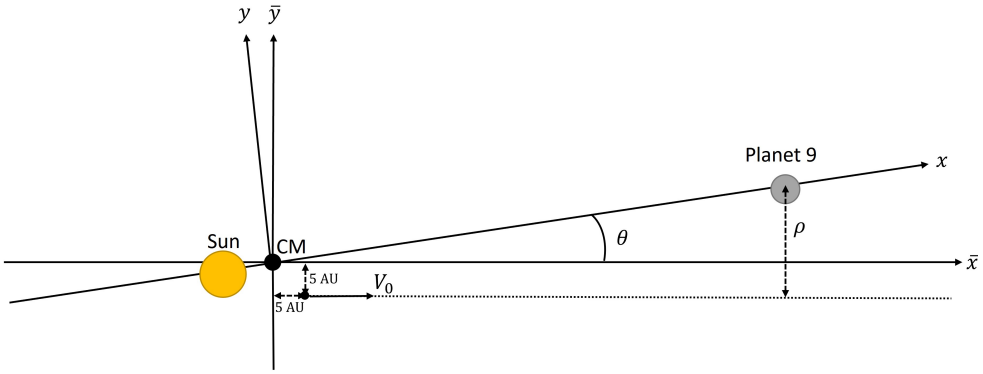

Figure 5.15: First initial configuration (case A).

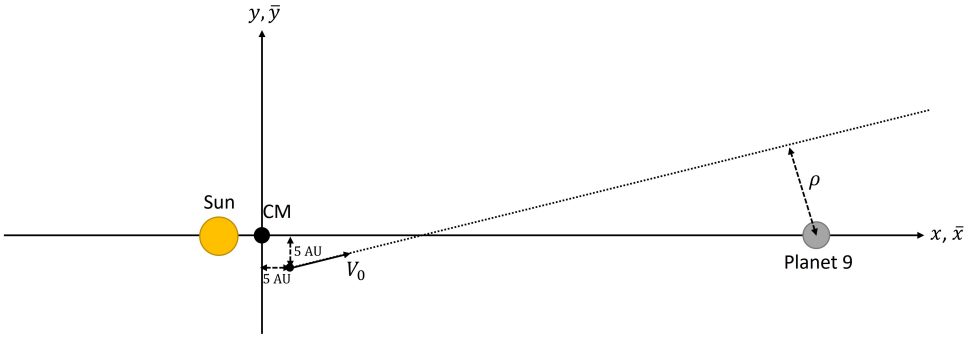

Figure 5.16: Second initial configuration (case B).

In the presence of the Sun, unperturbed or nominal trajectory of the spacecraft is defined as the trajectory obtained from the Sun-spacecraft two-body problem. Then, the perturbation due to Planet 9 is calculated as the difference between Sun-Planet 9-spacecraft three-body trajectory and Sun-spacecraft two-body trajectory. The results of the both initial configurations are obtained for different velocities and impact parameters in Fig. 5.17 and Fig. 5.18.

The two-body results correspond to the perturbation of Planet 9 on a straight line trajectory and they are obtained from the Eqn. 5.28. The three-body results correspond to the perturbation of Planet 9 on a trajectory that is defined by Sun and spacecraft two-body problem. The two-body and three-body results are compared to assess whether considering the Sun yields significant effect on the detection of Planet 9. Besides, different velocities and impact parameters are also considered since the angular displacement depends on those parameters. Velocities are decreased until 0.0004c because further reduction results in a longer mission duration.

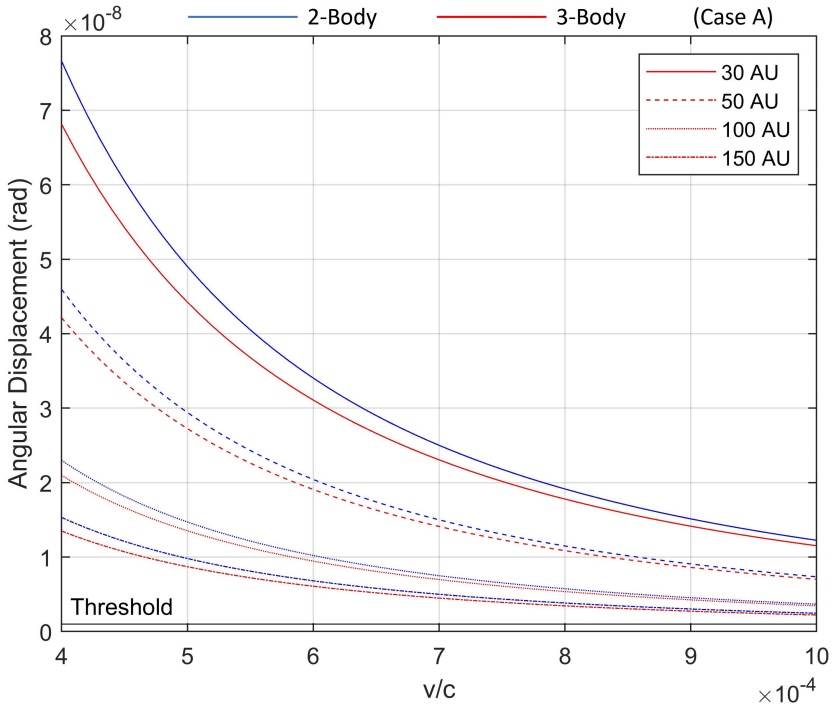

Figure 5.17: Angular displacement of two-body and three-body trajectories for the Case A.

In Fig. 5.17, results for the initial configuration of case A are given. The angular displacement due to Planet 9 is larger in the two-body context for all the impact parameters and velocities. In CRTBP, Planet 9 and Sun are moving in circular orbits unlike the two-body setting which considers the Planet 9 as stationary. Due to the movement of Planet 9, the distance between Planet 9 and spacecraft is larger at the flyby for the three-body trajectory. So, less angular displacement is obtained. As the velocity decreases, kinetic energy becomes comparible with the potential energy due to Sun and Planet 9. Therefore, their effects get visible and larger displacement occurs. As the impact parameter increases, spacecraft flybys with Planet 9 in a larger distance. So, its gravitational effect decreases and less displacement occurs. Lastly, all the angular displacements are above the detection threshold.

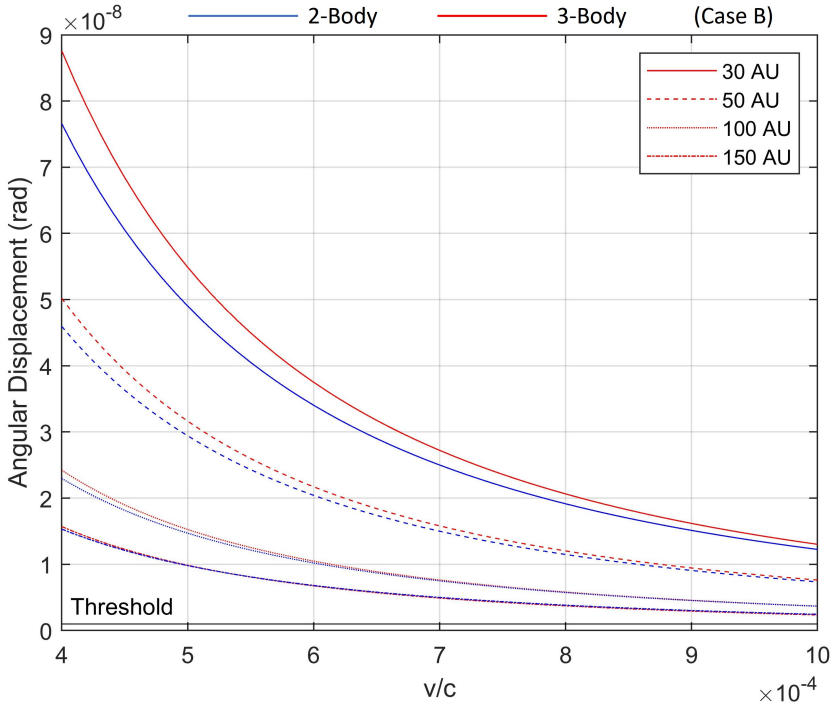

Figure 5.18: Angular displacement of two-body and three-body trajectories for the Case B.

In Fig. 5.18, results for the initial configuration of case B are given. Unlike the case A, angular displacement due to Planet 9 is larger in the three-body context for all the impact parameters and velocities. Due to the movement of Planet 9 in the CRTBP, the distance between Planet 9 and spacecraft is smaller at the flyby. So,

the angular displacement due to Planet 9 is larger. The behaviour for the different impact parameters and velocities are similar with case A. Here again, all the angular displacements are above the detection threshold.

Besides the perturbation due Planet 9, spacecraft is in the effect of non-gravitational perturbations like drag and magnetic forces. Therefore, it necessary to investigate whether the perturbation due to Planet 9 can be distinguishable from the other perturbations. In fact, this is investigated in [63] without considering the Sun and the directions of perturbations. In this thesis, comparison of perturbations is performed with considering the directions as well in the presence of Sun by solving the equations of motion numerically. Since the angular displacement due to Planet 9 is larger for the three-body trajectory in case B, rest of the analysis is performed considering the Case B.

5.2.3 Drag Force on the Spacecraft Trajectory

Due to the interstellar gas particles and dust, spacecraft is in the effect of drag force that is given by [63];

$$F_{drag} = 1.4 n_H m_H v^2 A_{sp}, \tag{5.31}$$

where n_H is the proton number density and taken as $n_H = 1$ cm^{-3} which is a standard parameter for the interstellar medium [63], m_H is the proton mass, v is the sub-relativistic speed and A_{sp} is the drag area. The direction is taken as the opposite velocity direction.

The perturbative effect of drag force is investigated as the difference between Sun-Drag-spacecraft trajectory and Sun-spacecraft two-body trajectory. It is assumed that drag force effects the spacecraft when it reaches sub-relativistic speeds to the end of the analysis. In calculating the drag force, parameters are taken with the same as in [63] for the comparison. Those are $A_{sp} = 0.5$ cm^2 and $M_{sp} = 1$ gram. The resulting angular displacement versus velocity plot is given in Fig. 5.19.

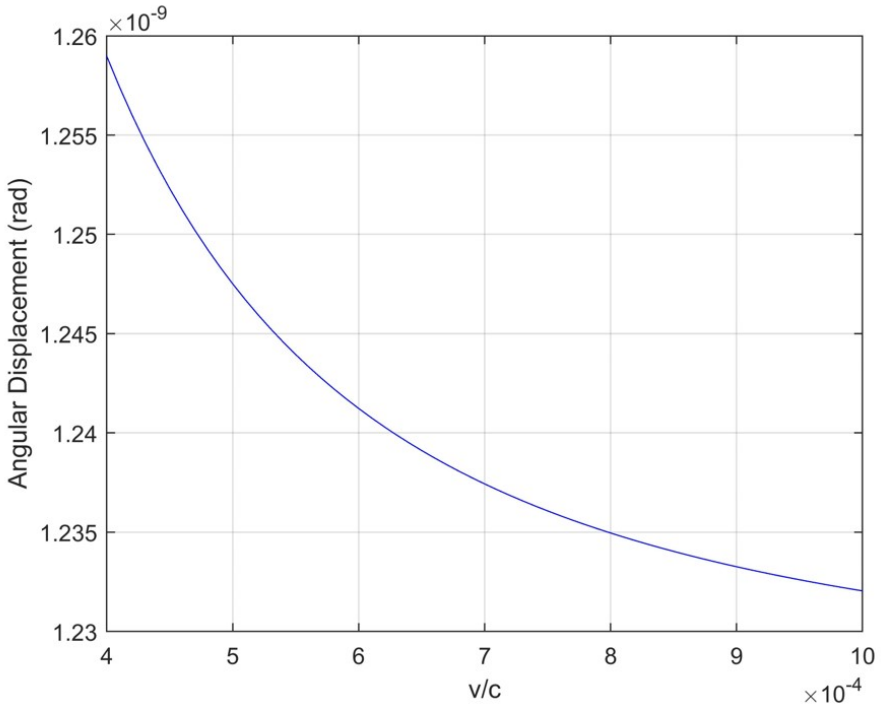

Figure 5.19: Angular displacement due to drag force.

The drag force slows down the spacecraft, so it travels less transverse distance compared to Sun-spacecraft trajectory. As the velocity increases, it is expected to have increasing trend in the displacement due to larger drag force but just the opposite happens in Fig. 5.19. The reason is that spacecraft travels same distance for all velocities, in other words traveled distance is constant. This is due to assumptions of the problem. So, the spacecraft with high velocity travels the same distance in smaller amount of time which is resulted with shorter interaction time with drag force. Although, the spacecraft with low velocity is in the effect of drag force in a longer time interval, so drag causes more angular displacement for the low velocities.

The more promising result about Fig. 5.19 is that the angular displacement due to drag force is about one order smaller than the Planet 9. In fact, the displacement due to drag force is in the limit of detection threshold and it may not be even detectable. So, it is found that gravity of Planet 9 can be distinguishable from the drag force for the parameters used in the analysis.

5.2.4 Magnetic Force on the Spacecraft Trajectory

During the cruise, spacecraft gets charged due to collisions of interstellar particles and also due to photoelectric effects from solar and interstellar photons [63]. Then, the interstellar magnetic field exerts magnetic force to the charged spacecraft which curves the trajectory. The magnetic force due to interstellar medium is given as [63];

$$F_{mag} = eZ_{sp}vB_{\perp}/c, \tag{5.32}$$

in Gaussian units. Here, e is the elementary charge, v is the sub-relativistic speed, $B_{\perp}$ is the magnetic field component perpendicular to the motion, c is the speed of light and Z_{sp} is the maximum charge of the spacecraft that is given as [63];

$$Z_{sp} = m_e v^2 \left(M_{sp}/\rho\right)^{1/3} / e^2, \tag{5.33}$$

where m_e is the electron mass, M_{sp} is the spacecraft mass and ρ is the density of spacecraft. One can look at [67] for detailed discussion about the calculation of Z_{sp}.

In calculating the magnetic force, parameters are taken with the same as in [63] for the comparison. Those are $M_{sp} = 1$ gram, $\rho = 3$ gram cm^{-3} and $B_{\perp}$ $5\mu G$. It is important to note that direction of the magnetic field is unknown. Therefore, direction is taken such that the maximum displacement occurs to consider the worst case in terms of distinguishability. Then, the perturbative effect of magnetic force is investigated as the difference between Sun-Magnetic Force-spacecraft trajectory and Sun-spacecraft two-body trajectory. The resulting angular displacement versus velocity plot is given Fig. 5.20.

As the velocity increases, magnetic force also increases and curves the trajectory. Therefore, larger angular displacement is obtained for the high velocities. There is cubic dependence on velocity for the magnetic force, and this makes the effect of velocity more dominant compared to drag force. But the resulting angular displacement is below the detection threshold and the effect of magnetic force is not even detectable. So, it is found that gravity of Planet 9 can be distinguishable from the magnetic force for the parameters used in the analysis.

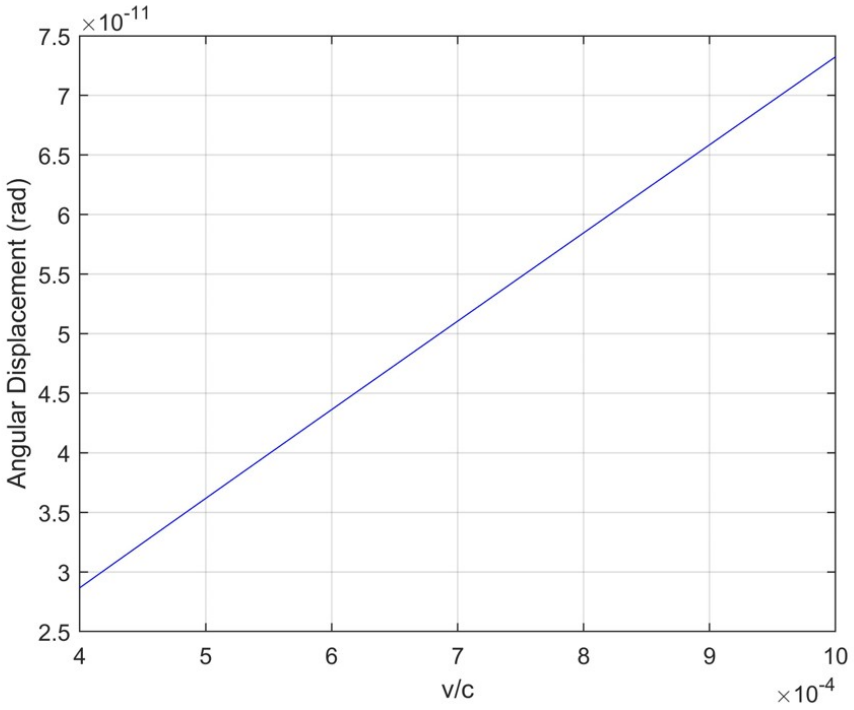

Figure 5.20: Angular displacement due to magnetic force.

CHAPTER 6

CONCLUSIONS

In this thesis, orbit structures in the planar CRTBP are investigated and its two applications are demonstrated. First, the local orbit structures such as transit, non-transit and periodic orbits around the equilibrium points are obtained by linearizing the equations of motion. Then, the periodic orbits around collinear equilibrium points, so called Lyapunov orbits, are investigated in detail. In this regard, initial condition of the Lyapunov orbit coming from the linear approximation is improved by utilizing differential correction and the family of Lyapunov orbits is generated with continuation method. Then, the stability of Lyapunov orbits are analyzed with the use of the Poincaré map. From this stability analysis, stable and unstable invariant manifolds are obtained and they are used to construct global orbit structures, namely homoclinic orbit which connects a Lyapunov orbit with itself and heteroclinic orbit which connects different Lyapunov orbits. To have an idea on the chaotic nature in CRTBP, sensitive dependence to the initial conditions of a Lyapunov orbit is also investigated with use of Lyapunov exponent.

Lastly, the two applications of CRTBP are demonstrated. First, Earth to Moon low-energy spacecraft trajectories are calculated by utilizing patched three-body approximation of Sun-Earth-spacecraft and Earth-Moon-spacecraft CRTBPs. The resulting trajectory constitutes less risk and requires less fuel compared to traditional Hohmann transfer. Second, search for Planet 9 with sub-relativistic spacecrafts is performed by considering CRTBP of Sun-Planet 9-spacecraft. To investigate the effect of Sun in the detection of Planet 9, three-body trajectory and Planet 9-spacecraft two-body trajectory are compared. In the numerical analysis, two possible initial conditions are used with different impact parameters and spacecraft velocities. One of the configuration

yields larger and the other one yields smaller angular displacement compared to two-body problem. It is found that the effect of Sun is not directly seen in the detection but the presence of Sun causes the motion of Planet 9 and this yields larger or smaller angular displacements depending on the initial condition. In presence of Sun, it is also looked for whether the perturbation due to gravity of Planet 9 can be distinguishable from the other non-gravitational perturbations such as drag and magnetic forces. The analysis is performed with numerical integration by considering those perturbations in the equations of motion. It is found that the angular displacements due to drag and magnetic forces are below the detection threshold and they are not even detectable for the parameters used in the analysis. As a future work, the orbits of Trans-Neptunian Objects (TNOs) can be investigated in the context of Sun-Planet 9-TNO Elliptic Restricted Three-Body Problem (ERTBP). If the observed orbits of TNOs fit to the orbit structures in ERTBP, like how the orbits of Trojan asteroids in our solar system are better understood with CRTBP, then this may be a strong evidence for the existence of Planet 9.

REFERENCES

[1] Z. E. Musielak and B. Quarles, "The three-body problem," *Reports on Progress in Physics*, vol. 77, no. 6, 2014.

[2] D. Brewster, *Memoirs of the Life, Writings, and Discoveries of Sir Isaac Newton*, 1th ed., Cambridge University Press, 1855.

[3] L. Euler, "De moto rectilineo trium corporum se mutuo attrahentium," *Novi Comm. Acad. Sci. Imp. Petrop.*, vol. 11, pp. 144-151, 1767.

[4] J. L. Lagrange, "Essai sur le probléme des trois corps," *Euvres*, vol. 6, pp. 229-331, 1772.

[5] C. E. Delaunay, "Théorie du mouvement de la lune II," *Mémoire de l'Academie des Sciences*, vol. 29, pp. 1-931, 1867.

[6] A. Lindstedt, "Sur la détermination des distances mutuelles dans le probléme des trois corps," *Annales de l'École Normale (3)*, vol. 1, pp. 85-102, 1884.

[7] H. Gyldén, "Nouvelles recherches sur les séries employées dans les théories des planétes," *Acta*, vol. 17, pp. 1-168, 1893.

[8] K. F. Sundman, "Mémoiresur le probléme des trois corps," *Acta*, vol. 36, pp. 105-179, 1912.

[9] H. Poincaré, *New Methods of Celestial Mechanics*, 1th ed., American Institute of Physics, 1992.

[10] J. Barrow-Green, *Poincaré and the Three Body Problem*, 1th ed., American Mathematical Society, 1996.

[11] A. N. Kolmogorov, "On conservation of conditionally periodic motions under small perturbations of the hamiltonian," *Dokl. Acad. Nauk SSR*, vol. 98, pp. 527-530, 1954.

[12] J. Moser, “On invariant curves of area-preserving mappings of an annulus,” *Nachricht von der Akademie der Wissenschaften, Gottingen II, Math. Phys.*, vol. K1, pp. 1-20, 1962.

[13] V. I. Arnold, “Proof of a theorem of A. N. Kolmogorov on the invariance of quasi-periodic motions under small perturbations of the hamiltonian,” *Russian Mathematical Surveys*, vol. 18, pp. 9-36, 1963.

[14] M. Hénon, “Families of periodic orbits in the three-body problem,” *Celestial Mechanics*, vol. 10, pp. 375-388, 1974.

[15] V. Szebehely, *Theory of Orbits: The Restricted Problem of Three Bodies*, 1th ed., Academic Press, 1967.

[16] R. Broucke and D. Boggs, “Periodic orbits in the planar general three-body problem,” *Celestial Mechanics*, vol. 11, pp. 13-38, 1975.

[17] J. D. Hadjidemetriou and T. Christides, “Families of periodic orbits in the planar three-body problem,” *Celestial Mechanics*, vol. 12, pp. 175-187, 1975.

[18] C. Moore, “Braids in classical dynamics,” *Phys. Rev. Lett.*, vol. 70, 1993.

[19] A. Chenciner and R. Montgomery, “A remarkable periodic solution of the three-body problem in the case of equal masses,” *Annals of Mathematics*, vol. 152, no. 3, pp. 881-901, 2000.

[20] M. Šuvakov and V. Dmitrašinović, “Three classes of Newtonian three-body planar periodic orbits,” *Phys. Rev. Lett.*, vol. 110, 2013.

[21] X. Li and S. Liao, “More than six hundred new families of Newtonian periodic planar collisionless three-body orbits,” *Science China Physics, Mechanics and Astronomy*, vol. 60, 2017.

[22] X. Li, Y. Jing and S. Liao, “The 1223 new periodic orbits of planar three-body problem with unequal mass and zero angular momentum,” *Publications of the Astronomical Society of Japan*, vol. 70, no. 4, 2018.

[23] X. Li and S. Liao, “Collisionless periodic orbits in the free-fall three-body problem,” *New Astronomy*, vol. 70, pp. 22-26, 2019.

[24] N. C. Stone and N. W. C. Leigh, “A statistical solution to the chaotic, non-hierarchical three-body problem,” *Nature*, vol. 576, pp. 406-410, 2019.

[25] P. G. Breen, C. N. Foley, T. Boekholt and S. P. Zwart, “Newton versus the machine: solving the chaotic three-body problem using deep neural networks,” *Monthly Notices of the Royal Astronomical Society*, vol. 494, no. 2, pp. 2465-2470, 2020.

[26] G. Jacobi, “Sur le mouvement d’un point et sur un cas particulier du probléme des trois corps,” *Comptes Rendus*, vol. 3, pp. 59-61, 1836.

[27] G. W. Hill, “Researches in the Lunar theory,” *American Journal of Mathematics*, vol. 1, pp. 5-26, 1878.

[28] A. M. Lyapunov, *General Problem of the Stability Of Motion*, 1th ed., CRC Press, 1992.

[29] R. W. Farquhar, “The control and use of libration-point satellites,” Ph.D. dissertation, Dept. of Aeronautics and Astronautics, Stanford University, 1968.

[30] R. Zhang, “A review of periodic orbits in the circular restricted three-body problem,” *Journal of Systems Engineering and Electronics*, vol. 33, no. 3, pp. 612-646, 2022.

[31] E. A. Belbruno and J. K. Miller, “Sun-perturbed Earth-to-Moon transfers with ballistic capture,” *Journal of Guidance, Control, and Dynamics*, vol. 16, no. 4, 1993.

[32] W. S. Koon, M. W. Lo, J. E. Marsden and S. D. Ross, “Low energy transfer to the Moon,” *Celestial Mechanics and Dynamical Astronomy*, vol. 81, pp. 63-73, 2001.

[33] W. S. Koon, M. W. Lo, J. E. Marsden and S. D. Ross, *Dynamical Systems, the Three-Body Problem and Space Mission Design*, 2006. Accessed: Jun., 15, 2023. [Online]. Available: http://www.cds.caltech.edu/∼marsden/volume/missiondesign/KoLoMaRo_DMissionBk.pdf

[34] H. D. Curtis, *Orbital Mechanics for Engineering Students*, 4th ed., Butterworth-Heinemann, 2019.

[35] S. C. Chapra and R. P. Canale, *Numerical Methods for Engineers*, 6th ed., McGraw-Hill, 2009.

[36] B. Sicardy, "Stability of the triangular Lagrange points beyond Gascheau's value," *Celestial Mechanics and Dynamical Astronomy*, vol. 107, pp. 145-155, 2010.

[37] J. S. Parker and R. L. Anderson, *Low-energy Lunar trajectory design*, 2013. Accessed: Jun., 15, 2023. [Online]. Available: https://descanso.jpl.nasa.gov/monograph/series12/LunarTraj–Overall.pdf

[38] S. H. Strogatz, *Nonlinear Dynamics and Chaos: With Applications to Physics, Biology, Chemistry, and Engineering*, 2th ed., CRC Press, 2015.

[39] D. J. Dichmann, R. Lebois and J. P. Carrico Jr, "Dynamics of orbits near 3:1 resonance in the Earth-Moon system," *The Journal of the Astronautical Sciences*, vol. 60, pp. 51-86, 2013.

[40] A. H. Nayfeh and B. Balachandran, *Applied Nonlinear Dynamics: Analytical, Computational, and Experimental Methods*, 1th ed., Wiley-VCH, 1995.

[41] J. LLibre, R. Martinez and C. Simo, "Tranversality of the invariant manifolds associated to the Lyapunov family of periodic orbits near L2 in the restricted three-body problem," *Journal of Differential Equations*, vol. 58, no. 1, pp. 104-156, 1985.

[42] D. Guzetti, K. Martin and E. Miskioğlu, "Designing the Moonshot: An Introduction to Gravitational Multi-Body Dynamics," *Auburn Catalog*, Auburn University, 2021.

[43] E. A. Belbruno, "Lunar capture orbits, a method of constructing Earth Moon trajectories and the lunar GAS mission," in *19th AIAA/DGLR/JSASS International Electric Propulsion Conference*, Colorado Springs, 1987.

[44] J. K. Miller and E. A. Belbruno, "Method for the construction of a Lunar transfer trajectory using ballistic capture," in *AAS/AIAA Spaceflight Mechanics Meeting*, Houston, Texas, 1991.

[45] K. Onozaki, H. Yoshimura and S. D. Ross, "Tube dynamics and low energy Earth–Moon transfers in the 4-body system," *Advances in Space Research*, vol. 60, no. 10, pp. 2117-2132, 2017.

[46] K. C. Howell, D. C. Davis and A. F. Haapala, "Application of periapse maps for the design of trajectories near the smaller primary in multi-body regimes," *Mathematical Problems in Engineering*, vol. 2012, 2011.

[47] F. Topputo, M. Vasile and F. Bernelli-Zazzera, "Earth-to-Moon low energy transfers targeting L1 hyperbolic transit orbits," *Annals of the New York Academy of Sciences*, vol. 1065, pp. 55-76, 2005.

[48] D. R. Williams, "Moon Fact Sheet,". https://nssdc.gsfc.nasa.gov/planetary/factsheet/moonfact.html (accessed Jun. 15, 2023).

[49] D. R. Williams, "Earth Fact Sheet,". https://nssdc.gsfc.nasa.gov/planetary/factsheet/earthfact.html (accessed Jun. 15, 2023).

[50] M. M. Berry, "Comparisons between Newton-Raphson and Broyden's methods for trajectory design problems," in *AAS/AIAA Astrodynamics Specialist Conference*, Girdwood, Alaska, 2011.

[51] F. Topputo and E. Belbruno, "Optimization of low-energy transfers," in *Modeling and Optimization in Space Engineering*, 1th ed., Springer, 2012, pp. 389-404.

[52] K. Batygin and M. E. Brown, "Evidence for a distant giant planet in the solar system," *The Astronomical Journal*, vol. 151, no. 2, 2016.

[53] K. Batygin, F. C. Adams, M. E. Brown and J. C. Becker, "The planet nine hypothesis," *Physics Reports*, vol. 805, pp. 1-53, 2019.

[54] S. Naess *et al.*, "The Atacama cosmology telescope: A search for Planet 9," *The Astrophysical Journal*, vol. 923, no. 2, 2021.

[55] J. Scholtz and J. Unwin, "What if Planet 9 is a primordial black hole?," *Phys. Rev. Lett.*, vol. 125, no. 5, 2020.

[56] E. Witten, “Searching for a Black Hole in the Outer Solar System,” https://doi.org/10.48550/arXiv.2004.14192 (accessed Jun. 16, 2023).

[57] A. Arbey and J. Auffinger, “Detecting Planet 9 via Hawking Radiation,” https://doi.org/10.48550/arXiv.2006.02944 (accessed Jun. 16, 2023).

[58] M. E. Brown and K. Batygin, “A search for Planet Nine using the Zwicky transient facility public archive,” *The Astronomical Journal*, vol. 163, no. 2, 2022.

[59] H. S. Navarro, “A candidate location for Planet Nine from an interstellar meteoroid: The messenger hypothesis,” *The Astrophysical Journal*, vol. 945, no. 1, 2023.

[60] M. Macdonald, C. McInnes and G. Hughes, “Technology requirements of exploration beyond Neptune by solar sail propulsion,” *Journal of Spacecraft and Rockets*, vol. 47, no. 3, 2010.

[61] K. L. G. Parkin, “The Breakthrough Starshot system model,” *Acta Astronautica*, vol. 152, pp. 370-384, 2018.

[62] S. Lawrence and Z. Rogoszinski, “The Brute-Force Search for Planet Nine,” https://doi.org/10.48550/arXiv.2004.14980 (accessed Jun. 16, 2023).

[63] T. Hoang and A. Loeb, “Can Planet Nine be detected gravitationally by a subrelativistic spacecraft?,” *The Astrophysical Journal Letters*, vol. 895, no. 2, 2020.

[64] K. Batygin and M. E. Brown, “The orbit of Planet Nine,” *The Astronomical Journal*, vol. 162, no. 5, 2021.

[65] X. Zeng, G. Vulpetti and C. Circi, “Solar sail H-reversal trajectory: A review of its advances and applications,” *Astrodynamics*, vol. 3, no. 1, pp. 1-15, 2019.

[66] C. G. Sauer, “Solar sail trajectories for solar-polar and interstellar probe missions,” in *AAS/AIAA Astrodynamics Specialist Conference*, Girdwood, Alaska, 1999.

[67] T. Hoang and A. Loeb, “Electromagnetic forces on a relativistic spacecraft in the interstellar medium,” *The Astrophysical Journal*, vol.848, no.1, 2017.